The Evolution of Organic Molecules from Star- and Planet-Forming Regions to the Solar System Traced by Isotopic Signatures

A dissertation presented

by

ICHIMURA Ryota

to

The Astronomical Science Program

in partial fulfillment of the requirements

for the degree of

Doctor of Philosophy

in the subject of

Astronomy & Astrophysics

Graduate Institute for Advanced Studies, SOKENDAI

Mitaka

March 2026

Dissertation Advisor: Professor Hideko Nomura ICHIMURA Ryota

The Evolution of Organic Molecules from Star- and Planet-Forming Regions to the Solar System Traced by Isotopic Signatures

Abstract

This thesis presents a theoretical study on the formation and isotopic evolution of complex organic molecules (COMs) in star-forming regions, with particular emphasis on carbon isotope fractionation and isotopomer-specific processes. The work addresses three central questions: (1) How do COMs acquire their isotopic compositions during the early phases of star and disk formation? (2) What are the dominant formation pathways of COMs under interstellar conditions? (3) Can the position of ^{13}C within a molecule be used to constrain its formation pathway?

To answer these questions, I developed and applied a three-phase (gas, grain surface, and ice mantle) gas–grain chemical model that incorporates isotopomer-resolved reaction networks and tracks position-specific ^{12}C/^{13}C ratios. The network includes both thermal and non-thermal chemical processes relevant to COM formation, such as radical–radical reactions on ice surfaces, non-diffusive chemistry, and cosmic-ray-induced radiolysis, enabling the model to follow the chemical and isotopic evolution from prestellar cores to protostellar environments.

Chapter 1 provides the astrophysical and astrochemical background required to understand the context and motivation of this work. It summarizes the current knowledge of star and planet formation, interstellar ice chemistry, and isotopic fractionation processes, establishing the foundation for the modeling efforts in the subsequent chapters.

In Chapter 2, the thesis investigates the evolution of carbon isotope ratios in COMs during the prestellar-to-protostellar transition using a time-dependent three-phase astrochemical model. Particular attention is paid to how different precursor carbon reservoirs (CO, C, or C^+) and isotope exchange processes active in cold cores imprint distinct ^{13}C signatures on COMs. The results demonstrate that molecules formed from CO-derived carbon systematically exhibit mild ^{13}C enrichment, while those originating from C or C^+ reservoirs tend to be ^{13}C-depleted due to isotope exchange chemistry in the gas phase. When only classical warm-up

chemistry is considered, the model tends to overestimate isotope fractionation of COMs observed by molecular lines in protostellar environments. By incorporating recently proposed C-atom reactions on CO- and H_2O ices, the model introduces efficient grain-surface formation channels that partially erase excessive fractionation. This leads to significantly improved agreement with observed $^{12}C/^{13}C$ ratios of selected COMs in the protostellar source, and highlights the importance of cold-grain chemistry in regulating isotopic signatures prior to ice sublimation.

Chapter 3 extends the approach to isotopomer-resolved modeling in order to test whether carbon isotope patterns can be used to distinguish among different COMs formation pathways. Motivated by recent carbon-isotopomer detections of COMs with ALMA and the detection of COMs in interstellar ices with JWST, we construct a new reaction network that tracks the position of ^{13}C within each molecule (e.g., $H^{13}COOCH_3$ versus $HCOO^{13}CH_3$), preserving the position of carbon atoms throughout grain-surface, and ice-mantle chemistry. This framework allows the model to predict isotopomer- and functional-group–specific $^{12}C/^{13}C$ ratios for COMs formed in star-forming cores, taking into account both thermal diffusion–driven radical–radical reactions on warm ice surfaces and non-thermal radiolysis chemistry in the bulk ice. The results show that COMs, particularly those containing methyl groups such as C_2H_5OH, CH_3CHO, and CH_3CN, can exhibit clear isotopomer differences in their $^{12}C/^{13}C$ ratios, reflecting whether they originate from CO-derived versus C/C^+ carbon reservoirs and whether their formation is governed by surface or mantle chemistry under thermal or non-thermal conditions.

In addition, Chapter 3 places these astrochemical results into a broader context by considering their relevance to meteoritic organic matter, with particular emphasis on meteoritic amino acids. By comparing the isotopomer- and position-specific signatures predicted for interstellar COMs with compound- and position-specific isotope measurements of meteoritic organics, the discussion examines whether meteoritic materials may retain interstellar isotopic memory. Emphasis is placed on relative intramolecular isotopic patterns, which are more robust to observational uncertainties, spatial gradients, and parent-body processing than absolute bulk ratios, thereby providing a potential conceptual bridge between interstellar chemistry and Solar System organic matter.

Finally, Chapter 4 summarizes the main findings and outlines future perspectives. The thesis demonstrates that isotopomer-resolved astrochemical modeling provides a physically grounded framework for interpreting molecular isotopic signatures across star- and planet-forming environments, and highlights the importance of non-equilibrium chemistry, time-dependent physical evolution, and material transport. The results point toward tighter integration between

isotopomer chemistry, forthcoming high-sensitivity ALMA and JWST observations, and laboratory constraints, with the ultimate goal of establishing robust isotopic connections from the interstellar medium to Solar System materials.

Contents

Acknowledgments

Your thoughtful dedication goes here.

Chapter 1

Introduction

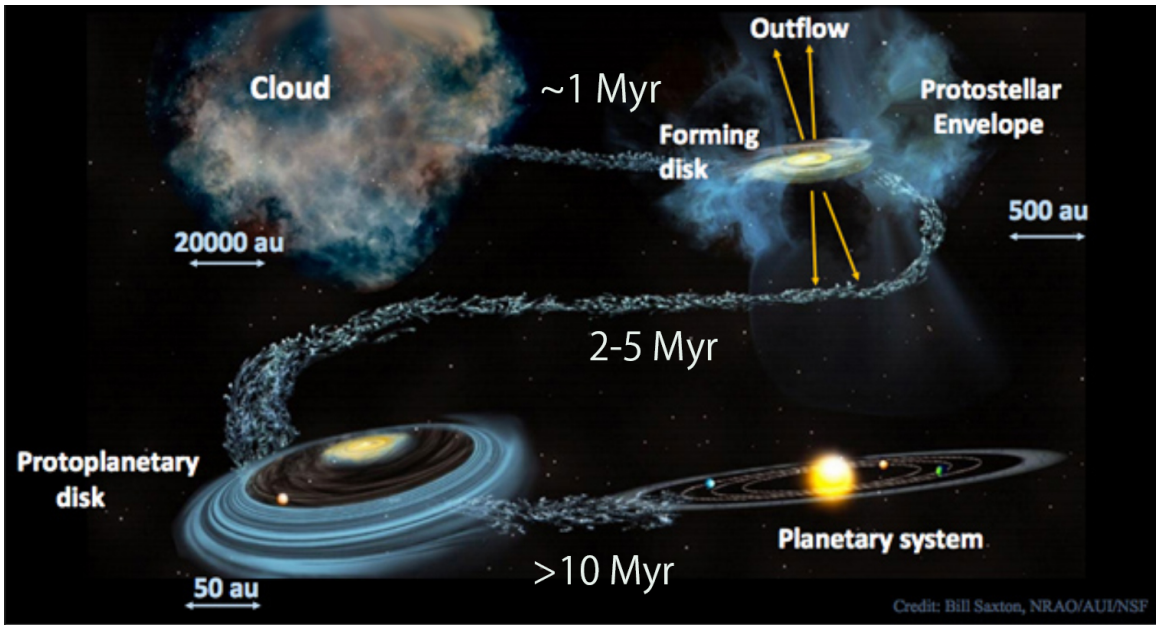

Figure 1.1: Schematic overview of star- and planet-forming environments relevant to this thesis. Dense molecular clouds evolve into prestellar cores, which collapse to form protostars surrounded by protoplanetary disks. Throughout these stages, gas–grain chemistry, ice formation, and isotopic fractionation shape the molecular inventory that is ultimately inherited by comets, asteroids, and planets in young planetary systems, including our own Solar System. In this figure, approximate evolutionary timescales have been added to the original illustration to highlight the temporal context of each stage. Credit: B. Saxton (NRAO/AUI/NSF), modified with added timescale annotations.

Our own Solar System originated within a molecular cloud, an environment

rich in volatile compounds and complex chemistry (Tielens 2013). The molecular inventory inherited by comets, asteroids, and planetary atmospheres bears witness to this interstellar origin, suggesting that the chemical processes active in the star-forming regions laid the groundwork for forming planetary systems, including our own (Caselli & Ceccarelli 2012)(see Figure 1.1).

In the vast expanse of interstellar space, where densities are exceedingly low and temperatures plunge to just a few tens of kelvin, a rich and diverse molecular inventory emerges and evolves. These molecules, formed under non-equilibrium conditions, not only serve as sensitive tracers of their underlying physical environments but also carry chemical memories across truly "astronomical" timescales (Tielens 2021). From the birthplaces of stars within prestellar cores to the chemically active surfaces of protoplanetary disks, molecular species provide a powerful window into the dynamic and thermochemical processes that shape planetary systems.

The study of astrochemistry, probing the formation, destruction, and transport of species in the star-forming regions, is therefore fundamental to understanding not only the origins of chemical complexity in space but also the physical mechanisms underlying star and planet formation (van Dishoeck & Blake 1998). This thesis focuses on the chemical evolution of complex organic molecules and their isotope compositions during the early stages of star and disk formation, with the goal of elucidating the astrochemical processes shaping molecular composition and isotopic structure.

1.1 Universal Nature of Star and Planet Formation

The process of star and planet formation appears to follow a robust physical framework within the Milky Way. Observations of nearby star-forming regions demonstrate that stars form through the gravitational collapse of dense molecular cores, accompanied by the formation of rotationally supported disks, which in turn serve as the birthplaces of planetary systems (McKee & Ostriker 2007). Although local environmental conditions—such as cloud mass, turbulence, and radiation field—introduce diversity in molecular compositions and chemical evolutionary pathways (for example, carbon-chain–rich chemistry in Taurus sources such as TMC-1 (Hirota et al. 2009; Sakai & Yamamoto 2013) and active sulfur-bearing chemistry observed in some Ophiuchus protostars such as Elias 29 (Oya et al.

2019)), infrared and (sub)millimeter observations of nearby star-forming regions nevertheless reveal broadly similar trends in disk formation, dust growth, and the buildup of carbon-bearing complex organic molecules (COMs), particularly when traced through the development of larger COMs from shared precursors. Thus, while the detailed chemical composition differs between regions, the emergence of larger saturated COMs from common carbon reservoirs appears to follow a comparable evolutionary pattern. This is seen across quiescent low-mass clouds such as Taurus as well as more clustered star-forming environments within the Ophiuchus molecular cloud (Guilloteau et al. 2011; Andrews et al. 2009). In addition, complex organic molecules have been detected in a wide range of star-forming environments (Bacmann et al. 2012; Jiménez-Serra et al. 2016; Andrews 2020), indicating that chemical complexity can emerge under diverse physical conditions. Together, these observations suggest that while the physical framework governing star and disk formation is broadly shared across nearby star-forming environments, variations in physical conditions modulate the efficiency and relative importance of the processes operating within this framework. High-resolution observations with facilities such as the Atacama Large Millimeter/submillimeter Array (ALMA) have further established that protoplanetary disks are ubiquitous across a wide range of stellar masses and environments (Andrews 2020). In addition, the discovery of thousands of exoplanets indicates that planet formation is a common outcome of the star formation process. While the detailed architectures, compositions, and potential habitability of planetary systems remain diverse and incompletely constrained, these findings suggest that the formation of planetary systems, exemplified by the Solar System, is a widespread feature of star formation rather than an exceptional event.

A defining feature of star-forming regions is their chemical richness. To date, over 300 molecular species have been identified in the interstellar medium (ISM), ranging from simple diatomics such as CO and CN to more complex species including long carbon chains and complex organic molecules (CDMS database; Müller et al. 2005; Endres et al. 2016). These molecules are detected across a wide range of environments—from cold, quiescent molecular clouds to warm inner protostellar envelopes and the surfaces of protoplanetary disks—demonstrating a remarkable molecular diversity. This diversity arises as a natural consequence of the strong physical evolution that accompanies star formation: as dense molecular cloud cores collapse, they experience dramatic changes in density, temperature, and radiation field, which regulate the balance between gas-phase and solid-phase chemistry. Under these evolving conditions, processes such as gas-phase ion–molecule reactions, grain-surface radical–radical chemistry on icy mantles, and thermal and non-thermal desorption operate under non-equilibrium conditions and continuously reshape the chemical inventory. The widespread detection of molecules across star-forming

environments therefore implies that a common set of fundamental astrochemical reaction types operates throughout the star- and disk-formation process (Tielens 2013). At the same time, variations in physical conditions and evolutionary stage modulate the efficiencies and competition among these reactions, giving rise to diverse molecular abundances, isotopic compositions, and chemical histories. Among this rich molecular inventory, COMs (e.g., CH_3OH, CH_3CHO) are of particular interest because they represent key intermediates in the progression toward more complex and potentially prebiotic chemistry (Jørgensen et al. 2020). Their detection across cold prestellar cores, hot corinos, and disk atmospheres indicates that COM chemistry develops continuously from the molecular cloud phase into planet-forming disks. Furthermore, the presence of chemically related species—and in some cases comparable isotopic signatures—in comets and meteorites within our Solar System suggests that at least part of this interstellar chemical heritage can survive the star- and planet-formation process (Bergin et al. 2024). Having established this physical and chemical context, we next examine how variations in physical conditions shape the chemical evolution of COMs, with particular emphasis on prestellar and low-mass protostellar systems, which are most relevant for understanding the chemical origins of planetary compositions (Armitage 2011).

1.1.1 Physical Evolution in Prestellar and Low-Mass Protostellar Systems

The formation of low-mass stars proceeds through a sequence of evolutionary stages, each characterized by distinct physical conditions that strongly influence the local chemistry. These stages span from cold, quiescent prestellar cores to actively accreting protostars and their surrounding disks, and are linked by systematic changes in density, temperature, and radiation field as star formation progresses. Understanding this physical evolution is essential for interpreting the chemical signatures observed in star-forming regions. Prestellar cores represent the initial conditions of this process. They are typically cold (T = 10 K) and dense ($n \gtrsim 10^4$ cm^{-3}), such that thermal pressure alone is often insufficient to support the gas against self-gravity (Bergin & Tafalla 2007). A first-order description of gravitational instability is provided by the Jeans analysis, which defines the characteristic length and mass scales above which collapse can occur. For typical molecular cloud conditions, the resulting Jeans scales are of order 0.1–0.5 pc and $\sim$1 $M_\odot$, broadly consistent with the observed sizes and masses of prestellar cores (Ward-Thompson et al. 1999). However, real prestellar cores are finite in size, pressure-confined by their surroundings, and exhibit centrally concentrated density profiles. A more realistic

description of their internal structure is therefore provided by the Bonnor-Ebert (BE) sphere, an isothermal, self-gravitating gas sphere in hydrostatic equilibrium. Importantly, BE-like density profiles do not uniquely imply gravitational collapse. Depending on the ratio of the core mass to the critical Bonnor–Ebert mass, such cores may be stable (subcritical), marginally stable, or unstable (supercritical). Observational studies support this view: some starless cores, such as B68, are well described by stable BE configurations, whereas others, including L1544, appear to be supercritical and on the verge of collapse. These examples demonstrate that the BE sphere serves as a useful structural model for prestellar cores across different evolutionary states, rather than as a collapse model itself. The dynamical and chemical evolution of BE-like prestellar cores has been investigated in numerical models by Aikawa et al. (2005). Starting from a nearly critical BE sphere, they simulated the contraction of a dense core including radiative equilibrium and a comprehensive gas–grain chemical network. Their results showed that as the core contracts, CO significantly freezes out in the dense central region once the density exceeds $\sim 10^5$ cm^{-3}, while N_2H^+ becomes centrally enhanced due to the depletion of CO, which would otherwise destroy it. The freeze-out timescale decreases with increasing density, implying that chemical evolution and dynamical contraction proceed on comparable timescales in dense cores. These trends are consistent with observational signatures in prestellar cores such as L1544 and demonstrate that chemical differentiation can serve as a diagnostic of prestellar core evolution.

Once a prestellar core becomes supercritical, gravitational collapse starts, and the system enters a dynamically evolving phase. Several idealized self-similar solutions have been developed to describe isothermal collapse under simplified assumptions. The Larson-Penston solution represents a highly dynamical collapse from an unstable initial configuration (Larson 1969; Penston 1969), while the Shu inside-out solution assumes a singular isothermal sphere and describes a collapse that begins at the center after the formation of a protostar and propagates outward (Shu 1977). Although these solutions provide valuable reference cases for understanding limiting dynamical behavior, they rely on idealized initial conditions and neglect radiative transfer and thermal evolution.

In this study to model the physical evolution relevant for astrochemical calculations, we adopt the radiation-hydrodynamical model of Masunaga & Inutsuka (2000). This model follows the collapse of a BE-like core while self-consistently solving for the time-dependent evolution of density and temperature, from the onset of collapse through the formation of the first hydrostatic core and the subsequent protostellar stage. By accounting for the transition from isothermal to adiabatic evolution, the Masunaga & Inutsuka (2000) model provides the thermal history

required to describe key chemical processes such as molecular freeze-out, ice sublimation, and the re-distribution of material between solid and gas phases. In this sense, the model naturally encompasses different dynamical regions that resemble the limiting behaviors described by the Larson-Penston and Shu solutions at different stages of the collapse, while offering a more physically realistic description of low-mass star formation. For the purpose of chemical modeling, we further separate the physical evolution into a quasi-static prestellar phase and a subsequent collapse phase. During the static phase, the core is represented by a BE-like structure with constant physical conditions, allowing chemical evolution to proceed over extended timescales typical of observed prestellar cores (Aikawa et al. 2005). This phase is essential for establishing the chemical initial conditions of collapse. The collapse phase then follows the time-dependent physical evolution given by Masunaga & Inutsuka (2000) model, during which rapid changes in density and temperature drive processes such as ice sublimation and chemical reprocessing. This static–collapse framework is a modeling strategy designed to preserve the chemical history accumulated prior to collapse while enabling a self-consistent treatment of chemistry during protostellar evolution.

Finally, it is important to note that observational constraints on prestellar and protostellar cores are primarily obtained through molecular line emission. As a result, interpreting observations requires accurate predictions of molecular abundances and their spatial distributions. Models that couple physical evolution with time-dependent gas-grain chemistry have demonstrated that chemical differentiation naturally arises during core evolution and provides valuable diagnostics of the evolutionary stage (Aikawa et al. 2005). The physical framework described above therefore serves as the formation for the chemical modeling presented in the following sections.

1.2 Astrochemistry in the star-forming region

Astrochemistry, or molecular astrophysics, provides a powerful tool for tracing the physical evolution of star-forming regions(Herbst & van Dishoeck 2009; Tielens 2013). High-resolution observations have revealed a high degree of chemical complexity, which arises from a combination of gas-phase reactions, grain-surface chemistry, and radiation-driven processes (Garrod 2013). In particular, ion-molecule and neutral-neutral reactions in the gas phase, radical-driven chemistry on dust-grain surfaces, and photochemical processes induced by ultraviolet (UV) photons play central roles in shaping molecular abundances, with additional contributions from

cosmic rays through ionization and the generation of a weak internal UV field in shielded regions (Prasad & Tarafdar 1983). Rather than being governed by chemical equilibrium, molecular abundances are determined by kinetics and by the relative efficiencies of competing reactions, which depend sensitively on the local physical conditions and their temporal evolution. As density, temperature, and radiation fields vary during star formation, the dominant gas-phase and grain-surface processes vary with the physical environment, leading to chemical diversity. Accordingly, astrochemical modeling focuses on identifying the dominant reaction pathways under given physical conditions, rather than assuming that a single set of reactions governs chemistry in all environments. To understand the outcome of these processes, it is therefore essential to first identify the key elemental reservoirs that set the initial conditions for chemical evolution.

In astrochemistry, particular attention is paid to the major volatile carriers of the biogenic elements—carbon (C), oxygen (O), and nitrogen (N)—since they represent the chemical reservoirs that eventually feed into protoplanetary disks and planetary atmospheres (Bergin & Tafalla 2007). Here, "volatility" refers to the tendency of a substance to remain in the gas phase under interstellar conditions. The elemental abundances of these elements relative to hydrogen in the local ISM are approximately $[\mathrm{C}]/[\mathrm{H}] \sim 3 \times 10^{-4}$, $[\mathrm{O}]/[\mathrm{H}] \sim 4 \times 10^{-4}$, and $[\mathrm{N}]/[\mathrm{H}] \sim 7.5 \times 10^{-5}$ (Wilson & Rood 1994). Here, [X] denotes the total number density of element X, summed over all chemical forms. Thus, abundance ratios such as [C]/[H] represent elemental number density ratios. These values, along with the relative volatility and chemical reactivity of each element, influence the partitioning between gas-phase and ice-phase species in different environments, depending on the volatility of each molecule. These abundances provide the boundary conditions for chemical evolution as the ISM transitions from diffuse to dense phases. In the early stages of chemical evolution, such as in diffuse interstellar clouds ($n \lesssim 10^2$ cm^{-3}), a significant fraction of heavy elements is already locked into refractory dust grains (Jenkins 2009). Within the gas phase of diffuse clouds, the dominant form of carbon is C^+, while oxygen and nitrogen are largely atomic, reflecting their ionization energies and electron affinities.

As molecular clouds evolve from diffuse to dense conditions, the major volatile carriers of carbon, oxygen, and nitrogen undergo systematic chemical reorganization (Herbst & van Dishoeck 2009). Carbon gradually transitions from ionized and atomic forms (C^+ and C) into CO, which becomes the dominant carbon reservoir in dense gas. Oxygen is incorporated into CO and $\mathrm{H_2O}$, with relative partitioning depending on local physical conditions. Nitrogen chemistry proceeds more slowly; at higher densities and later stages, molecular nitrogen ($\mathrm{N_2}$) and ammonia ($\mathrm{NH_3}$)

become the principal nitrogen-bearing species. Because N_2 lacks a permanent dipole moment, its abundance is not directly observable and is commonly inferred from tracers such as N_2H^+. Interstellar dust grains play a central role in regulating these chemical transformations. Although dust accounts for only about 1% of the mass of the interstellar medium, grains play a central role in astrochemical evolution. They provide surfaces for chemical reactions that are inefficient or inaccessible in the gas phase, enabling the formation of key species such as H_2, H_2O, CO_2, and CH_3OH (Hasegawa et al. 1992), and they attenuate ultraviolet radiation, allowing molecules to survive in shielded regions of dense clouds(Draine 2003). As densities increase and temperatures remain low, many volatile species freeze out onto grain surfaces, forming icy mantles. Within these ice layers, chemistry driven by atomic accretion, surface diffusion, and irradiation leads to the formation of more complex molecules. These icy mantles therefore act as reservoirs that store the chemical inventory inherited by collapsing cores and, ultimately, by protoplanetary disks.

The conversion of elemental carbon, oxygen, and nitrogen into their dominant molecular and ice-phase reservoirs therefore defines the initial chemical conditions of dense cores. Understanding when and how these elements become locked into species such as CO, H_2O, CO_2, NH_3, and N_2 is essential for modeling the chemical evolution during subsequent stages of star and planet formation. In the following sections, I outline the key reaction pathways that govern this transformation.

1.3 Dominant Reaction Pathways in Astrochemistry

The chemical complexity observed in star-forming regions arises from a rich interplay between gas-phase and solid-phase (ice) chemistry. These processes operate under non-equilibrium conditions and are highly sensitive to local variations in density, temperature, and radiation field. In this section, I outline the dominant chemical mechanisms that shape the molecular inventory from dense cores to protostellar environments. To describe the chemical evolution, we adopt a rate-equation approach that follows the time evolution of species abundances per unit volume (McElroy et al. 2013). For a generic reaction channel r producing species i, the rate equation is written as

$$\frac{dn_i}{dt} = \sum_r P_{i,r} - \sum_r L_{i,r} \tag{1.1}$$

where $P_{i,r}$ and $L_{i,r}$ denote the production and loss terms associated with reaction r, respectively. The form of each term depends on whether the reaction occurs in the

gas phase or on grain surfaces.

1.3.1 Gas-Phase Chemistry

Gas-phase chemical reactions play a fundamental role in shaping molecular abundances throughout star-forming regions. The dominant classes of gas-phase reactions include ion–molecule processes, dissociative recombination, charge transfer, radiative association, and neutral–neutral reactions. The relative importance of these reaction pathways depends on local physical conditions such as temperature, density, and ionization rate. Reaction rate coefficients adopted in astrochemical models are compiled in databases such as KIDA (Wakelam et al. 2012), OSU (Prasad & Huntress 1980), and UDfA (Woodall et al. 2007; McElroy et al. 2013). For a two-body gas-phase reaction,

$$\mathrm{A} + \mathrm{B} \rightarrow \mathrm{C},$$

the production term is written as

$$P_{\mathrm{C}} = k_{\mathrm{gas}}\, n_{\mathrm{A}}\, n_{\mathrm{B}},$$

where k_{gas} is the gas-phase rate coefficient with units of $\mathrm{cm^3\,s^{-1}}$.

Ion–Molecule Reactions

Ion–molecule reactions generally occur without activation barriers and proceed efficiently at low temperatures in cold interstellar environments ($T \sim 10$–30 K) due to long-range Coulomb or ion–dipole interactions. Their rate coefficients are typically estimated by either the Langevin expression (for non-polar neutrals) (Langevin 1905) or the Su–Chesnavich formalism (for polar neutrals) (Su & Chesnavich 1982), depending on the polarity of the neutral reactant. Langevin rate coefficient:

$$k_{\mathrm{L}} = 2\pi e \sqrt{\frac{\alpha}{\mu}} \quad [\mathrm{cm^3\,s^{-1}}], \tag{1.2}$$

where α is the polarizability of the neutral molecule and μ is the reduced mass. Su–Chesnavich expression (for polar neutrals):

$$k_{\mathrm{D}}(T) = k_{\mathrm{L}} \times f(x), \tag{1.3}$$

with temperature dependence entering via:

$$x = \frac{\mu_{\mathrm{D}}}{\sqrt{2\alpha k_{\mathrm{B}} T}}, \tag{1.4}$$

and $f(x)$ being a function defined piecewise by the value of x. Models such as OSU use this temperature-dependent form explicitly, while UDfA often applies an empirical approximation:

$$k(T) = k(300\,\mathrm{K}) \left(\frac{300\,\mathrm{K}}{T} \right)^{1/2}. \tag{1.5}$$

Ion–molecule reactions are particularly important in dense cores, where ionization is maintained by cosmic rays (Herbst & Klemperer 1973). Cosmic rays ionize molecular hydrogen,

$$\mathrm{H_2} + \mathrm{CR} \rightarrow \mathrm{H_2^+} + \mathrm{e^-},$$

and the resulting $\mathrm{H_2^+}$ rapidly reacts with another $\mathrm{H_2}$ molecule to form

$$\mathrm{H_2^+} + \mathrm{H_2} \rightarrow \mathrm{H_3^+} + \mathrm{H}.$$

In addition to this primary ionization, the energetic electrons produced in cosmic-ray interactions induce secondary excitation of $\mathrm{H_2}$, effectively enhancing the ionization rate in well-shielded regions when excited $\mathrm{H_2}$ transfers to the ground state and emits UV radiation. The resulting $\mathrm{H_3^+}$ then drives much of the ion-molecule chemistry in cold gas. A canonical example is the formation of $\mathrm{HCO^+}$:

$$\mathrm{CO} + \mathrm{H_3^+} \rightarrow \mathrm{HCO^+} + \mathrm{H_2}.$$

The rate coefficient for this reaction is typically $k \sim 1 \times 10^{-9}\,\mathrm{cm^3\,s^{-1}}$ and is only weakly dependent on temperature in cold clouds (10–100 K).

Dissociative Recombination

Dissociative recombination (DR) reactions involve the destruction of molecular ions by electrons and the production of neutral fragments (Hollenbach & Tielens 1999). DR rate coefficients depend on temperature through the electron velocity distribution and are commonly described by a power-law scaling:

$$k(T) = \alpha \left(\frac{T}{300\,\mathrm{K}} \right)^{\beta} \tag{1.6}$$

For example:

$$\mathrm{HCO^+} + \mathrm{e^-} \rightarrow \mathrm{CO} + \mathrm{H}$$

Such reactions are critical for shaping the ionization fraction and regulating molecular lifetimes. Different models may adopt slightly different branching ratios or temperature scaling based on laboratory experimental or theoretical data.

Neutral–Neutral Reactions

Neutral–neutral reactions are commonly described using the modified Arrhenius expression:

$$k(T) = \alpha \left(\frac{T}{300\,\mathrm{K}} \right)^{\beta} \exp\left(\frac{-\gamma}{T} \right),$$

where α is the pre-exponential factor, β accounts for temperature-dependent collision frequency, and γ is the activation energy expressed in Kelvin.

Although this general expression applies to all neutral–neutral reactions, the values of γ and α vary significantly depending on whether the reactants are radicals or closed-shell molecules. Reactions involving radicals (e.g., CH_3 + O) often exhibit little to no activation barrier and can proceed efficiently even at low temperatures. In contrast, reactions between two closed-shell neutrals (e.g., O_2 + H_2) typically require higher temperatures due to larger activation barriers (Tielens 2013). For example:

$$\mathrm{CH_3 + O \rightarrow H_2CO + H} \quad (\gamma \approx 0)$$
$$\mathrm{O_2 + H_2 \rightarrow H_2O_2} \quad (\gamma \gtrsim 2000\,\mathrm{K})$$

Radiative Association

Radiative association involves the stabilization of an intermediate complex by photon emission, which is inherently a slow process (Herbst & Klemperer 1973). Typical examples include reactions such as

$$\mathrm{C^+ + H_2 \rightarrow CH_2^+ + h\nu}$$

or

$$\mathrm{H + H \rightarrow H_2 + h\nu},$$

where the absence of a third body requires radiative stabilization. Radiative association reactions are inherently slower than typical Langevin-type ion–neutral reactions because stabilization of the reaction complex relies on photon emission rather than collisional energy transfer. As a result, rate coefficients are generally small, often of order 10^{-15}–10^{-16} $\mathrm{cm^3 s^{-1}}$ for simple systems, but can be significantly larger for reactions leading to larger molecular products with many internal degrees of freedom.

1.3.2 Isotope Fractionation Processes in the Gas Phase

All chemical elements in the Universe typically exist in the form of multiple stable isotopes. The relative abundances of these isotopes, referred to as elemental isotope ratios, are generally set by primordial nucleosynthesis in the early Universe and by stellar nucleosynthesis over cosmic timescales.(Wilson & Rood 1994) In cold interstellar environments such as molecular clouds, there are no nuclear processes energetic enough to alter the elemental isotope composition significantly. Therefore, each isotope ratio can be regarded as having a reference value that is conserved locally, except over long timescales involving stellar evolution and feedback (e.g., supernovae or AGB winds). Representative elemental isotope ratios commonly adopted for the local interstellar medium are summarized in Table 1.1 and serve as reference values for the isotope fractionation processes discussed below.

However, chemical reactions can redistribute isotopes among different molecular species even when the elemental ratio remains fixed. This process, known as *isotope fractionation*, arises mainly from differences in zero-point vibrational energies and masses between isotopologues (Langer et al. 1984a), molecules that differ only in their isotopic composition, such as H_2O and HDO or CO and $^{13}C^{18}O$. Even small energy differences (on the order of a few tens of Kelvin) can significantly affect reaction rates or equilibrium constants in the cold environments ($T \lesssim 30$ K) typical of molecular clouds(Langer et al. 1984a). In addition to such chemical fractionation processes, isotope-selective photodissociation plays an important role for certain elements, particularly nitrogen and oxygen, in regions exposed to ultraviolet radiation (van Dishoeck & Black 1988a). In the following, however, we focus on gas-phase and grain-surface fractionation processes relevant to ^{13}C-bearing species.

Understanding isotope fractionation has become a key diagnostic tool in astrochemistry, particularly in the study of star and planet formation. Because isotopologue abundance ratios depend sensitively on the dominant formation pathways and on the physical conditions—such as temperature and density—under

Table 1.1:: Representative elemental isotope ratios in the local interstellar medium, commonly adopted as reference values in astrochemical models.

Element	Isotope ratio	Reference
Carbon	$^{12}C/^{13}C \sim 60$–70	Milam et al. (2005a)
Nitrogen	$^{14}N/^{15}N \sim 300$	Adande & Ziurys (2012)
Oxygen	$^{16}O/^{18}O \sim 500$	Wilson & Rood (1994)
Hydrogen	$D/H \sim 1.5 \times 10^{-5}$	Linsky (2003)

which a molecule forms, its isotopic composition may become effectively fixed at the time of formation. Measuring isotope ratios in prestellar and protostellar environments and comparing them with Solar System values can therefore provide powerful constraints on the physical conditions and chemical history that shaped our planetary system. The increasing availability of sensitive observational facilities, such as the IRAM 30m telescope, the Green Bank Telescope (GBT), and ALMA, has recently made such studies more feasible. These efforts are further complemented by in situ measurements of cometary materials (e.g., the Rosetta mission to 67P/Churyumov–Gerasimenko), providing benchmarks for early Solar System isotope compositions.

Carbon Isotope Fractionation

Carbon isotope fractionation in the interstellar medium (ISM) is governed by a combination of well-identified physical and chemical processes, including exothermic isotope exchange reactions, isotope-selective photodissociation, and differences in binding energies between isotopologues (Nomura et al. 2023). Deuterium and nitrogen isotope fractionation provide highly sensitive tracers of physical conditions, such as temperature, density, and radiation environment. However, because D and N isotopes primarily reflect environmental conditions rather than the assembly of molecular backbones, their isotopic signatures are often less directly linked to the specific formation pathways of complex organic molecules. In contrast, carbon isotopic compositions—including isotopomer-resolved patterns—can more directly constrain COM formation chemistry, because the carbon skeletons of COMs are assembled from a limited number of small precursor reservoirs. In astrochemical environments, these reservoirs, including C^+, CO, CH_x, and CN, are characterized by distinct $^{12}C/^{13}C$ signatures that are redistributed through well-defined reaction networks. As a result, carbon isotope ratios, and in particular their position-specific distributions within molecules, provide a powerful diagnostic of the chemical pathways and precursor reservoirs involved in the formation of COMs. One of the most important mechanisms driving carbon isotope fractionation in cold molecular clouds is exothermic isotope exchange reactions. Because of the zero-point vibrational energy difference between ^{12}C- and ^{13}C-bearing isotopologues, these reactions can efficiently redistribute ^{13}C among molecular species at low temperatures. A key reaction is

$$^{13}C^+ + {}^{12}CO \rightleftharpoons {}^{12}C^+ + {}^{13}CO + \Delta E, \tag{1.7}$$

where the energy difference is $\Delta E \simeq 35$ K (Watson et al. 1976). At temperatures of $\sim$20 K, the forward reaction is favored, leading to enrichment of ^{13}CO and depletion

of ^{13}C in the C^+ reservoir.

In their seminal gas-phase astrochemical models, Langer et al. (1984b) incorporated this mechanism and demonstrated that carbon-bearing molecules can be broadly divided into two groups: ^{13}C-rich species formed from CO-related reservoirs and ^{13}C-poor species formed from C^+-derived carbon. Importantly, observational studies later revealed that such fractionation is not only reflected in bulk $^{12}C/^{13}C$ ratios across different molecules, but can also appear as anomalies among isotopologues and isotopomers. For example, the "^{13}C depletion" in CCH isotopologues observed toward cold dense clouds provided a clear empirical demonstration that C^+-related carbon can become ^{13}C-poor compared to CO-related carbon, consistent with the exchange-reaction framework (Sakai et al. 2010). A broader set of observational constraints on anomalous ^{13}C abundances in carbon-chain molecules, including species larger than CCH, further supported the view that fractionation is distributed non-uniformly across the carbon network, and explicitly discussed the connection to the Langer-type theoretical picture (Sakai et al. 2013). Subsequent studies extended the exchange-reaction framework by identifying additional reactions that redistribute ^{13}C among small carbon chains, such as $^{13}C + C_3 \rightleftharpoons {}^{12}C + {}^{13}CC_2 + 28$ K, based on quantum chemical calculations (Roueff et al. 2015; Colzi et al. 2020; Loison et al. 2020). These reactions have been shown to reproduce the large carbon isotope fractionations observed in small hydrocarbons and nitriles in dense clouds (e.g., $C_2H/{}^{13}CCH > 250$, Sakai et al. 2010; $HC_3N/H{}^{13}CCCN \sim 80$, Takano et al. 1998). For clarity, the carbon isotope exchange reactions adopted in this work are summarized in Table 1.2. Crucially, the observational discovery of position-dependent ^{13}C within a single molecule predates many isotopomer-resolved modeling efforts. Early measurements in cold clouds showed that isotopomers can exhibit distinct abundances (i.e., distinct site-specific $^{12}C/^{13}C$ ratios), demonstrating that intramolecular isotope information is, in principle, observable and can encode formation chemistry (Takano et al. 1998). This observational fact motivates isotopomer-resolved chemical modeling: any theory that aims to connect carbon reservoirs to molecular synthesis must explain not only molecule-to-molecule fractionation but also site-to-site fractionation within a molecule.

Carbon isotope fractionation can also arise from isotope-selective photodissociation of CO and from differences in binding energies between isotopologues. Self-shielding of ^{12}CO against ultraviolet photodissociation can enhance the relative abundance of ^{13}C-bearing species in regions of moderate visual extinction ($A_V \sim 1$ mag; van Dishoeck & Black 1988b; Visser et al. 2009). In addition, laboratory experiments and theoretical studies indicate that ^{13}CO has a slightly

Table 1.2:: Carbon isotopic exchange reactions and adopted forward rate coefficients (k_f).

Label	Reaction	k_f ($\mathrm{cm^3\ s^{-1}}$)	$f(B,m)^{(a)}$	$\Delta E^{(b)}$ (K)	References
		C isotopic exchange reactions.			
(1)	$^{13}C^+ + CO \rightleftharpoons {}^{12}C^+ + {}^{13}CO$	$6.6\times10^{-10}\left(\frac{T}{300}\right)^{-0.45}\exp(-6.5/T)\ \frac{1}{1+\exp(-34.7/T)}$	1	34.7	(2)
(2)	$^{13}CO + HCO^+ \rightleftharpoons CO + H^{13}CO^+$	$2.6\times10^{-10}\left(\frac{T}{300}\right)^{-0.4}\ \frac{1}{1+\exp(-17.4/T)}$	1	17.4	(2)
(3)	$^{13}C^+ + CN \rightleftharpoons {}^{12}C^+ + {}^{13}CN$	$3.82\times10^{-9}\left(\frac{T}{300}\right)^{-0.4}\ \frac{1}{1+\exp(-31.1/T)}$	1	31.1	(2)
(4)	$^{13}C + CN \rightleftharpoons {}^{12}C + {}^{13}CN$	$3.0\times10^{-10}\ \frac{1}{1+\exp(-31.1/T)}$	1	31.1	(2)
(5)	$^{13}C + C_2 \rightleftharpoons {}^{12}C + {}^{13}CC$	$3.0\times10^{-10}\ \frac{2}{2+\exp(-25.9/T)}$	2	25.9	(2)
(6)	$^{13}C^+ + C_2 \rightleftharpoons {}^{12}C^+ + {}^{13}CC$	$1.86\times10^{-9}\ \frac{2}{2+\exp(-25.9/T)}$	2	25.9	(2)
(7)	$^{13}C^+ + {}^{13}CC \rightleftharpoons {}^{12}C^+ + {}^{13}C_2$	$1.86\times10^{-9}\ \frac{0.5}{0.5+\exp(-26.4/T)}$	0.5	26.4	(2)
(8)	$^{13}C + {}^{13}CC \rightleftharpoons {}^{12}C + {}^{13}C_2$	$3.0\times10^{-10}\ \frac{0.5}{0.5+\exp(-26.4/T)}$	0.5	26.4	(2)
(9)	$^{13}C^+ + CS \rightleftharpoons {}^{12}C^+ + {}^{13}CS$	$1.86\times10^{-9}\ \frac{1}{1+\exp(-26.3/T)}$	1	26.3	(2)
(10)	$^{13}C + C_3 \rightleftharpoons {}^{12}C + {}^{13}CC_2$	$3.0\times10^{-10}\ \frac{2}{2+\exp(-27/T)}$	2	27	(2)
(11)	$^{13}C^+ + C_3 \rightleftharpoons {}^{12}C^+ + {}^{13}CC_2$	$1.8\times10^{-9}\ \frac{2}{2+\exp(-27/T)}$	2	27	(2)
(12)	$^{12}C^+ + {}^{13}CCC \rightleftharpoons {}^{12}C^+ + C^{13}CC$	$1.8\times10^{-9}\ \frac{0.5}{0.5+\exp(-16/T)}$	0.5	16	(2), (3)
(13)	$^{13}C^+ + C_3 \rightleftharpoons {}^{12}C^+ + C^{13}CC$	$1.8\times10^{-9}\ \frac{1}{1+\exp(-43/T)}$	1	43	(4)
(14)	$^{12}C + {}^{13}CCC \rightleftharpoons {}^{12}C + C^{13}CC$	$3.0\times10^{-10}\ \frac{0.5}{0.5+\exp(-16/T)}$	0.5	16	(2), (3)
(15)	$^{13}C + C_3 \rightleftharpoons {}^{12}C + C^{13}CC$	$3.0\times10^{-10}\ \frac{1}{1+\exp(-43/T)}$	1	43	(4)
(16)	$^{13}C + {}^{13}CC_2 \rightleftharpoons {}^{12}C + C^{13}C_2$	$3.0\times10^{-10}\ \frac{1}{1+\exp(-43/T)}$	1	43	(4)
(17)	$^{13}C + C^{13}CC \rightleftharpoons {}^{12}C + C^{13}C_2$	$3.0\times10^{-10}\ \frac{2}{2+\exp(-27/T)}$	2	27	(4)
(18)	$^{13}C^+ + {}^{13}CC_2 \rightleftharpoons {}^{12}C^+ + C^{13}C_2$	$1.8\times10^{-9}\ \frac{1}{1+\exp(-43/T)}$	1	43	(4)
(19)	$^{13}C^+ + C^{13}CC \rightleftharpoons {}^{12}C^+ + C^{13}C_2$	$1.8\times10^{-9}\ \frac{2}{2+\exp(-27/T)}$	2	27	(4)
(20)	$^{13}C + HCN \rightleftharpoons {}^{12}C + H^{13}CN$	$2.0\times10^{-10}\ \frac{1}{1+\exp(-48/T)}$	1	48	(3)
(21)	$^{13}C + HNC \rightleftharpoons {}^{12}C + HN^{13}C$	$3.0\times10^{-11}\ \frac{1}{1+\exp(-33/T)}$	1	33	(3)
(22)	$^{13}C + HCNH^+ \rightleftharpoons {}^{12}C + H^{13}CNH^+$	$1.0\times10^{-9}\ \frac{1}{1+\exp(-50/T)}$	1	50	(3)
(23)	$^{13}C + CS \rightleftharpoons {}^{12}C + {}^{13}CS$	$2.0\times10^{-10}\ \frac{1}{1+\exp(-26.3/T)}$	1	26.3	(3)
(24)	$H^+ + {}^{13}CCH \rightleftharpoons H^+ + C^{13}CH$	$2.0\times10^{-10}\ \frac{1}{1+\exp(-8.1/T)}$	1	8.1	(3)
(25)	$H^+ + {}^{13}CCS \rightleftharpoons H^+ + C^{13}CS$	$4.0\times10^{-11}\ \frac{1}{1+\exp(-18/T)}$	1	18	(3)
(26)	$HCNH^+ + H^{13}CN \rightleftharpoons H^{13}CNH^+ + HCN$	$2.0\times10^{-9}\left(\frac{T}{300}\right)^{-0.5}\ \frac{1}{1+\exp(-2.9/T)}$	1	2.9	(3)
(27)	$HCNH^+ + HN^{13}C \rightleftharpoons H^{13}CNH^+ + HCN$	$1.0\times10^{-9}\left(\frac{T}{300}\right)^{-0.5}$	1	0	(3)
(28)	$HCNH^+ + HN^{13}C \rightleftharpoons HCNH^+ + H^{13}CN$	$1.0\times10^{-9}\left(\frac{T}{300}\right)^{-0.5}$	1	0	(3)
(29)	$^{13}C + HC_3N \rightleftharpoons {}^{12}C + H^{13}CCCN$	$2.0\times10^{-11}\ \frac{1}{1+\exp(-48.3/T)}$	1	48.3	(3)
(30)	$^{13}C + HC_3N \rightleftharpoons {}^{12}C + HC^{13}CCN$	$2.0\times10^{-11}\ \frac{1}{1+\exp(-57.4/T)}$	1	57.4	(3)
(31)	$^{13}C + HC_3N \rightleftharpoons {}^{12}C + HCC^{13}CN$	$2.0\times10^{-11}\ \frac{1}{1+\exp(-60.0/T)}$	1	60.0	(3)

Notes. (a) $f(B,m)$ is a probability factor that depends on the rotational constant, mass, and symmetry factors of the reactants and products. In reactions involving ^{13}C, the mass ratio of the reactants and the products is close to unity. Then, $f(B,m) = q(C)q(D)/[q(A)q(B)]$, where A and B are the reactants, C and D the products, and $q(\ldots)$ are the internal molecular partition functions. (b) ΔE is the exoergicity of the exchange reaction in the forward direction.

References. (1) Roueff et al. (2015); (2) Colzi et al. (2020); (3) Loison et al. (2020); (4) Sipilä et al. (2023).

higher binding energy on grain surfaces than ^{12}CO, by typically a few kelvin (corresponding to less than a one-percent difference in absolute binding energy) (Smith et al. 2015, 2021). As a consequence, solid-phase carbon reservoirs can become ^{13}C-enriched relative to the gas phase, potentially imprinting isotope signatures onto molecules formed on or within interstellar ices.

Observational evidence for such processes has been reported for COMs in

protostellar environments. In particular, COMs observed toward IRAS 16293–2422B, such as glycolaldehyde and dimethyl ether, exhibit ^{13}C enrichments of up to a factor of two relative to the local ISM elemental ratio (Jørgensen et al. 2016, 2018). These enrichments have been interpreted as reflecting the incorporation of ^{13}C-enriched carbon reservoirs, potentially originating from isotope-selective photodissociation of CO, while additional processes affecting the availability of carbon isotopologues on grain surfaces may also contribute.

While bulk ^{12}C/^{13}C ratios reflect the average isotopic composition of the carbon reservoirs from which a molecule is assembled, they do not uniquely constrain how individual carbon atoms are incorporated. This limitation is particularly important for COMs, which contain multiple carbon atoms distributed among chemically distinct functional groups. In such molecules, different carbon atoms may originate from different precursor reservoirs and chemical pathways, even when the bulk isotope ratio appears uniform. Despite this, most astrochemical models have so far treated carbon isotope fractionation only at the molecular level, without tracking the positional distribution of ^{13}C within COMs. As a result, the connection between observed intramolecular isotope patterns in COMs and their underlying formation pathways remains poorly constrained. In particular, it is still unclear how distinct carbon reservoirs, such as CO-, C^+-, or CH_x-derived carbon, are incorporated into specific functional groups during COMs formation in the ice phase and in the gas phase. The positional distribution of ^{13}C within a molecule, referred to as isotopomer-specific fractionation (Takano et al. 1998; Sakai et al. 2010), therefore offers a uniquely powerful probe of the COM formation pathway. Position-specific observations, though still limited, are rapidly increasing and suggest that intramolecular isotope information can be preserved under certain astrochemical conditions. Interpreting these observations requires chemical models that follow isotopomer-resolved reaction networks coupled to the physical evolution of star-forming regions. Addressing this challenge provides the primary motivation for the isotopomer-resolved modeling framework developed in this work.

1.3.3 Grain-Surface and Ice Chemistry

As the density of molecular clouds increases and temperatures drop, gas-phase species begin to accrete onto dust grains, forming ice mantles. The surfaces of interstellar dust grains serve as catalytic sites for chemical reactions that are often inefficient in the gas phase. In cold, dense regions of molecular clouds ($\sim$10 K), grain-surface chemistry becomes particularly important in the formation of saturated molecules, including COMs. Several mechanisms have been proposed for reactions on

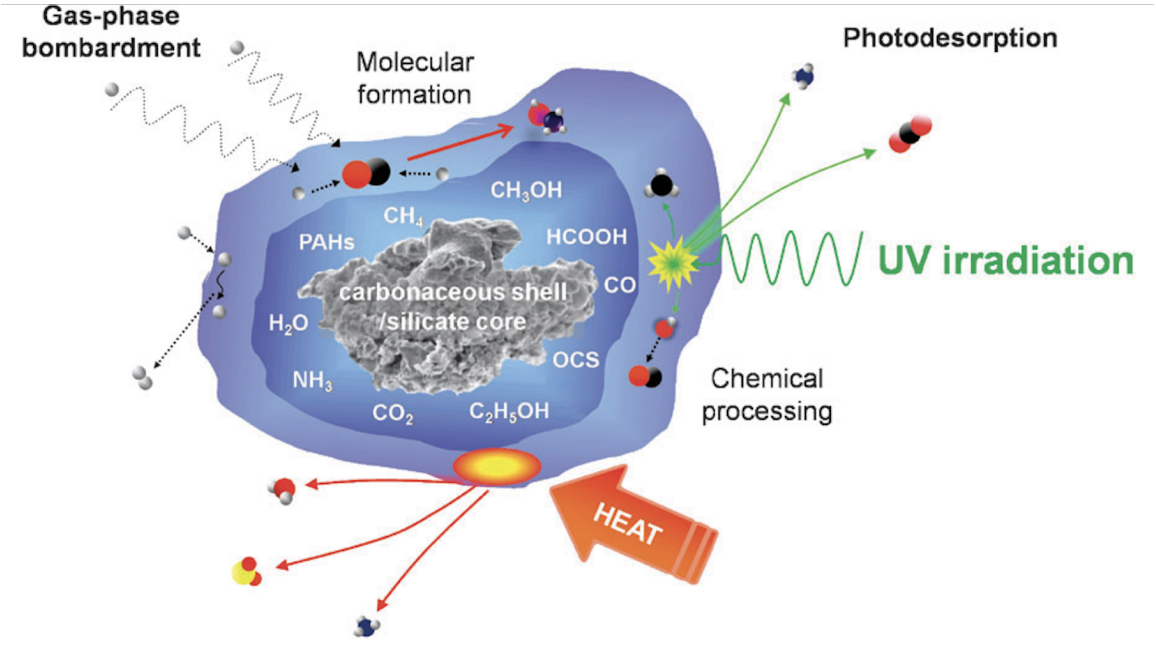

Figure 1.2: Common grain-surface chemical reactions in the ice phase Credit:Burke & Brown (2010), Figure 1.

dust and ice surfaces (Hasegawa & Herbst 1993) (see Figure 1.2). Surface reactions are treated using the rate-equation approach, in which the average number of species on a representative grain is followed (Hasegawa et al. 1992). For an LH-type reaction, the production term per unit volume is written as

$$P_{\mathrm{C}} = n_{\mathrm{d}}\, k_{\mathrm{LH}}\, N_{\mathrm{A}}\, N_{\mathrm{B}},$$

where n_{d} is the number density of dust grains, and N_{A} and N_{B} are the average numbers of species A and B, respectively, on a single grain.

Langmuir–Hinshelwood (LH) Mechanism on Dust Grains

One of the most important pathways for molecule formation on interstellar dust grains is the Langmuir–Hinshelwood (LH) mechanism (Langmuir 1918), in which two adsorbed species thermally diffuse across the grain surface and react upon encounter (Hollenbach & Salpeter 1970; Tielens & Hagen 1982). The efficiency of this process depends on the surface temperature, the binding and diffusion energies of the reactants, and the reaction barrier (Hasegawa et al. 1992; Cuppen et al. 2017). The rate coefficient k_{LH} of an LH-type surface reaction between species A and B can

be expressed as:

$$k_{\mathrm{LH}} = \frac{\kappa\,(R_{\mathrm{A}} + R_{\mathrm{B}})}{N_{\mathrm{site}}},$$

where κ is the reaction probability (evaluated either thermally or through quantum tunneling), R_{A} and R_{B} are the diffusion rates of species A and B, and N_{site} is the number of binding sites on a grain ($\sim 10^6$ for typical grains). The diffusion rate for species i is

$$R_i = \nu_i \exp\left(-\frac{E_{\mathrm{diff},i}}{k_{\mathrm{B}} T_{\mathrm{dust}}}\right),$$

where ν_i is the attempt frequency, $E_{\mathrm{diff},i}$ is the diffusion barrier, and T_{dust} is the dust temperature. The diffusion barrier is generally taken as a fraction ($\sim$0.3–0.5) of the binding energy $E_{\mathrm{bind,i}}$ (Cuppen et al. 2017):

$$E_{\mathrm{diff},i} \approx f \cdot E_{\mathrm{bind},i}, \quad f \sim 0.3\text{–}0.5.$$

For reactions with activation energy E_{A}, the reaction probability κ is evaluated either via thermal activation or quantum tunneling, depending on the physical conditions and the masses of the reacting species (Burke & Brown 2010; Hama & Watanabe 2013). For thermal activation,

$$\kappa_{\mathrm{th}} = \exp\left(-\frac{E_{\mathrm{A}}}{k_{\mathrm{B}} T_{\mathrm{dust}}}\right),$$

where T_{dust} is the grain temperature. For light particles such as H atoms, quantum tunneling through the reaction barrier can dominate, in which case κ is commonly approximated using a rectangular barrier of width a:

$$\kappa_{\mathrm{tun}} = \exp\left[-\frac{2a}{\hbar}\sqrt{2\mu E_{\mathrm{A}}}\right],$$

where μ is the reduced mass of the reacting system. This formalism enables LH-type chemistry to be incorporated quantitatively into astrochemical networks. In particular, reactions involving light atoms such as H are highly efficient even at low temperatures due to fast diffusion and tunneling, while reactions between heavier radicals become active mainly during the warm-up phase as surface mobility increases. The LH mechanism is implemented in many modern astrochemical models and plays a key role in the formation of COMs in both prestellar and protostellar environments (Garrod & Herbst 2006).

Eley–Rideal (ER) Mechanism

In contrast to the Langmuir–Hinshelwood (LH) mechanism, where both reactants are adsorbed on the grain surface and migrate thermally before reacting, the Eley–Rideal

(ER) mechanism (Rideal 1939) involves the direct interaction of a gas-phase species with a surface-adsorbed reactant. In this process, a gas-phase atom or molecule collides with the grain and reacts essentially instantaneously with a partner already present on the surface, without requiring prior adsorption or diffusion (Ruffle & Herbst 2000; Ruaud et al. 2015).

The ER mechanism is expected to be particularly important under conditions where a highly reactive gas-phase species (such as atomic C) is abundant, surface diffusion is strongly suppressed at low dust temperatures ($\lesssim 10$ K), and the surface coverage of the target species (e.g., CO or H_2O) is sufficiently high that direct encounters are likely. Because ER reactions do not rely on thermal hopping, they can remain efficient in cold dense cores where the LH mechanism is largely inactive, providing a non-diffusive pathway for bringing reactants together under such conditions(Cuppen et al. 2017). The rate of an Eley–Rideal reaction can be expressed as

$$R_{\rm ER} = F_X \, n_{\rm gr} \, \pi a^2 \, \theta_Y \, \kappa, \tag{1.8}$$

where F_X is the incident flux of the gas-phase species X (e.g., atomic C), $n_{\rm gr}$ is the number density of dust grains, and a is the grain radius determining the geometrical cross section πa^2. The factor θ_Y denotes the fractional surface coverage of the adsorbed target species Y, while κ is the reaction probability per collision, which may include the effects of activation barriers and/or quantum tunneling. In this approach, the spatial search for reaction partners on grain surfaces is treated probabilistically through surface coverage factors, rather than being resolved as a time-dependent diffusion process (Ruaud et al. 2015; Jin & Garrod 2020).

Laboratory experiments and modeling studies increasingly suggest that ER-type processes can contribute to both simple and complex molecule formation on icy grains. Proposed examples include C-atom reactions with CO- and H_2O-containing ices leading to carbonyl-bearing species, as well as transient complex formation (e.g., $C\cdots CH_3OH$) followed by subsequent hydrogenation and rearrangement into more complex organic products (Molpeceres et al. 2021; Potapov et al. 2021; Fedoseev et al. 2022). These reactions therefore provide non-thermal formation channels that bypass diffusion barriers and may operate efficiently under low-temperature conditions where LH chemistry alone is insufficient. Despite remaining uncertainties in cross sections and sticking probabilities, the inclusion of ER-type chemistry in astrochemical models is increasingly recognized as essential to reproduce observed abundances of complex molecules in prestellar and protostellar environments.

Cosmic-Ray-Induced Ice Radiolysis and Suprathermal Chemistry

In addition to diffusive and non-diffusive surface reaction pathways, such as the Langmuir–Hinshelwood and Eley–Rideal mechanisms, energetic processing of icy grain mantles by cosmic rays and secondary electrons can fundamentally alter ice chemistry. When a high-energy cosmic ray penetrates a dust grain, it deposits energy into the ice matrix, inducing ionization and electronic excitation of ice constituents (Bohr 1913; Spinks & Woods 1990). This process, known as radiolysis, produces chemically "hot" suprathermal fragments with excess internal and kinetic energy. Because these species are formed with substantial excitation energy, they are capable of overcoming activation barriers and reacting on timescales far shorter than those associated with thermal diffusion. As demonstrated by Shingledecker et al. (2018), such non-thermal chemistry provides an additional pathway toward molecular complexity in cold astrophysical environments. At the microscopic level, radiolysis is initiated by collisions between a target species A in the ice and either a primary cosmic-ray particle or secondary electrons generated along the cosmic-ray track. These interactions trigger a cascade of relaxation processes that can be schematically represented by

$$\mathrm{A} \rightsquigarrow \mathrm{A}^+ + e^- \rightarrow \mathrm{A}^* \rightarrow b\,\mathrm{B}^* + c\,\mathrm{C}^*, \tag{1.9}$$

$$\mathrm{A} \rightsquigarrow \mathrm{A}^* \rightarrow b\,\mathrm{B} + c\,\mathrm{C}, \tag{1.10}$$

$$\mathrm{A} \rightsquigarrow \mathrm{A}^* \rightarrow \mathrm{A}. \tag{1.11}$$

Here, A denotes a parent ice species, A^* its electronically or vibrationally excited suprathermal state, and B and C chemically active daughter fragments; b and c are stoichiometric coefficients. Reaction 1.9 corresponds to ionization followed by dissociation into excited fragments (Type I), 1.10 to dissociation after rapid thermalization (Type II), and 1.11 to non-dissociative excitation (Type III). The suprathermal products generated in these processes may subsequently undergo rapid secondary reactions before thermalizing within the ice mantle. In quantitative astrochemical models, radiolysis is described using the radiochemical yield, or G-value, defined as the number of molecules produced (or destroyed) per 100 eV of energy deposited in the ice. Following Shingledecker et al. (2018), the first-order rate coefficient for radiolysis of species i is expressed as

$$k_i = \frac{G_i}{100\,\mathrm{eV}}\, S_e\, \Phi_{\mathrm{CR}}, \tag{1.12}$$

where G_i is the channel-specific G-value, S_e is the electronic stopping cross section (energy deposited per unit path length) (Spitzer & Tomasko 1968), and Φ_{CR} is the

flux of penetrating cosmic-ray particles (Johnson 1990). The effective rate of an individual reaction channel is further weighted by its branching fraction $f_{\rm br}$,

$$k_{i\to j} = f_{\rm br}\, k_i. \tag{1.13}$$

This formalism links the microscopic excitation cascade initiated by cosmic-ray impacts to macroscopic rate coefficients implemented in chemical networks. In contrast to thermal diffusion-driven chemistry, which becomes efficient mainly during warm-up phases, radiolysis-driven chemistry can proceed even in cold, quiescent dense cores. By enabling barrier-crossing reactions, bond rearrangements, and functional-group formation in the bulk ice, cosmic-ray-induced suprathermal chemistry may substantially modify both the molecular inventories and isotopic signatures of complex organic molecules.

Although significant uncertainties remain, including quantitative yields, branching ratios, and the efficiency of energy redistribution in realistic astrophysical ices, radiolysis is now recognized as an important process that should be considered in models of ice chemistry in star-forming environments. Together with diffusive and other non-diffusive surface processes, cosmic-ray-induced suprathermal chemistry provides a complementary and potentially dominant contribution to the chemical evolution of interstellar ices in both prestellar and protostellar phases.

1.3.4 Gas–Grain Interaction

The interaction between the gas and solid phases plays a crucial role in the chemical evolution of star-forming regions. Key exchange processes include accretion of gas-phase species onto dust grains, thermal desorption due to temperature rise, and various non-thermal desorption mechanisms that operate even in cold environments. These interactions govern the availability of reactants in both the gas and ice phases and thereby influence the abundances and isotopic compositions of COMs (Tielens 2013; Cuppen et al. 2017).

Accretion. Neutral species in the gas phase can stick to grain surfaces through collisions. The rate coefficient for accretion per unit volume is given by

$$R_{\rm acc} = s\, n_X\, \langle v_X \rangle\, \pi a^2\, n_{\rm gr}, \tag{1.14}$$

where s is the sticking coefficient (typically $s \sim 1$ at $T \lesssim 20$ K), n_X is the number density of species X, $\langle v_X \rangle = \sqrt{8k_BT/(\pi m_X)}$ is the thermal velocity, a is the grain radius (typically 0.1 μm), and $n_{\rm gr}$ is the number density of grains. In cold dense

regions, accretion efficiently transfers heavy species from the gas to the solid phase, driving the build-up of icy mantles.

Thermal Desorption. Species thermally desorb from grain surfaces when the dust temperature exceeds their binding energy $E_{\rm des}$. The desorption rate per species is given by the Arrhenius expression

$$k_{\rm des} = \nu_0 \, \exp\left(-\frac{E_{\rm des}}{k_B T_{\rm dust}}\right), \tag{1.15}$$

where ν_0 is the characteristic attempt frequency, often taken to be 10^{12}–10^{13} s^{-1}, and $T_{\rm dust}$ is the grain temperature. The binding energy $E_{\rm des}$ depends on both the species and the substrate; for example, CO on water ice has $E_{\rm des} \sim 1300$ K (Minissale et al. 2016), while H_2O has $E_{\rm des} \sim 5700$ K (Fraser et al. 2001). Thermal desorption thus sets the sublimation fronts of volatile species and regulates the transition of COMs from ice to gas in warm regions.

Non-thermal Desorption. Desorption can also occur via mechanisms unrelated to the bulk dust temperature, including cosmic-ray-induced heating, photodesorption, and reactive desorption (Hasegawa & Herbst 1993). Cosmic-ray-induced transient heating occurs when energetic particles deposit energy into dust grains, briefly raising their temperature to $T \sim 70$ K and enabling desorption of weakly bound species even in otherwise cold environments. Photodesorption is driven by UV photons (either external or produced by cosmic rays), which can eject surface species into the gas. The rate is typically expressed as

$$R_{\rm pd} = Y \, F_{\rm UV} \, \theta_X, \tag{1.16}$$

where Y is the photodesorption yield (molecules photon^{-1}), $F_{\rm UV}$ is the photon flux (photons cm^{-2} s^{-1}), and θ_X is the surface coverage fraction of species X. Laboratory measurements have provided yields for a variety of astrophysically relevant ices such as CO, CO_2, H_2O, and simple organics.

Reactive desorption occurs when the energy released in an exothermic surface reaction leads to the immediate ejection of a fraction of the reaction products into the gas phase. A commonly used parameterization is

$$f_{\rm rd} = a \, \frac{E_{\rm rxn}}{E_{\rm rxn} + E_{\rm des}}, \tag{1.17}$$

where a is an empirical efficiency factor (typically ∼0.01–0.1), and $E_{\rm rxn}$ is the exothermicity of the reaction. Subsequent experimental and theoretical studies have

refined constraints on the efficiency of reactive desorption for different reaction classes, but it remains an important non-thermal route to maintain certain molecules in the gas phase in cold, dense regions.

Implications for Chemical Modeling. The balance between accretion and desorption dictates the lifetime and reactivity of molecules on grains. In cold environments ($T_{\rm dust} \lesssim 15$ K), thermal desorption is negligible for most species, and non-thermal desorption processes dominate the exchange between gas and ice. Accurate implementation of accretion and non-thermal desorption processes is essential to reproduce the observed abundances of both simple and complex molecules in dense clouds, protostellar envelopes, and protoplanetary disks.

Toward Physically Consistent Astrochemical Models Traditional chemical models, particularly those assuming static physical structures and thermal equilibrium, often fail to reproduce key molecular abundances observed in protostellar environments(Herbst & van Dishoeck 2009). For example, the formation of certain COMs or multiply-deuterated species requires consideration of transient warm-up events, radical-radical recombination on grain surfaces, or non-thermal desorption mechanisms—all of which depend on time-dependent changes in temperature, density, and irradiation (Garrod et al. 2008). This has led to a paradigm shift: chemical evolution in star-forming regions must be studied in the context of co-evolution with physical structure, where parameters such as gas/dust temperature, density profiles, UV flux, and dynamical timescales evolve concurrently. In this framework, chemistry becomes both a tracer and a consequence of physical evolution, and interpreting molecular signatures requires an integrated, time-resolved approach.

Nevertheless, significant uncertainties and open questions remain:

- Molecular inheritance vs. in-situ formation: It is unclear to what extent observed molecules in protostellar disks are inherited from earlier prestellar stages or are formed locally within the disk environment.
- Isotopic compositions and isotopomer distributions: Observations show variations in molecular $^{13}C/^{12}C$, $^{15}N/^{14}N$, and D/H ratios, as well as position-specific isotopomer enhancements. However, their chemical origins, dependence on formation pathways, and sensitivity to physical conditions remain poorly constrained.
- Chemical timescales and evolutionary markers: Determining the temporal evolution of molecular abundances and isotopic ratios across stages—prestellar

core, protostellar envelope, and disk—is essential for establishing chemical clocks, but current models lack sufficient observational and theoretical constraints.

These limitations underscore the need for advanced astrochemical models that are physically consistent, isotopically explicit, and capable of simulating the chemical evolution across multiple evolutionary phases under dynamically changing conditions.

1.4 Complex organic molecules and isotopic chemistry

COMs, sometimes referred to as interstellar complex organic molecules (iCOMs), constitute a class of carbon-bearing species that resemble small organic molecules familiar from terrestrial chemistry. Although termed "complex," these molecules typically contain only a few to a dozen atoms (six atoms or more) and are modest in size compared with biomolecules on Earth. Common examples include simple alcohols, ethers, esters, aldehydes, nitriles, and other functionalized hydrocarbons. COMs have been detected mainly through radio and millimeter/submillimeter spectroscopy and are now known to be widespread across a variety of star-forming environments (Jørgensen et al. 2018; Yamato et al. 2024).

COMs were first identified in warm, dense regions associated with massive and low-mass star formation, known respectively as hot cores and hot corinos (Bottinelli et al. 2004) (see Figure 1.3). These regions correspond to late stages of gravitational collapse, in which the innermost parts of the envelope are heated by the central protostar and dust temperatures locally exceed ∼100 K, leading to the sublimation of icy grain mantles and the release of previously formed molecules into the gas phase. Subsequent observational studies have shown that COMs are not exclusively present in such warm regions. Low-level abundances of selected COMs have also been detected in a variety of colder and dynamically different environments, including cold molecular clouds, prestellar cores, protostellar envelopes, and shocked regions associated with outflows (McGuire 2022). In these colder environments, COM abundances are typically several orders of magnitude lower than those observed in hot cores and hot corinos, and their detection generally requires high-sensitivity observations. This broad but highly non-uniform distribution indicates that COM formation is not confined to a single evolutionary stage or physical regime, but instead involves distinct chemical routes—including gas-phase reactions and ice-phase processes such as Langmuir–Hinshelwood 1.3.3, Eley–Rideal 1.3.3, and

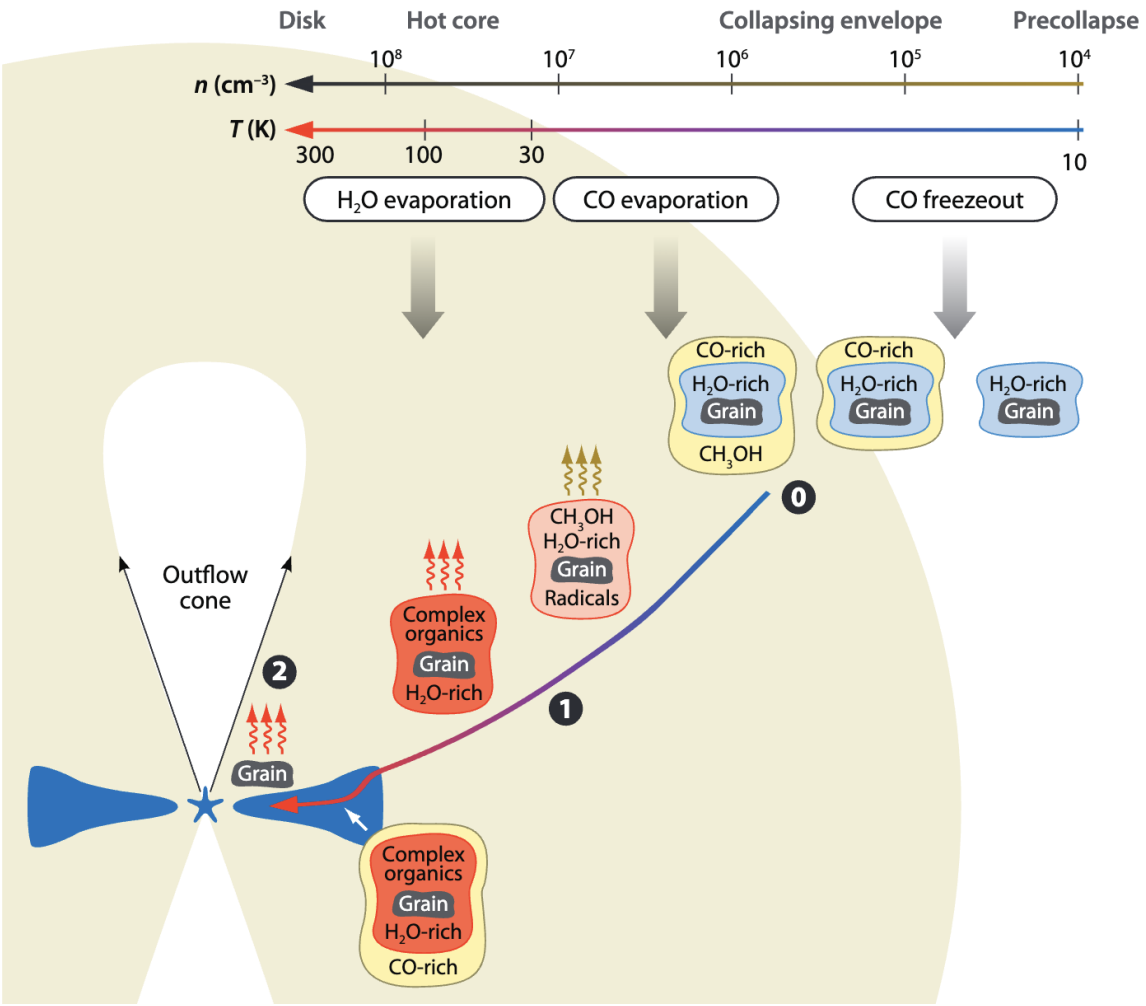

Figure 1.3: Schematic overview of the evolution of material from the prestellar core stage through the collapsing envelope (size ~ 0.05 pc) into a protoplanetary disk. The formation of zeroth- and first-generation organic molecules in the ices is indicated with 0 and 1, and the second-generation molecules in the hot-core/corino region when the envelope temperature reaches 100 K, and even strongly bound ices start to evaporate, are designated 2. Credit:Herbst & van Dishoeck (2009), Figure 14.

radiation-driven chemistry 1.3.3—whose relative efficiencies depend strongly on local physical conditions.

In the classical framework developed for hot cores and hot corinos, COMs synthesis proceeds through a two-step process. First, simple molecules and radicals are produced on icy dust-grain mantles during cold phases via atom-addition reactions and energetic processing by ultraviolet photons or cosmic rays. Second, as temperatures increase during protostellar collapse, radicals become mobile and

recombine on grain surfaces, or COMs are released into the gas phase, where additional chemical reactions may take place (Garrod & Herbst 2006). In colder environments ($T \sim 10$ K), where thermal diffusion on grain surfaces is inefficient, alternative non-thermal grain chemistry and gas-phase pathways have been proposed. In particular, non-diffusive grain-surface processes — such as chemically driven "chain-reaction" mechanisms, Eley–Rideal type reactions, and suprathermal chemistry triggered by energetic processing — have been shown to enable COMs formation even when thermal hopping is suppressed (Jin & Garrod 2020). Overall, it is now widely accepted that more than one formation mechanism contributes to the observed COMs population, and that the dominant pathways depend sensitively on the local physical conditions.

Because COMs are thought to form through reaction sequences starting from a limited set of small precursor species, their isotopic compositions provide a powerful probe of chemical history. Isotopic ratios can encode information about the physical conditions, dominant reaction channels, and precursor reservoirs involved in molecular synthesis, offering unique insights into the processes linking interstellar chemistry to the organic inventory of forming planetary systems (see Section 1.3.2).

To avoid ambiguity in terminology, we clarify our usage of carbon isotope and isotopomer ratios. The "carbon isotope ratio" refers to the abundance ratio between a molecule and its singly ^{13}C-substituted isotopologue, that is, the main isotopologue (^{12}CX) to each ^{13}C-bearing isotopologue (^{13}CX), where only one ^{12}C is replaced by ^{13}C. In molecules with multiple carbon atoms, this ratio is defined for each specific carbon position, corresponding to structurally distinct isotopomers such as $^{13}CH_3CHO$ and $CH_3{}^{13}CHO$. For symmetric molecules in which multiple carbon atoms are chemically and spectroscopically indistinguishable, the carbon isotope ratio is derived from the abundance ratio between the main isotopologue and the sum of all singly ^{13}C-substituted isotopologues, multiplied by a statistical factor equal to the number of equivalent carbon positions. For example, in the case of the C_3 molecule, the ^{13}C-substituted isotopomers ^{13}CCC and CC^{13}C are chemically equivalent due to the symmetry of the molecule. When defining the carbon isotope ratio from isotopomer abundances, the abundance of the main isotopologue (C_3) should be compared with the sum of the abundances of the two symmetry-equivalent singly ^{13}C-substituted isotopomers (CC^{13}C and ^{13}CCC), multiplied by a statistical factor of 2 to account for the two equivalent terminal carbon positions. The resulting expression for the ^{12}C/^{13}C ratio at the terminal carbon positions is therefore given by ^{12}C/^{13}C of terminal carbon = ([C_3]/([^{13}CCC]+[CC^{13}C]))×2. This statistical factor reflects the number of equivalent substitution sites and does not rely on observational separation of individual isotopomers. On the other hand, the central

carbon–substituted isotopomer $C^{13}CC$ is not equivalent to the terminal ones and can be treated separately. Thus, the carbon isotope ratio for the central position is simply given by: $^{12}C/^{13}C$ of central carbon = $[C_3]/[C^{13}CC]$. This correction allows estimation of the $^{12}C/^{13}C$ ratio per carbon position. A deviation of the carbon isotope ratio from the elemental abundance ratio of $[^{12}C/^{13}C]$ in the local ISM (e.g., 69) is referred to as "isotope fractionation". The "isotopomer ratio" refers specifically to the abundance ratio between two distinct singly ^{13}C-substituted isotopomers of a molecule with more than one carbon atom (e.g., $^{13}CH_3CHO$ / $CH_3{}^{13}CHO$). A deviation of this ratio from unity or statistical ratio indicates "isotopomer difference".

1.5 Observational benchmarks for isotopic studies of COMs

High-angular-resolution observations now provide a critical benchmark for testing astrochemical models of COMs, particularly with respect to their isotopic compositions. Among currently available sources, the low-mass protostellar system IRAS 16293–2422 (Figure 1.4), located in the ρ Ophiuchi cloud at a distance of $\sim$140 pc, has emerged as a key laboratory for isotopic studies of COMs owing to its chemical richness and proximity (Jørgensen et al. 2016). IRAS 16293–2422 is a deeply embedded Class 0 binary system consisting of two gravitationally bound components, IRAS 16293–2422A and IRAS 16293–2422B, separated by $\sim$600–700 au in projection. Both sources are embedded within a common envelope, and ALMA observations have revealed complex gas structures and possible material flows connecting the two components (Pineda et al. 2012; Jørgensen et al. 2016). These results suggest that dynamical and radiative interactions may influence the large-scale thermal and density structure of the system on scales of several hundred au. In this work, we focus on the compact hot corino associated with IRAS 16293–2422B. The B component exhibits a nearly face-on geometry and relatively narrow line widths, making it particularly suitable for isotopic analysis. High-resolution ALMA observations obtained as part of the Protostellar Interferometric Line Survey (PILS) achieve spatial resolutions of order $\sim$50–60 au, probing the warm ($\gtrsim$100 K) inner envelope where ices have thermally desorbed. The molecular column densities used in the PILS analysis are not derived directly toward the continuum peak of the protostar, where the dust emission becomes optically thick, but instead from a nearby offset position representative of the hot corino gas (Jørgensen et al. 2016). This position lies within the warm inner envelope of source B at a projected distance

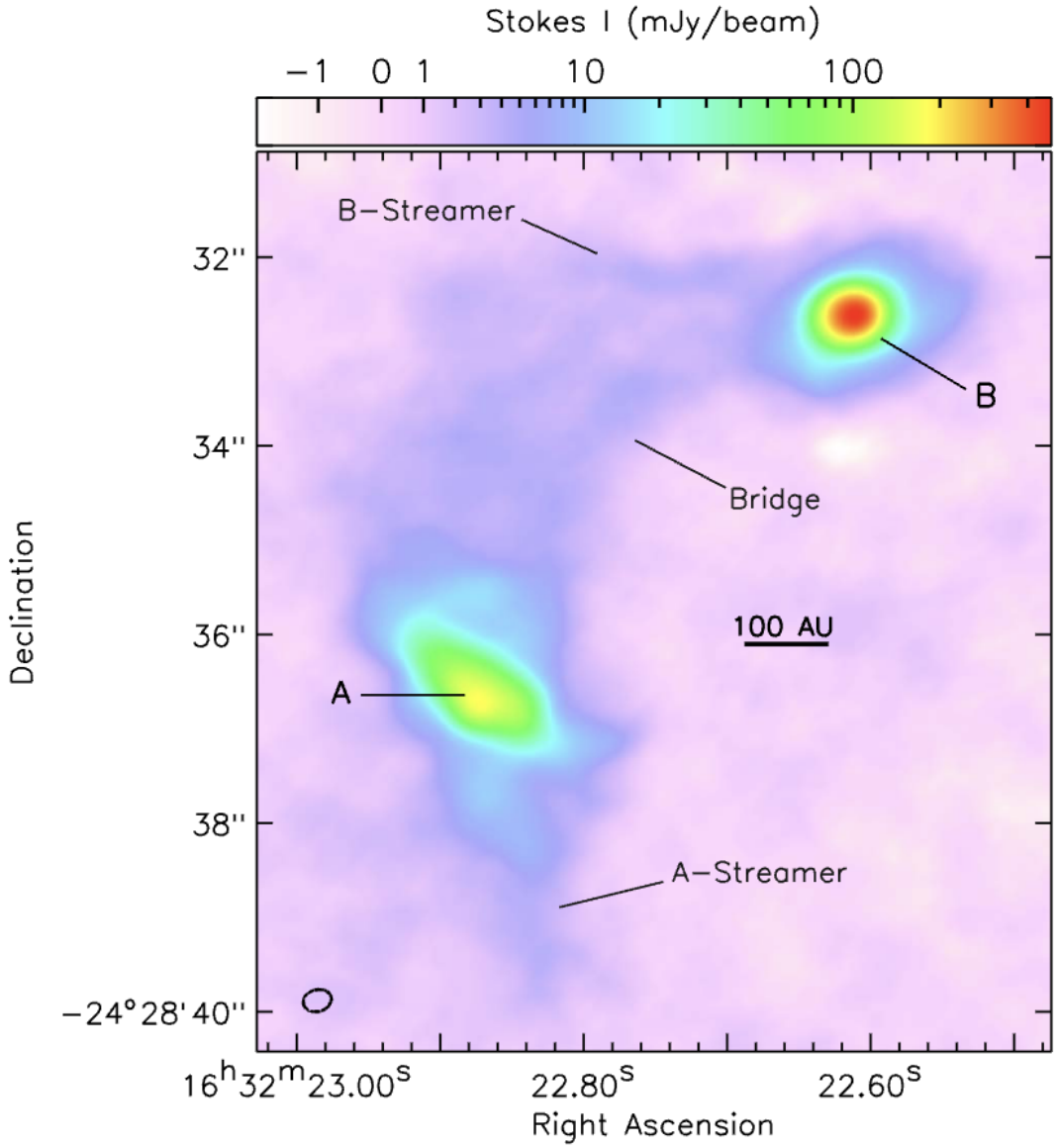

Figure 1.4: ALMA 1.3 mm Stokes I continuum image of the IRAS 16293–2422 system. The two protostellar components, sources A and B, are labeled, together with the Bridge structure and the A- and B-streamers connecting to each source. The synthesized beam is shown in the lower-left corner, and a 100 au scale bar is provided for reference. Credit:Sadavoy et al. (2018), Figure 1.

of several tens of au from the continuum peak, allowing reliable measurements of optically thin molecular emission. At these spatial scales, the chemistry is expected to be primarily regulated by the local temperature and density structure associated with source B, while any influence from source A is likely attenuated. These observations reveal a rich inventory of COMs with sufficient sensitivity to detect

not only isotopologues but, in some cases, distinct ^{13}C isotopomers (Jørgensen et al. 2018). Such data provide rare empirical constraints on position-specific carbon isotope distributions within COMs, which are directly relevant to the questions addressed in this thesis.

Previous observational and modeling studies have provided quantitative constraints on the physical structure of the protostellar envelope surrounding IRAS 16293–2422. Radiative transfer modeling of the dust continuum by Crimier et al. (2010) established a spherically symmetric envelope structure characterized by steep radial gradients in both density and temperature. In this model, the gas density follows a power-law distribution $n_{\rm H}(r) \propto r^{-1.7}$, reaching $n_{\rm H} \gtrsim 10^7$–10^8 cm^{-3} in the inner envelope, while the dust temperature rises rapidly toward the center. The radius at which $T_{\rm dust} \simeq 100$ K, corresponding to the onset of efficient thermal desorption of major ice constituents, is constrained to be ∼90–120 au, depending on the adopted luminosity and envelope parameters. These results provide a quantitative physical framework for interpreting high-angular-resolution molecular observations. The chemical relevance of this physical structure has been further highlighted by time-dependent gas–grain chemical modeling studies. In particular, Wakelam et al. (2014) coupled a collapsing envelope model based on the radiation-hydrodynamical calculations of Masunaga & Inutsuka (2000) to a comprehensive chemical network and showed that molecular abundances and isotopic ratios depend sensitively on the adopted physical structure and collapse history, especially at radii larger than ∼100 au. They demonstrated that modest changes in the envelope density profile can lead to substantial differences in the degree of molecular depletion and in the resulting isotopic compositions, even though the warm inner region ($r \lesssim 100$ au) is largely governed by post-sublimation gas-phase chemistry. This result emphasizes that isotopic signatures observed in the hot corino do not solely reflect local physical conditions, but also encode the chemical history accumulated during earlier, colder stages of envelope evolution. Such sensitivity arises because the Masunaga & Inutsuka collapse model self-consistently links the temporal evolution of density and temperature experienced by fluid parcels, which directly controls the duration of CO freeze-out, ice chemistry, and subsequent sublimation.

Consistent with this physical picture, observational studies have shown that many COMs—including methanol, methyl formate, dimethyl ether, and glycolaldehyde—are concentrated within the inner ≲100 au of the protostellar system. This region is characterized by elevated temperatures ($T \gtrsim 100$ K), at which icy grain mantles have largely sublimated and the gas-phase composition is expected to reflect the cumulative outcome of earlier ice chemistry and subsequent gas-phase processing. Consequently, isotopic measurements in this inner region predominantly

probe the post-sublimation molecular inventory, providing a direct observational counterpart to the chemical abundances predicted by astrochemical models at late evolutionary stages.

At present, observational constraints on the $^{12}C/^{13}C$ ratios of COMs are available for only a very limited number of sources, with IRAS 16293–2422B serving as the primary benchmark. The derived absolute isotope ratios typically carry substantial uncertainties, often at the level of ∼30%, reflecting limitations in sensitivity, calibration, line blending, and fitting procedures. In particular, a significant fraction of this uncertainty arises from degeneracies in single-temperature LTE slab fits, where excitation temperature and column density are not independently constrained. Additional systematic uncertainties may arise from spectroscopic inputs. For some molecules, partition functions in commonly used spectroscopic databases—such as CDMS and JPL—do not fully include vibrationally excited states and were primarily developed for cold (∼10 K) sources. As a result, high-temperature effects relevant to warm protostellar environments may not be completely captured. Although vibrational correction factors are sometimes applied, uncertainties in partition functions and transition intensities can propagate directly into derived column densities and isotopic ratios, particularly for COMs. These spectroscopic limitations have not yet been systematically assessed, and while we adopt the reported ∼30% uncertainties as the best available estimates, future spectroscopic developments may revise these values. Despite these limitations, these measurements represent the most sensitive and comprehensive isotopic datasets currently available for COMs.

IRAS 16293–2422B is not treated as a unique or exceptional object in this work, but rather as a representative benchmark source that enables direct confrontation between isotopomer-resolved astrochemical models and observations. Systematic comparisons between modeled abundances and isotopic compositions and those observed within the inner ∼100 au region provide a sensitive test of the physical and chemical assumptions underlying the models. In particular, such comparisons provide a means to assess whether the relative isotopic patterns implied by the observations can be reproduced by current chemical networks, or instead point to additional processing or missing reaction channels. Accordingly, the aim of this work is not to achieve a definitive quantitative match to absolute $^{12}C/^{13}C$ ratios, but rather to examine whether astrochemical models can reproduce the relative isotopic patterns implied by the observations within the present uncertainties. By explicitly acknowledging these observational limitations, this study establishes a modeling framework that can be directly applied to future datasets with improved sensitivity and broader source coverage, enabling increasingly stringent tests of isotopomer-specific formation pathways as observational capabilities continue to

advance.

In addition to IRAS 16293–2422B, observational efforts to constrain the carbon isotopic composition of COMs are now expanding to a broader range of sources. Recent studies, such as Busch et al. (2025), and forthcoming large systematic programs, including the ALMA Large Program COMPASS, are beginning to provide isotopic measurements for multiple protostellar environments. These programs are expected to significantly enlarge the currently very limited sample of sources with reliable $^{12}C/^{13}C$ constraints, enabling comparative studies of isotopic chemistry across different physical environments and evolutionary stages.

1.6 Reqired Astrochemistry models

Recent advances in observational capabilities—most notably through facilities such as the James Webb Space Telescope (JWST) and the ALMA—have ushered in a new era of astrochemistry. These instruments provide unprecedented sensitivity and spatial resolution, enabling the detection of a wide range of molecules, including COMs and their isotopologues, across various stages of star and planet formation. With these detailed molecular inventories now accessible, a critical gap has emerged: theoretical models must evolve to match the sophistication of observations. To interpret the increasingly rich spectroscopic datasets, it is essential to refine chemical models in the following ways:

- Reaction Pathway Elucidation: The formation routes of COMs and other key species—whether occurring in the gas phase, on dust grain surfaces, or within ice mantles—remain incompletely understood. This is particularly true for isotopic variants, which may follow position-specific or site-selective pathways.

- Time-Dependent Modeling: Chemical abundances are highly sensitive to the temporal evolution of physical conditions. Accurately simulating this requires coupling detailed chemical networks with time-evolving physical models of collapsing cores, protostellar envelopes, and disks.

- Quantitative Comparison with Observations: To extract physical and chemical constraints from observational data, models must move beyond qualitative agreement. This entails quantitative reproduction of observed column densities, isotopomer ratios, and spatial distributions—often requiring position- and isotope-specific tracking of molecular species.

The convergence of high-resolution observational data and the need for mechanistically detailed, time-resolved theoretical models marks a pivotal moment in astrochemistry. Now more than ever, there is a pressing need to construct physically self-consistent and isotopically explicit astrochemical models that can bridge the gap between molecular line data and our understanding of the processes governing chemical complexity in star- and planet-forming environments.

1.7 This thesis

The overarching goal of this thesis is to provide a theoretical understanding of the formation and isotopic evolution of COMs in star-forming regions. This thesis introduces several key advances over previous astrochemical studies. First, this thesis presents the first systematic modeling of the $^{12}C/^{13}C$ ratios of complex organic molecules within a fully time-dependent, three-phase astrochemical framework. Unlike previous studies that mainly focused on simpler species (Furuya et al. 2011; Colzi et al. 2020; Loison et al. 2020), this work follows, for the first time, the bulk isotopic evolution of COMs from the prestellar to protostellar stages in a physically self-consistent manner. Second, it develops, for the first time, an isotopomer-resolved chemical network for COMs, explicitly tracing the positional distribution of ^{13}C within individual molecules and linking these signatures to distinct formation pathways. Together, these advances establish a new framework in which isotopic and isotopomer information can be used as direct diagnostics of the chemical origins of COMs.

Specifically, the study addresses the following key questions: How do COMs acquire their isotopic compositions in the early stages of star and disk formation?

- This includes tracking the evolution of $^{12}C/^{13}C$ ratios across different molecular sites and determining how environmental factors such as temperature, density, and cosmic-ray ionization rate influence isotopic fractionation.
- What are the dominant formation pathways of COMs under interstellar conditions? Special attention is given to non-thermal processes, including grain-surface chemistry, cosmic-ray induced radiolysis, and diffusion-mediated radical reactions, as well as their dependence on physical conditions.
- Can isotopomer-specific information be used to disentangle competing formation mechanisms? For molecules with multiple synthetic routes (e.g., CH_3CHO, CH_3CN, CH_3OH), the position of ^{13}C within the molecule offers clues

to its formation history. This thesis explores how such isotopomer-resolved modeling can serve as a diagnostic tool for chemical pathways.

To tackle these questions, the study employs a three-phase astrochemical modeling approach, including:

- Rate-equation models for global evolutionary trends
- Three-phase gas–surface–mantle chemistry to simulate interactions across ice layers
- Isotopomer-resolved reaction networks for tracking site-specific fractionation

Wherever possible, the theoretical predictions are compared with recent observational data from facilities such as ALMA and JWST, to test the validity of the models and identify observable carbon isotopic signatures.

This dissertation is structured as follows:

- *Chapter 2* investigates the evolution of carbon isotope ratios ($^{12}C/^{13}C$) in complex organic molecules from the prestellar to protostellar phases using a gas-grain chemical model. Motivated by recent ALMA observations that report ^{13}C isotopic compositions in COMs, we examine how different formation pathways—particularly those originating from CO, C, and C^+ reservoirs—affect the resulting isotopic fractionation. We find that COMs formed via CO-derived species tend to be slightly enriched in ^{13}C, while those formed from atomic C or C^+ are depleted due to isotope exchange reactions in the prestellar phase. However, in protostellar environments, where COMs are mainly formed on warm grain surfaces and in the hot gas, our base model predicts a degree of carbon isotope fractionation that is larger than observed. To address this, we incorporate grain-surface reactions involving atomic C and CO/H_2O ices, based on recent laboratory evidence. These C-atom addition reactions introduce new formation pathways that reduce the degree of isotopic fractionation, bringing the modeled values into better agreement with observations. The role of cosmic-ray ionization rates in modulating the isotopic ratios is also explored. This chapter thus presents the first study to follow the evolution of carbon isotope fractionation in COMs within a three-phase gas–grain framework coupled to time-dependent physical evolution, while explicitly distinguishing formation pathways associated with different carbon reservoirs.

- *Chapter 3* introduces a new astrochemical model that explicitly tracks the position of ^{13}C within complex organic molecules—i.e., isotopomers building upon the findings in Chapter 2. This isotopomer-resolved network enables a more detailed investigation of how carbon isotope fractionation manifests at the functional-group level within COMs. Motivated by recent JWST detections of COMs in ices, we consider both thermal and non-thermal processes: radical-radical reactions on ice surfaces driven by thermal diffusion, and radiolysis chemistry in the bulk ice induced by cosmic rays. Our results reveal that isotopomer-specific $^{12}C/^{13}C$ ratios depend on both the molecule and its formation environment. For example, molecules containing methyl groups exhibit distinct isotopic signatures depending on whether the carbon originated from CO ice, atomic C, or CH_3 radicals. These signatures serve as chemical fingerprints that can be used to trace COMs formation pathways. The findings highlight the diagnostic power of isotopomer-resolved models and lay the groundwork for future comparisons with high-precision isotopic observations of star-forming regions. This constitutes the first isotopomer-resolved astrochemical modeling of COMs, demonstrating that positional ^{13}C information can be used as a diagnostic tool to identify dominant chemical formation pathways. Furthermore, these astrochemical results are put into a broader context by discussing their implications for Solar System materials, particularly meteoritic organic matter. Recent compound- and position-specific carbon isotope analyses of meteoritic amino acids reveal pronounced intramolecular ^{13}C heterogeneity. By focusing on relative isotope contrasts rather than absolute ratios, the discussion evaluates whether such position-specific signatures may reflect inheritance from distinct interstellar precursor reservoirs, thereby providing a conceptual bridge between interstellar isotopic chemistry and meteoritic organic inventories.

- *Chapter 4* summarizes the main conclusions of this thesis and discusses future perspectives. It synthesizes how isotopomer-resolved astrochemical modeling provides a physically grounded framework to interpret isotopic signatures from prestellar cores to protostars and potentially to Solar System materials. The chapter outlines key directions for future work, including tighter integration with ALMA and JWST observations, reduction of chemical and kinetic uncertainties through laboratory and quantum-chemical studies, incorporation of disk transport and layering into isotopic modeling, and extension of the present ^{13}C-focused framework to multi-isotope systems such as ^{15}N and D/H. These developments will be essential for establishing quantitative links between interstellar chemistry, protoplanetary disk evolution, and the isotopic properties of meteorites and comets.

Chapter 2

Carbon Isotope Fractionation of Complex Organic Molecules in Star-Forming Cores

This thesis chapter originally appeared in the literature as
Ichimura, R., Nomura, H., and Furuya, K. 2024, *ApJ, 970, 55*

2.1 Introduction

In this chapter, we report gas-grain chemical reaction network calculations, systematically investigating the carbon isotopic fractionations of COMs. This calculation includes their formation before star formation and their sublimation into the gas phase following star formation. In Section 2.2, we describe a physical model of a star-forming core and the gas-grain chemical model. In Section 2.3, we present the results of time variation of molecular abundances and $^{12}C/^{13}C$ ratios in the base model. The effects of the atomic C insertion or addition reactions on the grain surface and difference in binding energy between ^{12}CO and ^{13}CO, and the initial condition of carbon and $^{12}C/^{13}C$ ratio of C^+ are also studied. In Section 2.4, we compare our calculation results with the observations in the IRAS 16293-2422B. We also discuss the effect of cosmic ray (CR) ionization rates on $^{12}C/^{13}C$ ratios of COMs. Our findings are summarized in Section 2.5.

2.2 Model

2.2.1 Physical model

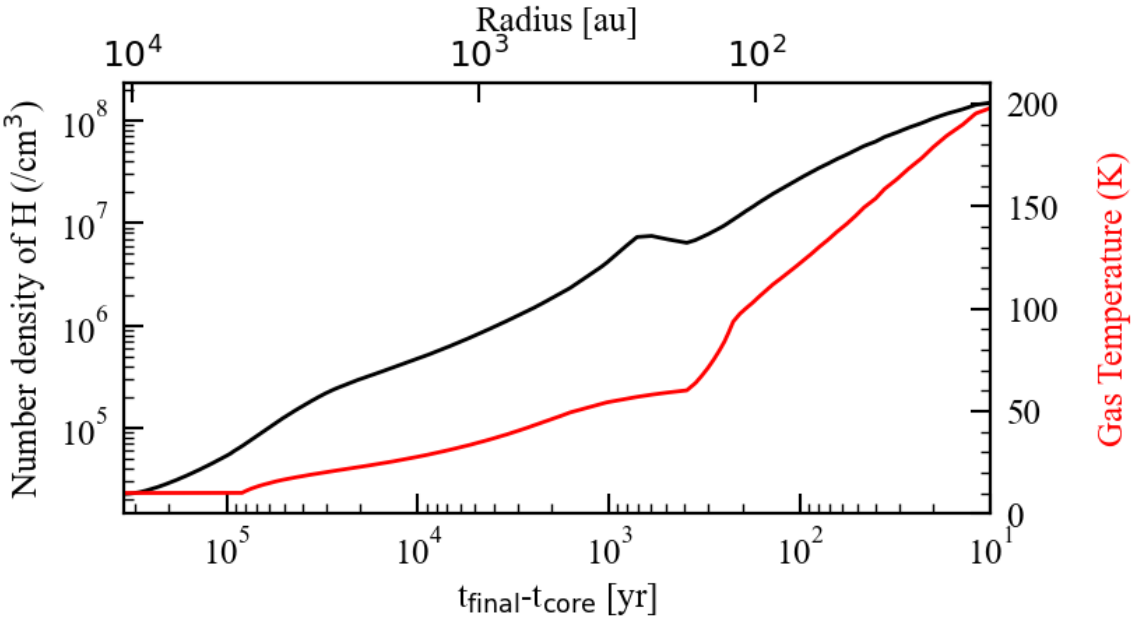

Figure 2.1: Temporal variation of the number density of hydrogen nuclei (black line) and gas temperature (red line) of a fluid parcel along a streamline in a gravitationally collapsing core. The upper axis indicates the radial position of the parcel from the core center.

As a physical model, we adopt the 1D radiation hydrodynamics simulation by Masunaga & Inutsuka (2000). This model traces the evolution of a dense, starless core to a protostellar core. Fluid parcels are traced in the hydrodynamics simulation, and we calculate the evolution of molecular abundances with a chemical reaction network along the fluid parcels as done in Aikawa et al. (2008, 2020). For the purpose of the chemical calculations, we distinguish two stages: an initial static phase, during which physical conditions are held fixed to establish chemical initial conditions, and a subsequent collapse phase, in which the time-dependent physical structure derived from Masunaga & Inutsuka (2000) is applied. In the static phase, the prestellar core is in hydrostatic equilibrium with a constant temperature and density for 1×10^6 yr assuming that turbulence prevents the contraction of the core. In the subsequent collapse phase, a protostar is formed due to gravitational collapse and further grows through envelope accretion. After the collapse starts, the protostar is born at 2.5×10^5 yr. This model further proceeds to track the physical

evolution for 9.3×10^4 yr. Figure 2.1 shows the temporal variation of the number density of hydrogen nuclei and gas temperature in a fluid parcel. We define the moment of the protostar formation as $t_{core} = 0$ and the end of calculation as $t_{core} = t_{final} = 9.3\times10^4$ yr. To increase the visibility of the evolution around the final stage, we adjust the horizontal axis to the logarithmic scale of t_{final} - t_{core} (Aikawa et al. 2008). In the static phase, the fluid parcel is at 1×10^4 au from the core center. The gas and dust temperatures are 10 K, and the number density of hydrogen nuclei is 2.28×10^4 cm^{-3}. At $t_{core} = t_{final}$ the fluid parcel reaches R = 30.6 au, with both gas and dust temperatures reaching at $\sim$ 198 K, and the total H_2 density reaching $\sim$ 1.49×10^8 cm^{-3}. The infalling timescale inside 1000 au is shorter than the lifetime of the protostar in this model so that we can use the time evolution of abundances in a single fluid parcel to represent the true radial distribution (Aikawa et al. 2020). For the sake of simplicity, we impose a minimum temperature of 10 K throughout our simulations. In the original collapse calculation of Masunaga & Inutsuka (2000), attenuation of the external radiation field can lead to a slightly lower temperature in the deep interior than near the cloud edge, and the temperature of a fluid parcel may briefly fall below 10 K in the early collapse stage. Because we introduce a static phase with a fixed temperature prior to collapse (cf. Aikawa et al. 2008), directly connecting to the original temperature evolution can produce a small, artificial discontinuity at the transition. The adopted temperature floor is therefore used to maintain a smooth and consistent thermal history across the static-to-collapse connection. We note that this choice primarily affects only the coldest part of the early collapse phase and does not qualitatively alter the chemical trends discussed in this thesis.

2.2.2 Chemical model

The base model

We utilize the gas-ice astrochemical code "Rokko" (Furuya et al. (2015)). The code solves the rate equations (see Equation 1.1) for a given list of chemical reactions. We expand this reaction network to include mono-^{13}C species and carbon isotope exchange reactions. The chemistry is described by a three-phase model (Furuya et al. 2016). This model makes a distinction between the surface of the ice mantle and the rest of the ice mantle (Hasegawa & Herbst 1993). Like in Hasegawa & Herbst (1993), we assume that the ice mantle phase remains chemically inert, while the ice surface phase considers chemical reactions. In this network, carbon isotopes are limited to carbon skeleton up to C_2H_X for simplicity. ^{13}C isotopomers (e.g., $^{12}C^{13}CH$ and $^{13}C^{12}CH$) are not distinguished. We have omitted the multiple fractionations, such

as two or more ^{13}C for simplicity. Isotope exchange reactions are taken from Roueff et al. (2015) and Loison et al. (2020). Moreover, we incorporate two hydrogenation reactions on grain surface; CH_2CO ice + H ice → CH_3CO ice and CH_3CO ice + H ice → CH_3CHO ice (Ruaud et al. 2015). We neglect ^{13}C fractionation via the isotope selective photodissociation in the following sections because we only consider the dense region. Our reaction network consists of 733 gas and grain species and 20360 gas phase and grain surface reactions.

We assume the Langmuir-Hinshelwood mechanism to describe two-body reactions on grain surfaces. In this mechanism, species on the grain surface diffuse by thermal hopping and react with each other when they meet. The set of adsorption energies is adopted from Furuya et al. (2015). The barrier for thermal diffusion of atoms and molecules, excluding hydrogen (H), is set to be 40 % of the adsorption energy (E_{des}). The barrier is set at 30 % of E_{des} for hydrogen. We assume that the sticking probability of colliding gaseous species except for hydrogen onto the grain is unity. For hydrogen, the sticking probability is calculated based on Hollenbach & McKee (1979). We adopt the low-metal elemental abundances listed in Table 2.1 taken from Aikawa et al. (2001). The species are assumed to be initially atoms or atomic ions, except for hydrogen, which is in H_2. The dust grain is spherical with a 0.1 μm radius with the material density of 2.5 g/cm^3. The dust-to-gas ratio is set to 0.01. The CR ionization rate of H_2 is set to be 1.3×10^{-17} s^{-1} (Terzieva & Herbst 1998). In this thesis, we define "abundance" as the fractional abundance of species to hydrogen nuclei.

The direct C-atom addition reactions

Besides the Langmuir-Hinshelwood process, complex molecules could be formed via the direct collision of a gaseous species with adsorbed species on a grain surface via the so-called Eley-Rideal (ER) mechanism. We incorporate the ER reactions involving atomic C referring to recent laboratory studies (hereafter direct C-atom addition reaction) (Molpeceres et al. 2021; Potapov et al. 2021; Fedoseev et al. 2022). We incorporate the following two direct C-atom addition reactions into the model presented in Section 2.3.2.

$$\mathrm{C} + \mathrm{H_2O\,ice} \rightarrow \mathrm{H_2CO\,ice}. \tag{2.1}$$

$$\mathrm{C} + \mathrm{CO\,ice} \rightarrow \mathrm{C_2O\,ice}. \tag{2.2}$$

Table 2.1:: Initial abundances with respect to hydrogen nuclei.

Species	Abundance ($n_i/n_{\rm H}$)
H_2	5.00×10^{-1}
He	9.75×10^{-2}
$^{12}C^+$	7.86×10^{-5}
$^{13}C^+$	1.14×10^{-6}
N	2.47×10^{-5}
O	1.80×10^{-4}
Si^+	9.74×10^{-9}
S^+	9.14×10^{-8}
Fe^+	2.74×10^{-9}
Na^+	2.25×10^{-8}
Mg^+	1.09×10^{-8}
Cl^+	2.16×10^{-10}
P^+	1.00×10^{-9}

These direct C-atom addition reactions are assumed to occur when atomic C is adsorbed from the gas phase onto its reaction partner on the grain surface. Therefore, the reaction coefficient (s^{-1}) of the direct C-atom addition reaction is given by

$$k_{Cadd} = A \times k_{acc} \times \frac{n_s(X)}{n_s(total)}, \tag{2.3}$$

where k_{acc} is the accretion rate, which is given by the collisional frequency of a gas phase species (here, atomic C) with a grain multiplied by sticking probability, $n_s(X)$ is the number density of species X on grains, $n_s(total)$ is the number density of total species adsorbed on the grain surface, and A is a branching ratio. Some gaseous atomic C take part in this direct C-atom addition reaction instead of the adsorption, so the adsorption rate of atomic C is adjusted by subtracting the reaction coefficient of the direct C-atom addition reaction as

$$k_{acc,adj} = k_{acc} - k_{Cadd}, \tag{2.4}$$

where $k_{acc,adj}$ is the adjusted accretion rate. Some adsorbed atomic C transfer a part of their kinetic energy to the grain surface and then stick in physisorbed sites. Others can transfer to chemisorbed sites or desorb from surface (Tsuge et al. 2023). So, the branching ratio of the reaction in Eq.(2.1) is set to be 0.3 ($A = 0.3$) based on recent laboratory experiments (Molpeceres et al. 2021; Tsuge et al. 2023). For the reaction in Eq.(2.2), the branching ratio is set to be 1 ($A = 1.0$) because this reaction is suggested to be barrierless (Fedoseev et al. 2022). The impact of direct C-atom addition reactions on the $^{12}C/^{13}C$ ratios of COMs are discussed in Sect. 2.3.2.

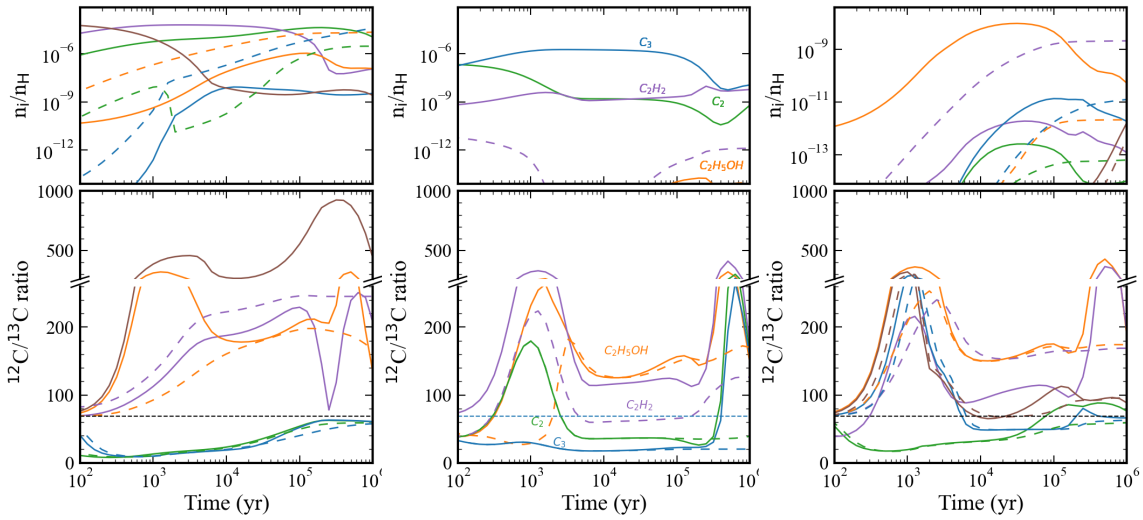

Figure 2.2: Temporal variation of the molecular abundances and $^{12}C/^{13}C$ ratios for gaseous species (solid lines) and icy species (dashed lines) during the static phase in the base model. The horizontal black dashed line represents the average $^{12}C/^{13}C$ ratio of local ISM. A broken y-axis is used in the lower panel to show both the moderate ratios of some species (e.g., CO and CH_3OH) and the very high ratios of other species (e.g., C^+ and CH_4).

2.3 Results

2.3.1 The Base Model

The Static Phase

Figure 2.2 presents the temporal evolution of the abundances and $^{12}C/^{13}C$ ratios of selected species during the static phase, in which the physical conditions are held fixed. The adopted parameters are a temperature of 10 K, a gas density of 2.28×10^4 cm^{-3}, a cosmic-ray ionization rate of 1.3×10^{-17} s^{-1}, and a visual extinction of 4.5 mag. The dominant carriers of carbon in the gas phase change over time. Initially, carbon in the gas phase is dominated by C^+, which is gradually converted into atomic C and subsequently into CO as chemical evolution proceeds. At a density characteristic of the static phase, these small carbon-bearing species accrete onto dust grains and participate in surface chemistry. Adsorbed atomic C is rapidly hydrogenated to form CH_4 ice, while adsorbed CO is converted into CH_3OH ice through successive hydrogenation reactions on grain surfaces before $\sim 10^5$ yr. During the static phase, significant ^{13}C fractionation is established through

exothermic isotope exchange reactions (Furuya et al. 2011; Colzi et al. 2020; Loison et al. 2020). $^{13}C^+ + {}^{12}CO \rightleftharpoons {}^{12}C^+ + {}^{13}CO + 35$ K and $^{13}C + C_3 \rightleftharpoons {}^{12}C + {}^{13}CC_2 + 28$ K. These reactions preferentially transfer ^{13}C from C^+ and atomic C into CO and C_3, leading to ^{13}C depletion in the atomic and ionized carbon reservoirs and enrichment in CO and small carbon chains. The temporal evolution of the $^{12}C/^{13}C$ ratios is therefore closely tied to changes in the dominant source of gaseous atomic carbon. At At early times ($t \sim 10^3$ yr), atomic C is mainly supplied by C^+, resulting in ^{13}C-poor C and C^+. Consequently, species such as C_2, which form primarily from atomic C or C^+ during this phase, exhibit ^{13}C depletion. As the chemistry evolves toward $t \sim 2 \times 10^5$ yr, CO becomes the dominant carrier of gas-phase carbon. Because CO is enriched in ^{13}C by isotope exchange reactions, the supply of atomic C increasingly originates from ^{13}C-rich C_3 and CO-related pathways. This transition causes a temporary decrease in the $^{12}C/^{13}C$ ratio of atomic C toward the elemental ISM value, producing a second characteristic feature in the temporal evolution of isotopic ratios. At later times ($t \gtrsim 10^6$ yr), C^+ is primarily regenerated through the destruction of CO by reactions with He^+. Subsequent isotope exchange reactions again drive C^+, atomic C, and C_3 toward ^{13}C-poor compositions. As a result, species whose formation pathways depend on these reservoirs exhibit renewed ^{13}C depletion, while the $^{12}C/^{13}C$ ratio of CO gradually relaxes toward the local ISM value (Furuya et al. 2011).

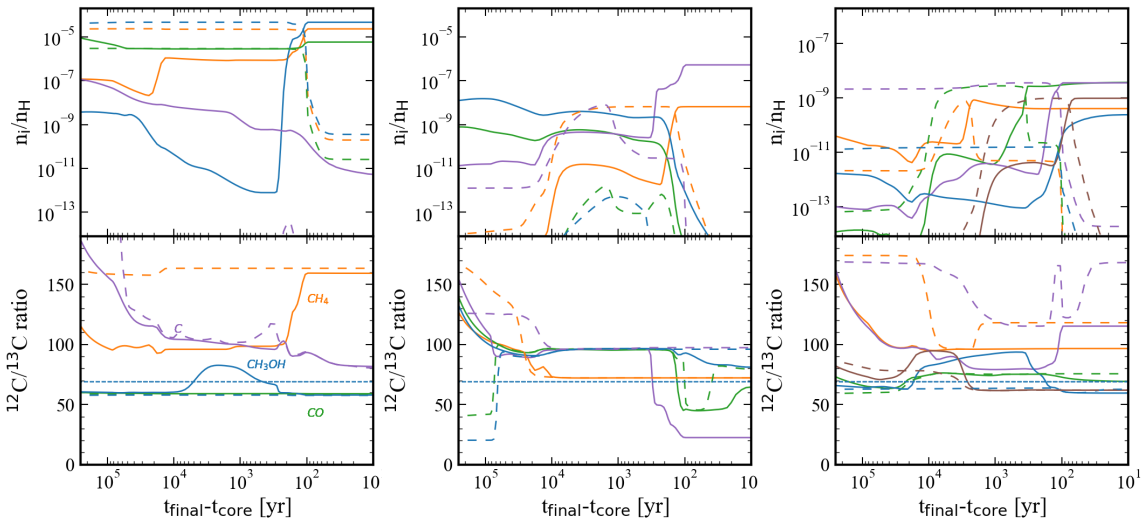

Figure 2.3: Same as Figure 2.2 but during the collapse phase.

The carbon isotope ratios of icy molecules record the isotopic composition of their precursor species at the time of ice formation. Before 10^5 yr, icy molecules such as CH_4 and CH_3OH are mainly formed from atomic C and CO accreted onto

grain surfaces. As a result, the $^{12}C/^{13}C$ ratios of these ices directly reflect those of atomic C or CO in the gas phase at early times. After $\sim 10^5$ yr, CO becomes the dominant carbon reservoir in the gas phase. Consequently, the carbon isotope ratio of CH_3OH ice gradually approaches the local ISM value, following the temporal evolution of CO. In contrast, the formation of CH_4 ice becomes inefficient after $\sim 10^5$ yr, and the existing CH_4 ice retains the high $^{12}C/^{13}C$ ratio established during the earlier phase. As a result, the dominant icy carbon-bearing molecules exhibit a bimodal distribution in their $^{12}C/^{13}C$ ratios: either significantly depleted in ^{13}C or comparable to, or slightly enriched in ^{13}C (by $\sim$10%), relative to the local ISM value.

COMs are formed from simple molecules. Before around 10^5 yr when C^+ and atomic C are the main carbon reservoir, COMs (e.g. CH_3CHO) and their ices are mainly formed from ^{13}C-poor molecules, while after around 10^5 yr when CO is main carbon reservoir, COMs (e.g. CH_3OCH_3) and their ice are formed from slightly ^{13}C-rich CO or CH_3OH on the grain surface or adsorbed on grains after the formation in the gas phase. The $^{12}C/^{13}C$ ratios of COMs follow those of simple molecules and exhibit a bimodal profile. Some molecules including COMs (e.g. NH_2CHO and HCOOH) are formed from both fractionated CH_4 and CO. For example, NH_2CHO is formed from H_2CO. H_2CO is formed from CO ice on the grain surface and CH_3 in the gas phase, so the $^{12}C/^{13}C$ ratios of these molecules including COMs show the intermediate value between the bimodal profile.

The Collapse Phase

In the collapse phase (see Fig.2.1), icy molecules on the grain surface sublimate into the gas phase at their sublimation temperatures, which depend on their binding energies, and the rest in the bulk ice mantle are trapped in water ice and sublimate at $\sim$ 120 K together with water ice. Moreover, some species are additionally produced by grain surface reactions. Figure 2.3 shows the temporal variation of abundances and $^{12}C/^{13}C$ ratios of selected species in the collapse phase. For CH_4, the binding energy is set to be 1300 K, CH_4 ice on the surface sublimates around 20 K (t_{final} - $t_{core} \sim 2 \times 10^4$ yr) and the gas phase CH_4 abundance increases to almost 1×10^{-6}. After that, whole CH_4 ice sublimates at $\sim$ 120 K (t_{final} - $t_{core} \sim 10^2$ yr) together with water ice. The $^{12}C/^{13}C$ ratios of abundant molecules (molecular abundance of $\sim 10^{-5}$) molecules such as CH_4 and CH_3OH after water ice sublimation (t_{final} - $t_{core} \sim 10^2$ yr) reflect those of ice formed during the static phase. After CH_4 ice sublimates at $\sim$ 120 K, the $^{12}C/^{13}C$ ratio of gaseous CH_4 becomes significantly depleted in ^{13}C as well as that of CH_4 ice.

On the other hand, some icy COMs (e.g. CH_3CHO and NH_2CHO) are produced via radical-radical reactions on the grain surface during the collapse phase. The abundances of the additionally formed ices are equivalent to or exceeding the abundances of the icy COMs formed during the static phase. Therefore, the $^{12}C/^{13}C$ ratios of some sublimated COMs (e.g. CH_3CHO and NH_2CHO) are different from those of their ice formed in the static phase. The $^{12}C/^{13}C$ ratios of icy molecules formed during the collapse phase depend on the $^{12}C/^{13}C$ ratios of reactants such as radicals. For example, the NH_2CHO ice is formed from ^{13}C-enriched HCO radical ($^{12}C/^{13}C \sim 30$) during the collapse phase, so the $^{12}C/^{13}C$ ratio of NH_2CHO ice decreases, and eventually the $^{12}C/^{13}C$ ratio of sublimated NH_2CHO is different from that of ice formed in the static phase. Consequently, the $^{12}C/^{13}C$ ratios of some COMs after water ice sublimation are essentially a mixture of those formed during the static phase and the collapse phase, sometimes closer to the $^{12}C/^{13}C$ ratios of icy COMs formed during the collapse phase rather than those in the static phase. Moreover, the formation of a part of COMs proceeds even in the gas phase via ion-neutral reactions after the sublimation, resulting in distinct carbon isotope ratios compared to those in ice before sublimation. The detailed explanation for other complex molecules is presented in Section 2.4.1.

2.3.2 The effect of the direct C-atom addition reactions

Based on recent laboratory experiments and quantum chemical calculations, we incorporate the two direct C-atom addition reactions by the ER mechanism; Eq.(2.1) (Molpeceres et al. 2021; Potapov et al. 2021) and Eq.(2.2) (Fedoseev et al. 2022). Figure 2.4 shows the temporal variation of abundances and $^{12}C/^{13}C$ ratios of some icy species in the static phase without and with the direct C-atom addition reactions. In the model with the direct C-atom addition reactions, the abundances of icy CH_3OH and CH_3CHO increase compared to the base model. On the other hand, the abundance of CH_4 ice, which is mainly formed via hydrogenation reactions of atomic C on the grain surfaces, slightly decreases compared to the base model (by ~ 15 %). The $^{12}C/^{13}C$ ratios of icy CH_3OH and CH_3CHO in the model with the direct C-atom addition reactions are less fractionated than those in the base model. Figure 2.5 shows formation pathways of CH_3OH and CH_3CHO in the models with the direct C-atom addition reactions which suggests that due to these reactions, the isotope fractionation of some species could be suppressed. CH_3OH ice is formed via hydrogenation reactions of ^{13}C-enriched CO ice on the grain surfaces in the base model. In contrast, in the direct C-atom addition model CH_3OH ice is additionally formed from slightly ^{13}C-depleted atomic C via the reaction in

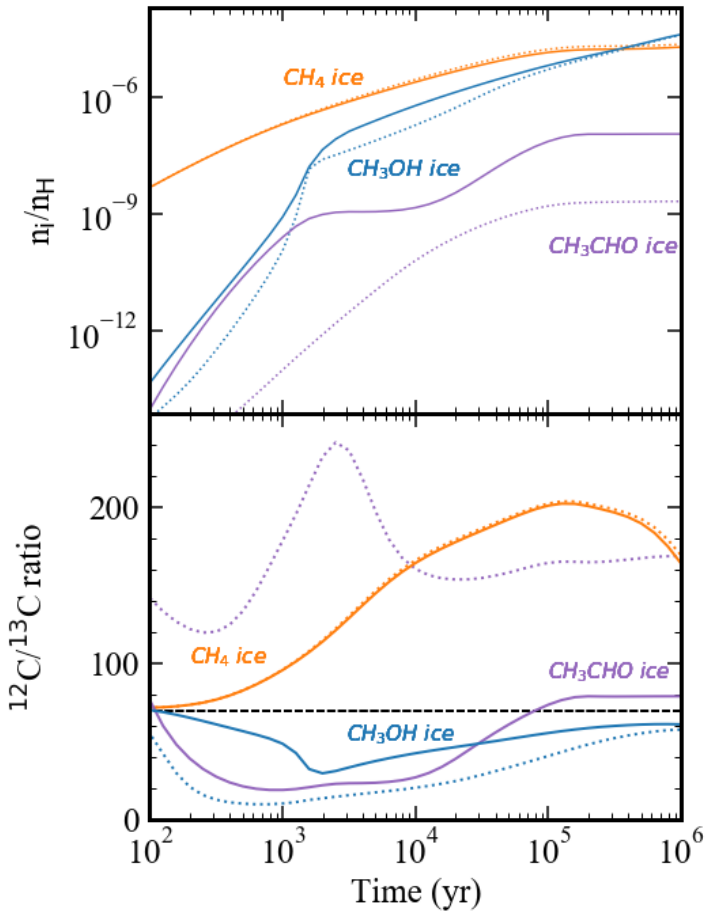

Figure 2.4: Temporal variation of the molecular abundances and $^{12}C/^{13}C$ ratios of CH_4 ice, CH_3OH ice, and CH_3CHO ice during the static phase for the base model (dotted lines) and the model with the direct C-atom addition reactions (solid lines).

Eq.(2.1) and the subsequent hydrogenation reactions on the grain surfaces. In the base model, CH_3CHO ice is ultimately formed from ^{13}C-depleted C^+ and atomic C through a combination of gas-phase and grain-surface processes. In the gas phase, the key precursor CH_2CO is produced primarily via reactions between O atoms and C_2H_3 radicals, where the carbon backbone inherits the ^{13}C-depleted signature originating from C^+ and atomic C. Subsequent adsorption of CH_2CO onto grain surfaces followed by hydrogenation reactions leads to the formation of CH_3CHO ice. In contrast, in the model with the direct C-atom addition reactions CH_3CHO ice is additionally formed from slightly ^{13}C-depleted atomic C and ^{13}C-enriched CO via the reaction in Eq.(2.2) followed by a sequence of hydrogenation reactions on the grain surfaces. These formation processes make differences in carbon isotope fractionation of CH_3OH and CH_3CHO between the models with and without the direct C-atom addition reactions.

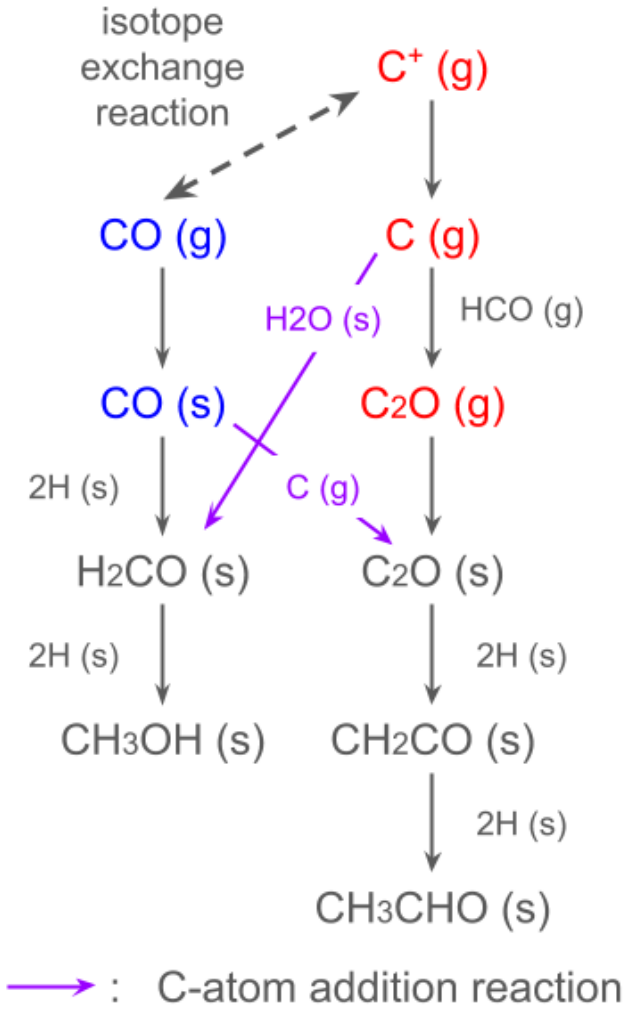

Figure 2.5: Schematic formation pathways of CH_3OH and CH_3CHO with the direct C-atom addition reaction. Gas phase species (g) link to the icy species on the grain surface (s). The dashed arrow indicates the isotope exchange reaction. Red-colored species are depleted in ^{13}C, while blue-colored species are enriched in ^{13}C. Purple arrows indicate the direct C-atom addition reaction. Species 2H indicate consecutive hydrogenation reactions on the grain surfaces.

Figure 2.6 shows the temporal variation of abundances and $^{12}C/^{13}C$ ratios of selected species in the collapse phase with the direct C-atom addition reactions. Some icy complex molecules related to the direct C-atom addition reactions (e.g. CH_3CHO) show less fractionation rather than those in the base model. After water ice sublimation, molecules that are formed via the direct C-atom addition reactions and following reactions, also show a smaller degree of carbon isotope fractionation compared to those in the base model.

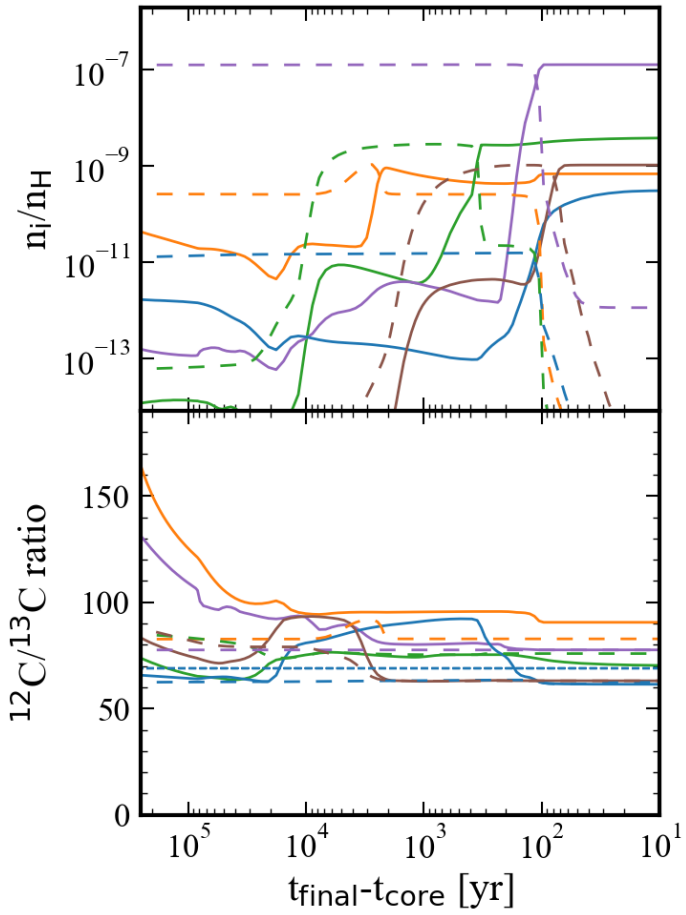

Figure 2.6: Same as right panel of Figure 2.3 but with the direct C-atom addition reactions.

2.3.3 The effect of the difference in Binding Energy between ^{12}CO and ^{13}CO

If the binding energies of CO isotopologues on the dust surface are mass-dependant and thus ^{13}CO is larger than that of ^{12}CO, ^{12}CO can sublimate at a lower temperature than ^{13}CO. Consequently, CO in the gas phase would become depleted in ^{13}C, while CO ice would become enriched in ^{13}C. Smith et al. (2015) theoretically investigated the mass-dependence of thermal desorption of CO and dust temperature for segregation between ^{12}CO and ^{13}CO in the ices. They considered the balance between the adsorption rates and desorption rates for $^{12}C^{16}O$ and $^{13}C^{16}O$. As a result, assuming a 10 K difference in binding energy, the $^{12}CO/^{13}CO$ gas ratio reaches twice as high as the elemental $^{12}C/^{13}C$ ratio. Moreover, Smith et al. (2021) derived binding energies of pure ^{12}CO ice and pure ^{13}CO ice to be 833 $\pm$ 5 K,

and 846 ± 6 K respectively based on laboratory experiments. We additionally run models assuming that the binding energy of ^{12}CO is 833 K and that of ^{13}CO is 846 K for both the static phase and the collapse phase. We find that the difference in binding energy does not affect the ^{12}C/^{13}C ratios of COMs although the difference leads to the desorption rate of CO to be slightly increased, nearly 10 %.

2.3.4 Dependence on the Elemental ^{12}C/^{13}C Ratio

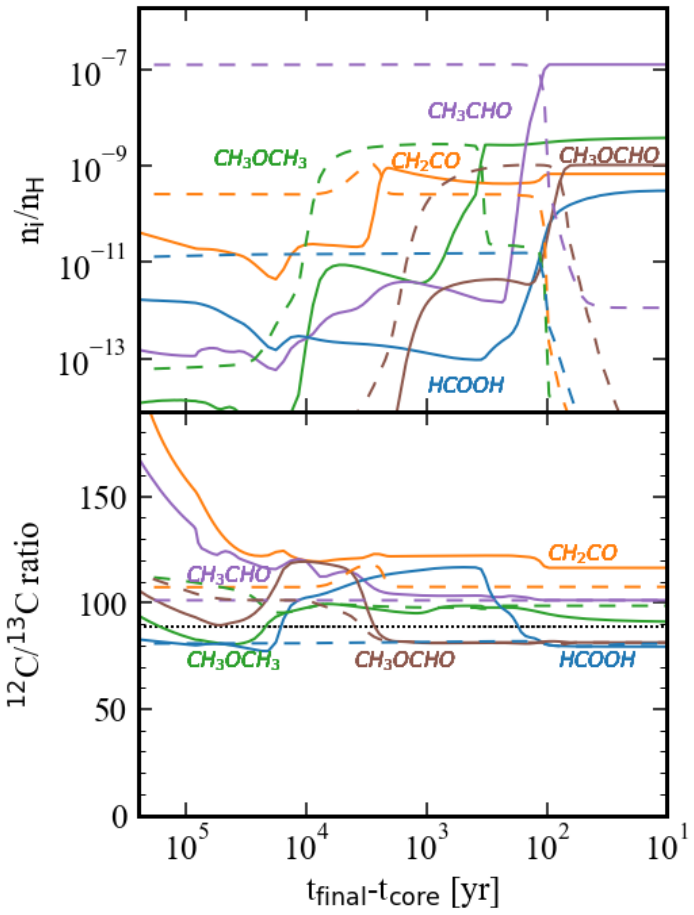

Figure 2.7: Same as right panel of Figure 2.3 but adopting the direct C-atom addition reactions and initial ^{12}C/^{13}C = 89. The horizontal black dotted line in the lower panel represents the average ^{12}C/^{13}C ratio of the Solar System.

In our models presented in the previous section, we assume the elemental ^{12}C/^{13}C ratio is 68, which corresponds to the local ISM value (Milam et al. 2005b). Here, we explore how our results depend on the assumed value of the elemental ^{12}C/^{13}C ratio. Figure 2.7 shows the temporal variation in the collapse phase with the elemental

$^{12}C/^{13}C$ ratio = 89, which is the average value in the Solar System. We find that the $^{12}C/^{13}C$ ratios of molecules are approximately scaled with the assumed elemental $^{12}C/^{13}C$ ratio.

2.3.5 Dependence on the Initial Form of Carbon

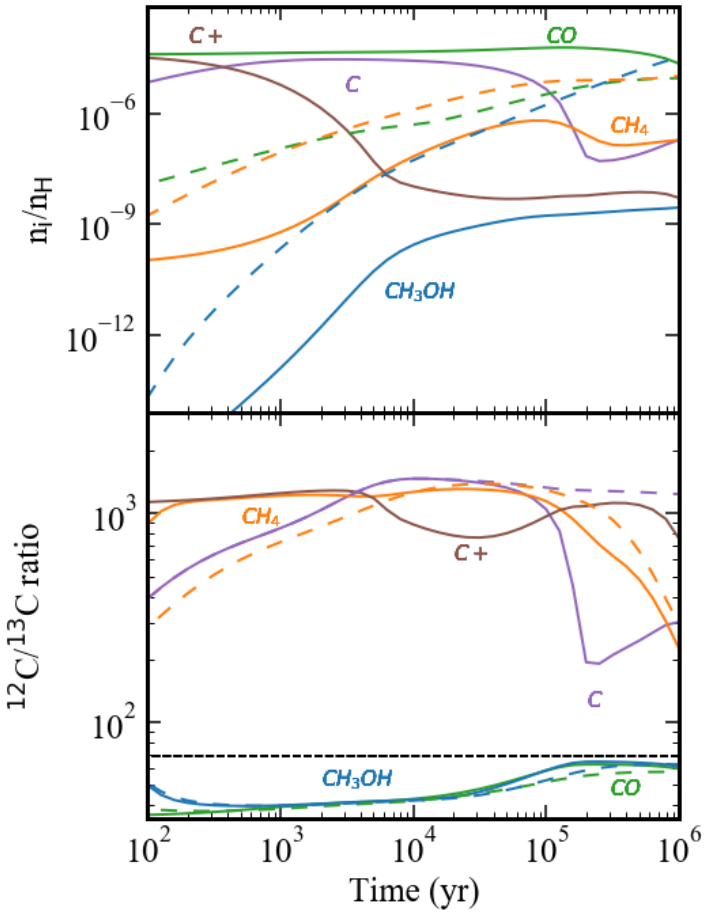

Figure 2.8: Same as left panel of Figure 2.2 but with the initial condition in which half of the carbon is in the form of CO, while the remaining half is in the form of C^+

So far, we assumed that carbon is initially present as $^{12}C^+$ and $^{13}C^+$. Here, we investigate the dependence of the initial form of carbon on the carbon isotope ratios of molecules. In addition to the base model, we calculate a model in which half of the carbon is initially present as ^{12}CO and ^{13}CO ($^{12}CO/^{13}CO = 68$), while the remaining half is present as $^{12}C^+$ and $^{13}C^+$ ($^{12}C^+/^{13}C^+ = 68$). In the following, we refer to this model as the half-CO model. We run models both with and without the direct C-atom addition reactions during the static and collapse phases. The dependence of

selected molecules on the initial form of carbon is summarized in Table 2.2.

Figure 2.8 shows the temporal variation of abundances and $^{12}C/^{13}C$ ratios of selected species in the static phase without the direct C-atom addition reactions. The dependence on the initial carbon form is first seen in simple molecules. Molecules formed from CO show only a weak dependence on the initial carbon form. Although CO is initially more abundant in the half-CO model than in the base model, almost all carbon is eventually converted into CO by 10^6 yr in the static phase (see the left panel of Fig. 2.2). As a result, the abundances and $^{12}C/^{13}C$ ratios of CO-derived species are similar between the two models. For example, around 10^6 yr in the static phase, the abundance of CH_3OH ice is 3.0×10^{-5} and the $^{12}C/^{13}C$ ratio is 61 in the half-CO model, similar to the base model values of 3.7×10^{-5} and 60. In contrast, molecules formed from atomic carbon show a stronger dependence on the initial carbon form. At early times in the static phase, the abundance of C^+ is lower in the half-CO model than in the base model because half of the elemental carbon is initially locked in CO. As a result, the abundances of C^+-derived molecules such as CH_4 are initially smaller than in the base model. For example, around 10^5 yr in the static phase, the abundance of CH_4 is 6.22×10^{-7}, that is about 2 times smaller compared to those in the base model, in which the abundance is 1.1×10^{-6}. As the static phase proceeds, however, C^+ is gradually regenerated through cosmic-ray-driven destruction of CO. On timescales approaching 10^6 yr, the abundance of C^+ becomes comparable between the two models, and the difference in molecular abundances correspondingly decreases. In contrast to the abundances, the carbon isotope ratios retain a strong dependence on the initial carbon form. Because CO is present from the beginning in the half-CO model, the carbon isotope fractionation is initially stronger than in the base model. As a result, the $^{12}C/^{13}C$ ratio of CH_4 increases from 133 in the base model to about 225 in the half-CO model at $t \sim 10^6$ yr. As the evolution proceeds and carbon becomes increasingly locked in CO, the degree of fractionation gradually decreases, similarly to the behavior in the base model.

The behavior of complex molecules can be understood in terms of the relative contributions of CO-derived and C-derived precursors. The dependence on the initial carbon form can be understood by first considering the models without the direct C-atom addition reactions. As discussed above, complex molecules formed mainly from CO-derived species in the static phase show little dependence on the initial carbon form, similarly to CO and CH_3OH. In contrast, molecules formed from atomic carbon inherit the ^{13}C depletion characteristic of the C^+ reservoir. For example, the $^{12}C/^{13}C$ ratio of CH_3CHO ice formed in the static phase increases from 207 in the base model to 337 in the half-CO model. During the collapse

phase, however, CH_3CHO ice is formed from a mixture of ^{13}C-rich and ^{13}C-poor precursors, and therefore the influence of the initial carbon form becomes smaller. After sublimation, the $^{12}C/^{13}C$ ratio of CH_3CHO is 115 in the base model and 127 in the half-CO model. A similar reduction of the dependence on the initial carbon form is found when the direct C-atom addition reactions are included. In this case, mixing of ^{13}C-rich and ^{13}C-poor carbon reservoirs already occurs in the static phase. As a result, the $^{12}C/^{13}C$ ratio of CH_3CHO ice changes only from 78 in the base model to 93 in the half-CO model. Therefore, complex molecules formed from mixtures of ^{13}C-rich and ^{13}C-poor species, either through radical–radical reactions or through the direct C-atom addition reactions, are not strongly affected by the initial form of carbon.

These results also suggest that, although adopting a more realistic treatment of the prestellar evolution instead of the pseudo-time-dependent model or including isotope-selective photodissociation may change the absolute $^{12}C/^{13}C$ ratios of COMs, their dependence on the initial form of carbon is expected to remain relatively small. In contrast, changes in the elemental $^{12}C/^{13}C$ ratio primarily result in an approximately proportional scaling of the isotopic ratios of molecules, as shown in Section 2.3.4.

Table 2.2:: Dependence of selected molecules on the initial form of carbon. The half-CO model assumes that half of the elemental carbon is initially in the form of CO and the rest in the form of C^+. Values are shown for the end of the collapse phase.

Species	Main precursor	Direct C-addition	Sensitivity	Example ($^{12}C/^{13}C$)
CO	CO reservoir	off	Weak	$68 \rightarrow 68$
CH_3OH	CO-derived	off	Weak	$60 \rightarrow 61$
CH_4	C^+-derived	off	Strong	$133 \rightarrow 225$
CH_3CHO	Mixed origin	off	Moderate	$115 \rightarrow 127$
CH_3CHO	Mixed origin	on	Moderate	$78 \rightarrow 93$

2.4 Discussion

2.4.1 Discussion of Individual Species

CH_2CO

In our base model, CH_2CO gas is depleted in ^{13}C, and $^{12}C/^{13}C \sim 95$ after water ice sublimation (Fig. 2.3). This value is set by the sublimation of CH_2CO ice. CH_2CO

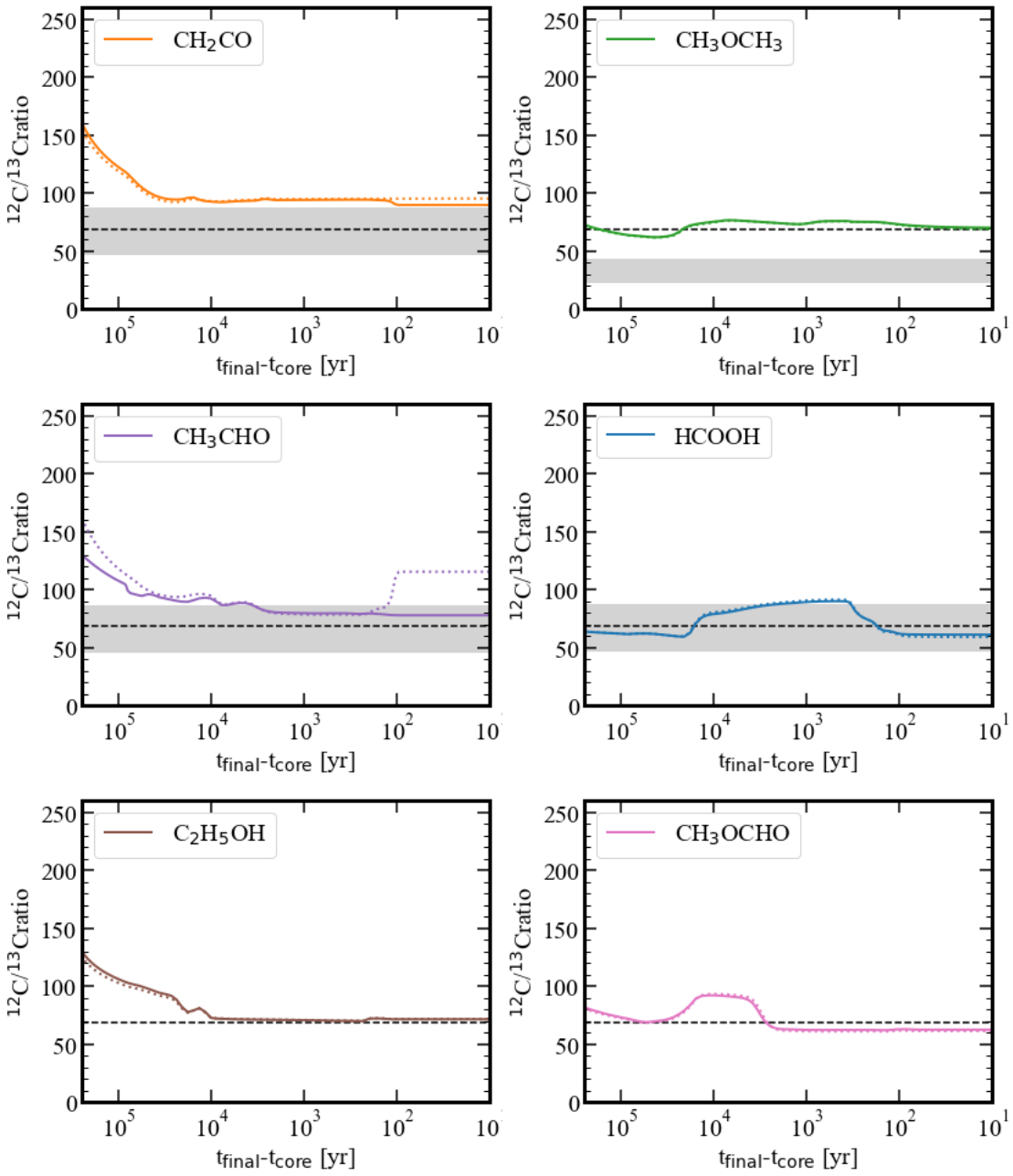

Figure 2.9: Temporal variation of $^{12}C/^{13}C$ ratios of some organic molecules for the base model (dotted lines) and the model with the direct C-atom addition reactions (solid lines). The black horizontal dashed line is for the average $^{12}C/^{13}C$ ratio of local ISM. The observations in IRAS16293-2422B are represented in light gray shaded regions. The observations of C_2H_5OH and CH_3OCHO have large uncertainties, so we refrain from comparing our results with the observations.

ice is mainly formed from C_2 ice on the grain surface via a reaction with atomic O followed by a sequence of hydrogen addition reactions on the grain surfaces in early time (t_{final} - $t_{core} \sim 10^4$ yr) of the collapse phase. C_2 ice is mainly formed from C_2H_2 ice or via the adsorption of gaseous C_2, which become depleted in ^{13}C ($^{12}C/^{13}C \sim 100$) due to the reaction in Eq.(3.4), around 10^6 yr in the static phase. Therefore, the $^{12}C/^{13}C$ ratio of sublimated CH_2CO is depleted in ^{13}C as well. In the model with the direct C-atom addition reactions, the formation of CH_2CO ice is much more efficient in the static phase compared to the base model. CH_2CO ice is formed from C_2O ice on the grain surface via a sequence of hydrogen addition reactions. C_2O ice is formed by the direct C-atom addition reaction, Eq.(2.2). So, the $^{12}C/^{13}C$ ratio of CH_2CO ice ($^{12}C/^{13}C \sim 80$) is lower compared to the base model ($^{12}C/^{13}C \sim 180$) at 10^6 yr in the static phase as well as CH_3CHO ice discussed in Section 2.3.2. Additionally, ^{13}C-depleted CH_2CO ice is also formed in the collapse phase as in the base model. At the CH_2CO sublimation temperature ($\sim$ 40 K, $t_{final} - t_{core} \sim 2 \times 10^3$ yr), CH_2CO ice on the grain surface is desorbed into the gas phase, and the gas-phase CH_2CO becomes strongly ^{13}C-depleted ($^{12}C/^{13}C \sim 95$). At the water sublimation temperature ($\sim$ 120 K, $t_{final} - t_{core} \sim 10^2$ yr), CH_2CO ice residing in the mantle phase—mainly formed during the static phase and enriched in ^{13}C—is released into the gas phase. As a result, the isotopic composition of CH_2CO gas partially relaxes from this highly ^{13}C-depleted state and shifts toward slight ^{13}C enrichment ($^{12}C/^{13}C = 89$; Fig. 2.6), reflecting the isotopic signature of the mantle reservoir. Although this final value remains higher than the local ISM ratio ($\sim$69), it is less ^{13}C-depleted than the value immediately after surface-ice sublimation.

CH_3CHO

Our base model shows that the $^{12}C/^{13}C$ ratio of sublimated CH_3CHO is significantly depleted in ^{13}C ($^{12}C/^{13}C \sim 132$). CH_3CHO ice is formed from ^{13}C-depleted reservoirs in the static phase before 10^5 yr. In addition, in early time (t_{final} - $t_{core} \sim 10^3$ yr, Fig. 2.2) of the collapse phase, CH_3CHO ice is formed from CH_2CO ice via a sequence of hydrogenation reactions or a radical-radical reaction between CH_3 and HCO on the grain surfaces. These reactants are slightly depleted in ^{13}C ($^{12}C/^{13}C \sim 100$). Therefore, sublimated CH_3CHO shows smaller degree of carbon isotope fractionation compared to the CH_3CHO ice formed in the static phase (Fig. 2.3). In the model with the direct C-atom addition reactions, CH_3CHO ice is mainly formed in the static phase due to the direct C-atom addition reaction, Eq.(2.2), and shows small fractionation (see 2.3.2). Unlike CH_2CO, CH_3CHO ice mainly formed in the static phase, so the $^{12}C/^{13}C$ ratio of sublimated CH_3CHO is equal to that of CH_3CHO ice which is formed in the static phase and shows small fractionation. Therefore, the

direct C-atom addition reactions decrease the $^{12}C/^{13}C$ ratio of CH_3CHO to ~ 80.

In this work, we introduced two hydrogenation reactions on grain surfaces; CH_2CO ice + H ice $\rightarrow$ CH_3CO ice and CH_3CO ice + H ice $\rightarrow$ CH_3CHO ice, following Ruaud et al. (2015). The hydrogen addition to CH_2CO ice is the dominant pathway for CH_3CHO ice formation. This pathway also plays an important role in keeping low carbon isotope ratio of CH_3CHO in the direct C-atom addition model since C_2O is formed from ^{13}C-enriched CO and then the subsequent hydrogenation reactions of C_2O on the grain surfaces forms CH_3CHO. Without this hydrogenation pathway of CH_2CO, the $^{12}C/^{13}C$ ratio of CH_3CHO gas is significantly depleted in ^{13}C ($^{12}C/^{13}C$ ~ 120) after water is sublimated, even though we incorporate the direct C-atom addition reactions.

CH_3OCH_3

In our base model, CH_3OCH_3 ice is mainly formed in the collapse phase from ^{13}C-poor CH_3 and ^{13}C-rich CH_3O radical, so the $^{12}C/^{13}C$ ratio of CH_3OCH_3 ice is intermediate value, ~ 75 before the sublimation. In addition, CH_3OCH_3 is formed in the hot gas phase via proton transfer. The gaseous CH_3OCH_3 is formed from the reaction between CH_3OH and $CH_3OH_2^+$ via proton transfer. The $^{12}C/^{13}C$ ratio gradually gets close to that of CH_3OH after the sublimation, and decreases to $\sim$ 68. In the model with the direct C-atom addition reactions, the $^{12}C/^{13}C$ ratio of CH_3OCH_3 is similar to that in the base model because CH_3OCH_3 is mostly formed during the collapse phase and the $^{12}C/^{13}C$ ratio changes with time. Both in the models with and without the direct C-atom addition reactions, the $^{12}C/^{13}C$ ratio of CH_3OCH_3 becomes closer to the ISM value after water ice is sublimated.

HCOOH

In our base model, HCOOH ice is formed from CO in the static phase, so the ice is slightly enriched in ^{13}C (by ~ 10 %) at $t_{core} \sim t_{final}$. The $^{12}C/^{13}C$ ratio of sublimated HCOOH is also slightly enriched in ^{13}C. After the sublimation gaseous HCOOH is additionally formed from H_2CO, which originates from CO, via OH + H_2CO $\rightarrow$ HCOOH. Thus, the $^{12}C/^{13}C$ ratio of HCOOH doesn't change and remains close to that of CO. In the model with the direct C-atom addition reactions, the $^{12}C/^{13}C$ ratio of HCOOH is similar to that in the base model since HCOOH ice is mainly formed from CO during the later static phase ($\sim 10^5$ yr).

C_2H_5OH

In our model, the $^{12}C/^{13}C$ ratio of C_2H_5OH gas is ~ 69 after water ice sublimation. This value is set by the sublimation of C_2H_5OH ice which is mainly formed via radical-radical reaction on the grain surface during the collapse phase. The formation of C_2H_5OH ice involves the rection between ^{13}C-poor CH_3 ice and slightly ^{13}C-rich CH_2OH ice. As a result, the $^{12}C/^{13}C$ ratio of C_2H_5OH aligns with the local ISM value. This remains the case even after including the direct C-atom addition reactions.

CH_3OCHO

In our model, the $^{12}C/^{13}C$ ratio of CH_3OCHO gas is ~ 60 after water ice sublimation. This value is set by the sublimation of CH_3OCHO ice which is mainly formed via radical-radical reaction on the grain surface during the collapse phase. CH_3OCHO ice is formed via radical-radical reaction between ^{13}C-poor CH_3O ice and ^{13}C-rich HCO ice, so the $^{12}C/^{13}C$ ratio of CH_3OCHO is the intermediate value (~ 60) regardless of whether the direct C-atom addition reactions are included.

2.4.2 Comparisons with Observations of IRAS16293-2422B

Table 2.3:: $^{12}C/^{13}C$ ratio for some organic molecules in IRAS16293-2422B and our modeling results.

Species	Observation	Base Model	C-atom Addition
CH_2CO	68 ± 20	95	89
CH_3CHO	67 ± 20	115	78
HCOOH	68 ± 20	59	61
CH_3OCH_3	34 ± 10	68	70

IRAS 16293-2422B is a low-mass protostar harboring a hot corino. Icy grains accrete towards the central hot region surrounding the protostar, and the bulk water ice sublimates at 100 - 200 K. As a result, the composition of the hot corino region is thought to be determined by the ice sublimation. We compare our modeling results to the observational data for the IRAS 16293-2422B, which are obtained by the ALMA-PILS line surveys (Jørgensen et al. 2016, 2018).

In Figure 2.9 and Table 2.3, our results are compared with the observations. Table 2.3 compares the observations and the results of our calculations at $t_{core} \sim$

t_{final} for the base model and the model with the direct C-atom addition reactions. In the base model, sublimated CH_2CO, CH_3CHO, and CH_3OCH_3 are more depleted in ^{13}C than the observations while HCOOH is similar to the observations. In the model with the direct C-atom addition reactions, CH_2CO and CH_3CHO show a smaller fractionation than the base model and are similar to the observational data. This suggests that the direct C-atom addition reactions could play a significant role in the formation of observed organic molecules. However, regardless of the direct C-atom addition reactions, CH_3OCH_3 remains enriched in ^{13}C and the calculated carbon isotope ratio is larger than the observation ($\sim$ 34). We need more investigation to reproduce the observed carbon isotope fractionation of CH_3OCH_3.

As noted in Jørgensen et al. (2018), many lines of the main isotopologues of CH_2CO and HCOOH are optically thick. Therefore, their column densities were not directly determined from the main isotopologue lines, but were inferred from optically thin ^{13}C-isotopologue lines by assuming a standard $^{12}C/^{13}C$ ratio (= 68). This observational procedure introduces an implicit assumption about the carbon isotope ratio, and thus comparisons involving the main-isotopologue column densities should be interpreted with caution. The inferred column densities are consistent with the few optically thin transitions of the main isotopologues.

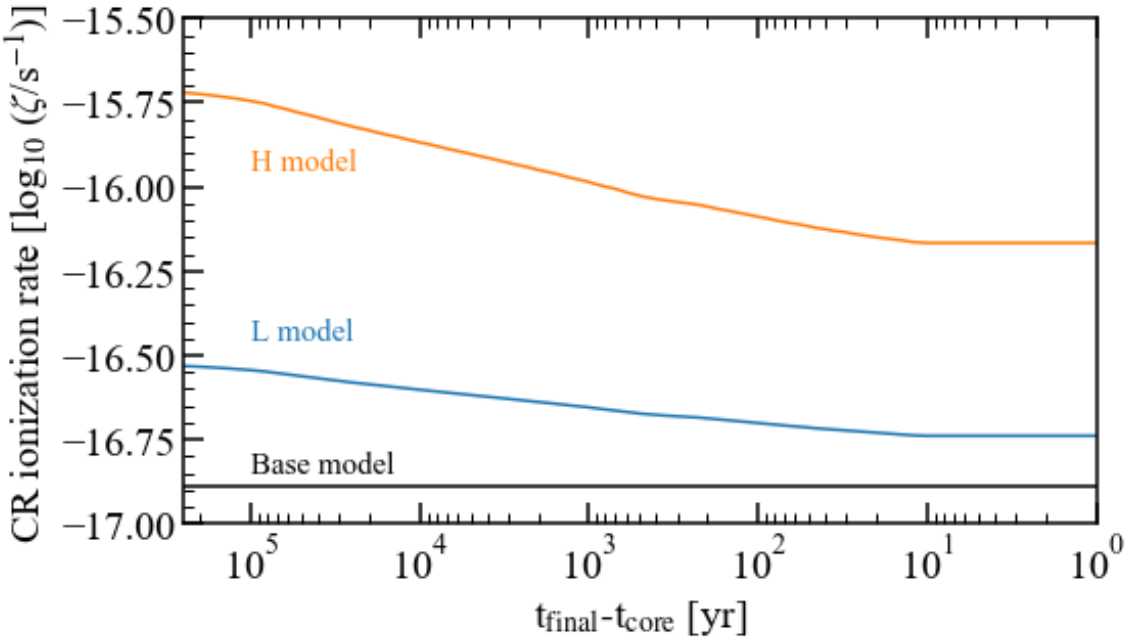

Figure 2.10: Temporal variation of the CR ionization rate per H_2 for the base model (black line), H model (orange line), and L model (blue line) during the collapse phase.

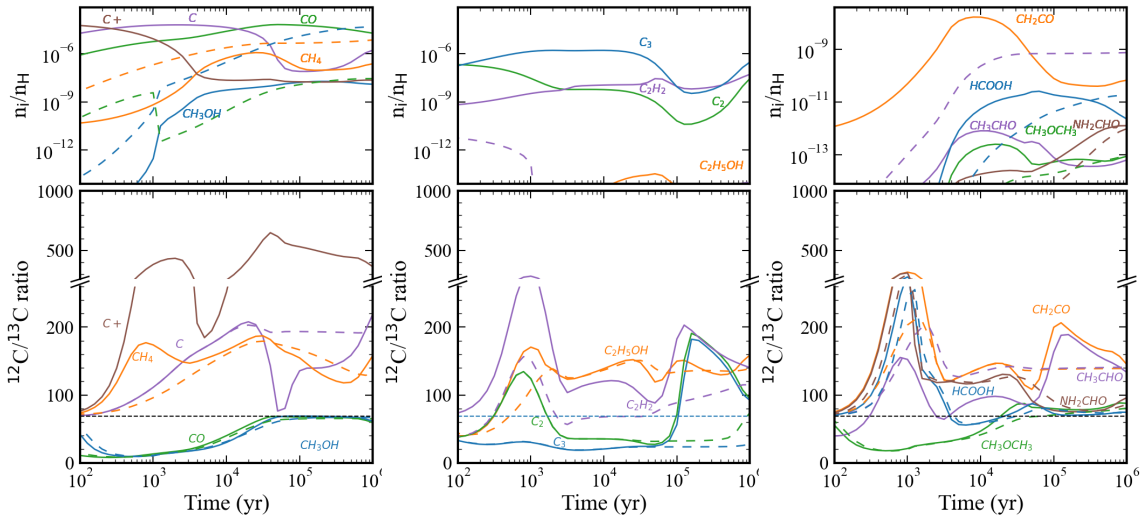

Figure 2.11: Same as Figure 2.2 but for the H model for CR ionization rate

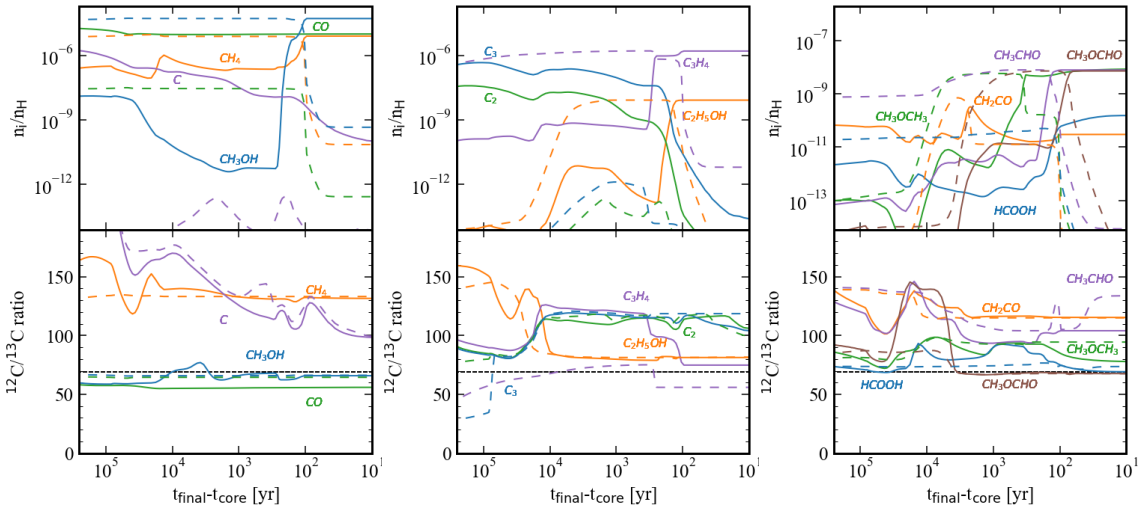

Figure 2.12: Same as Figure 2.3 but for the H model for CR ionization rate

2.4.3 The Effect of Cosmic Ray

In the models presented in Section 2.3, we assume that the cosmic-ray ionization rate of H_2 is constant and is 1.3×10^{-17} s^{-1}. Here we additionally run the astrochemical models with various CR ionization rates.

Interstellar Cosmic Ray Flux

We adopt the CR ionization rate model as a function of gas column density in Padovani et al. (2009, 2018), in which the detailed processes of energy loss and propagation of CR are taken into account. Padovani et al. (2018) considered two models; the L (Low spectrum) model and the H (High spectrum) model for the interstellar CRs proton spectrum. L model comes from the recent data from the extrapolation of the Voyager missions (Cummings et al. 2016), while the H model is from a measurement of H_3^+ in the diffuse medium (Indriolo & McCall 2012). Figure 2.10 shows the temporal variation of the CR ionization rate for the model with the constant CR ionization rate of 1.3×10^{-17} s^{-1}, the H model, and L model. We run the chemical reaction network calculations using the H model and L model for CR ionization rate with and without the direct C-atom addition reactions. This is because, in the L model, the cosmic-ray ionization rate remains close to $1.3 \times 10^{-17}\,\mathrm{s}^{-1}$ over most of the relevant evolutionary timescale, so the ion–neutral chemistry and the resulting isotopic fractionation are not significantly altered.

Figure 2.11 shows the temporal variation of molecular abundances and $^{12}C/^{13}C$ ratios in the static phase in the H model. The higher CR ionization rate leads to the shorter timescale of ion-neutral chemical reactions including isotope exchange reactions. As a result, gaseous CO becomes the dominant carbon reservoir already at $\sim 10^4$ yr. Once most of the carbon is locked in CO, the influence of isotope exchange reactions diminishes. Consequently, the $^{12}C/^{13}C$ ratio of CO gradually approaches the local ISM value. The molecules formed from CO, such as CH_3OH, HCOOH, and CH_3OCH_3 and ices thereof mainly after 10^5 yr, show a smaller degree of fractionation compared to the base model. Other species (e.g. CH_3CHO) and their ices formed from ^{13}C-depleted C^+ or atomic C also show a smaller degree of fractionation compared to those in the base model. Around 10^6 yr higher CR ionization rate leads to atomic C being depleted in ^{13}C because ionized and atomic C has been produced by CRs and the efficiency of the isotope exchange reactions increases (Colzi et al. 2020). Therefore, the molecules formed from C^+ or atomic C, such as gaseous CH_4 also become more depleted in ^{13}C than in the base model at 10^6 yr.

Figure 2.12 shows the temporal variation of molecular abundances and $^{12}C/^{13}C$ ratios in the collapse phase with the H model. In the early time (t_{final} - $t_{core} \sim 10^4$ yr) some icy COMs (e.g. CH_3OCH_3) are produced more efficiently by the higher CR ionization rates, and these are depleted in ^{13}C. The CR-induced UV photons dissociate stable molecules producing radicals on grain surfaces, and then stimulate the formation of COMs on the grain surface. For example, the CH_3 ice on the grain

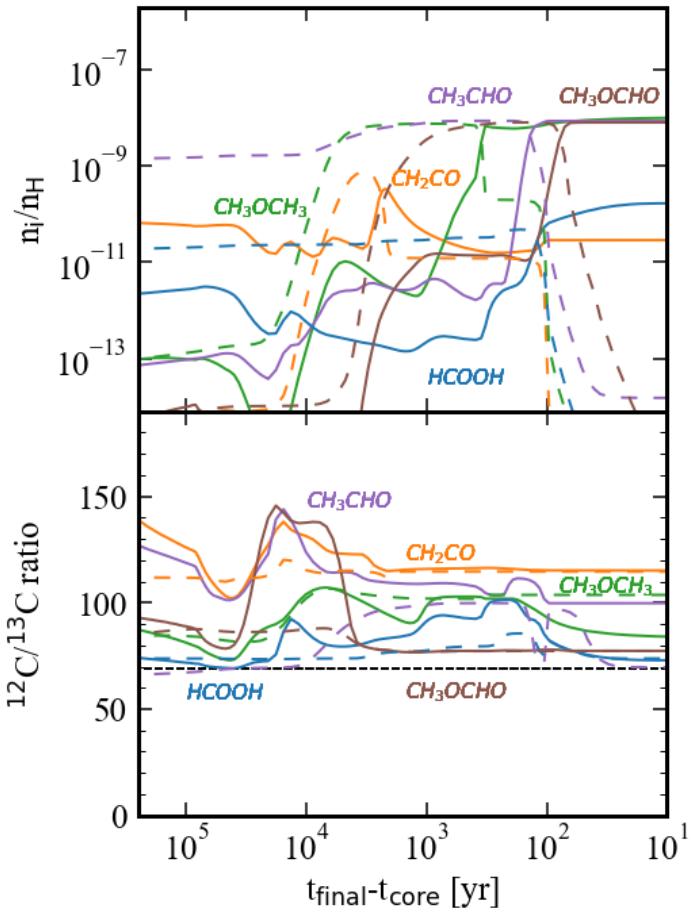

Figure 2.13: Same as right panel of Figure 2.3 but adopting the H model and the direct C-atom addition reactions.

surface is also depleted in ^{13}C since the gaseous CH_4 is depleted in ^{13}C at the end of the static phase. As a result, COMs formed from CH_3 ice by radical-radical reactions on warm grains become more depleted in ^{13}C after water ice sublimation than in the base model. Moreover, for a higher CR ionization rate, the $^{12}C/^{13}C$ ratio of CH_3OCH_3 approaches that of CH_3OH more quickly, because the CR ionization rate promotes the formation of $CH_3OCH_4^+$ via ion-molecule reactions and then the formation of CH_3OCH_3 by the following dissociative recombination, $CH_3OCH_4^+ + e^- \rightarrow CH_3OCH_3$ form CH_3OCH_3 in the warm gas phase. However, the $^{12}C/^{13}C$ ratio of CH_3OCH_3 at $t_{core} \sim t_{final}$ is ~ 80, which is higher than the ISM value. This is because CH_3OCH_3 sublimated together with H_2O is initially significantly depleted in ^{13}C ($^{12}C/^{13}C \sim 95$), and the subsequent gas-phase reactions reduce the ratio only partially.

We incorporate the direct C-atom addition reactions together with the H

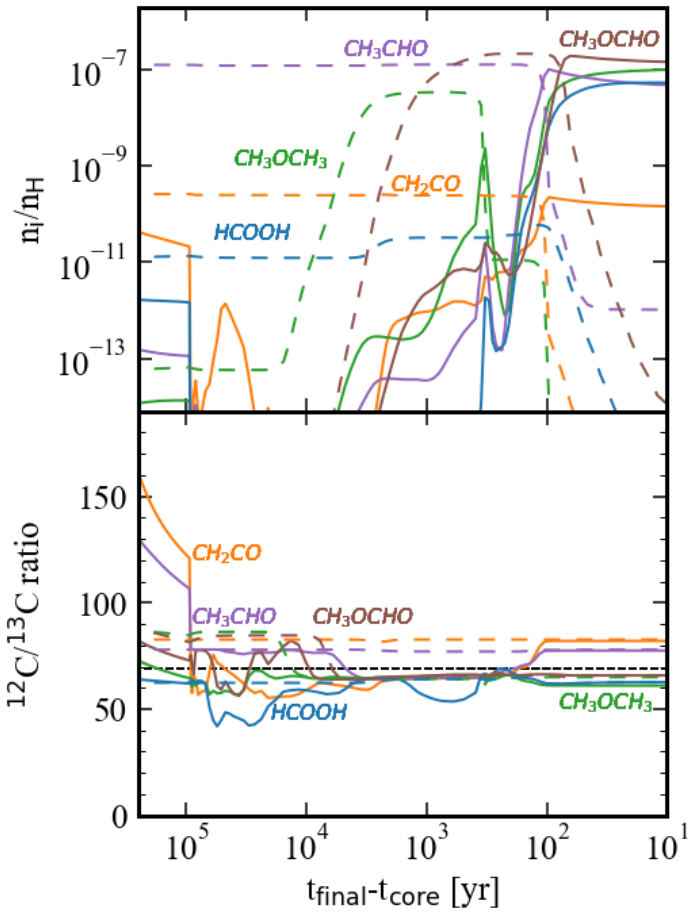

Figure 2.14: Same as right panel of Figure 2.3 but with the direct C-atom addition reactions, and 1.3×10^{-14} s^{-1} as CR ionization rate after the protostar birth.

model. Figure 2.13 shows the temporal variation of molecular abundances and ^{12}C/^{13}C ratios in the collapse phase with the H model and the direct C-atom addition reactions. In the H model, the suppression of ^{12}C/^{13}C ratios of COMs (e.g. CH_3CHO) does not occur even when considering the direct C-atom addition reactions. Atomic C becomes CO and is depleted in the gas phase at $\sim 10^4$ yr in the static phase, so the degree of the direct C-atom addition reactions become smaller, and the abundances of icy COMs produced via the direct C-atom addition reactions in the static phase becomes smaller compared to the model with the constant CR ionization rate of 1.3×10^{-17} s^{-1} and the direct C-atom addition reactions. These icy COMs are much more formed via radical-radical reactions in the collapse phase in the same as the model without the direct C-atom addition reactions. As a result, the ^{12}C/^{13}C ratios of COMs in the warm gas trace those formed on warm dust grains during the collapse phase. For example, the abundance of CH_3CHO ice at 10^6 yr in the static phase decreases by a factor of 100 (the molecular abundance is

$\sim 10^{-9}$) (see also Figure 2.4). On the other hand, the abundance of CH_3CHO ice formed from ^{13}C-depleted CH_3 during the collapse phase is ten times larger than that formed in the static phase. As a result, the $^{12}C/^{13}C$ ratio of CH_3CHO gas after water ice sublimation is depleted in ^{13}C despite incorporating the direct C-atom addition reactions. For the L model, the result is similar to that of the model with the constant CR ionization rate of 1.3×10^{-17} s^{-1}. This is because, in the L model, the cosmic-ray ionization rate remains close to 1.3×10^{-17} s^{-1} over most of the relevant evolutionary timescale, so the ion–neutral chemistry and the resulting isotopic fractionation are not significantly altered.

Cosmic Ray Acceleration after protostar formation

As shown in Sect. 2.4.3, CR ionization rate affects the carbon isotope ratios. In this section, we consider the effect of possible variations of CR ionization rate during the star formation. CRs are suggested to be accelerated by the local shocks around the protostar (Padovani et al. 2015, 2016) such as strongly magnetized shock along the outflow or by the accretion shocks. Cabedo et al. (2023) measured abundances of molecular ions in a solar-type protostellar object and suggest high CR ionization rates of 10^{-16} - 10^{-14} s^{-1}, possibly locally accelerated at shocks. We run the additional model in which we set the CR ionization rate to be 1.3×10^{-14} s^{-1} after the protostellar formation. We note that the CR ionization rate higher than 1.3×10^{-14} s^{-1} destroys COMs via proton transfer by H_3O^+ after sublimation as suggested by Nomura & Millar (2004) and eventually abundance of some molecules (e.g. CH_3CHO and CH_3OCH_3) decrease to around 1×10^{-11} at $t_{core} = t_{final}$. Figure 2.14 shows the temporal variation of molecular abundances and $^{12}C/^{13}C$ ratios in the collapse phase with CR ionization rate of 1.3×10^{-14} s^{-1} and the direct C-atom addition reactions. CH_3OCH_3 is formed from CH_3OH and $CH_3OH_2^+$ via proton transfer after water ice sublimation and then the $^{12}C/^{13}C$ ratio of CH_3OCH_3 approaches that of CH_3OH and becomes enriched in ^{13}C ($\sim$ 60). Consequently, the $^{12}C/^{13}C$ ratio of CH_3OCH_3 decreases if the CR ionization rates become high only in the collapse phase. However, the ratio is still higher than the observation towards IRAS16293-2422B (Jørgensen et al. 2018). For other selected molecules, the $^{12}C/^{13}C$ ratios of HCOOH, CH_2CO, CH_3CHO are similar to those in the base model with the direct C-atom addition reactions (see a right panel of Fig. A2).

2.5 Summary

We investigated the carbon isotope fractionation of COMs from prestellar cores to protostellar cores by combining the chemical network model and the radiation hydrodynamical simulation. The temporal variation of the molecular abundances and $^{12}C/^{13}C$ ratios were calculated by conducting calculations of a gas-grain chemical network within a single fluid parcel. Our main findings are the following.

1. In the static prestellar phase, due to the carbon isotope exchange reactions, the molecules formed from atomic C and C^+ were depleted in ^{13}C, while the molecules formed from CO were around 10 % enriched in ^{13}C at the end of the static phase. COMs have various $^{12}C/^{13}C$ ratios depending on the $^{12}C/^{13}C$ ratios of their reactants.

2. In the collapse phase, after the protostar formation where species are sublimated to the gas phase, the $^{12}C/^{13}C$ ratios of some sublimated species (e.g. CH_4 and CH_3OH) reflected those of their icy counterparts. On the other hand, the $^{12}C/^{13}C$ ratios of other species are affected by chemical reactions during the collapse phase. Some COMs (e.g. CH_3CHO) were formed on warm grain surfaces during the collapse phase as much as in the static phase. As a result, the $^{12}C/^{13}C$ ratios of these COMs were different from those of their icy counterparts formed in the static phase. In addition, some COMs (e.g. CH_3OCH_3) were formed in the warm gas phase after water ice sublimation, which also affects their carbon isotope ratios. Eventually, in our base model, some complex molecules (e.g. CH_3CHO and CH_3OCH_3) become more depleted in ^{13}C compared to the observations.

3. We incorporated the direct C-atom addition reactions into our base model and investigated the effect of these reactions on the formation and the $^{12}C/^{13}C$ ratios of COMs. Direct C-atom addition reactions altered the $^{12}C/^{13}C$ ratios of molecules, reducing the diversity of the carbon isotope ratios. This is due to the additional formation of specific species (e.g., H_2CO and C_2O), which further lead to the production of COMs. Our results reproduced the observations of the $^{12}C/^{13}C$ ratios of some complex molecules including COMs (CH_2CO, CH_3CHO, and HCOOH) in the Class 0 source, IRAS16293-2422B, which were comparable to the elemental $^{12}C/^{13}C$ ratio in the local ISM. However, CH_3OCH_3 in our results still shows depletion of ^{13}C compared to the observations.

4. We investigated the effect of various CR ionization rates on carbon isotope ratios of complex molecules. During the static phase, high cosmic ray (CR)

ionization rates are considered unfavorable for the formation of complex organic molecules. Consequently, the formation of ^{13}C-rich COMs through direct C-atom addition reactions becomes less efficient. Instead, ^{13}C-depleted radicals, such as CH_3, tend to form COMs on warm grain surfaces during the collapse phase. On the other hand, ion-molecule reactions in the warm gas phase reduced the $^{12}C/^{13}C$ ratio of CH_3OCH_3 after water ice sublimation. Especially, when the CR ionization rates become as high as 1.3×10^{-14} s^{-1} only after protostar formation, this ratio becomes enriched in ^{13}C. However, the $^{12}C/^{13}C$ ratio of CH_3OCH_3 at the end of the collapse phase was still higher than the observations.

Appendix to Chapter 2

A.1 Additional figures

A.1.1 Carbon- and Oxygen-bearing molecules

Figure A1 and A2 show the temporal variation of abundances and the $^{12}C/^{13}C$ ratios of some molecules with the direct C-atom addition reactions in the static phase and collapse phase, respectively.

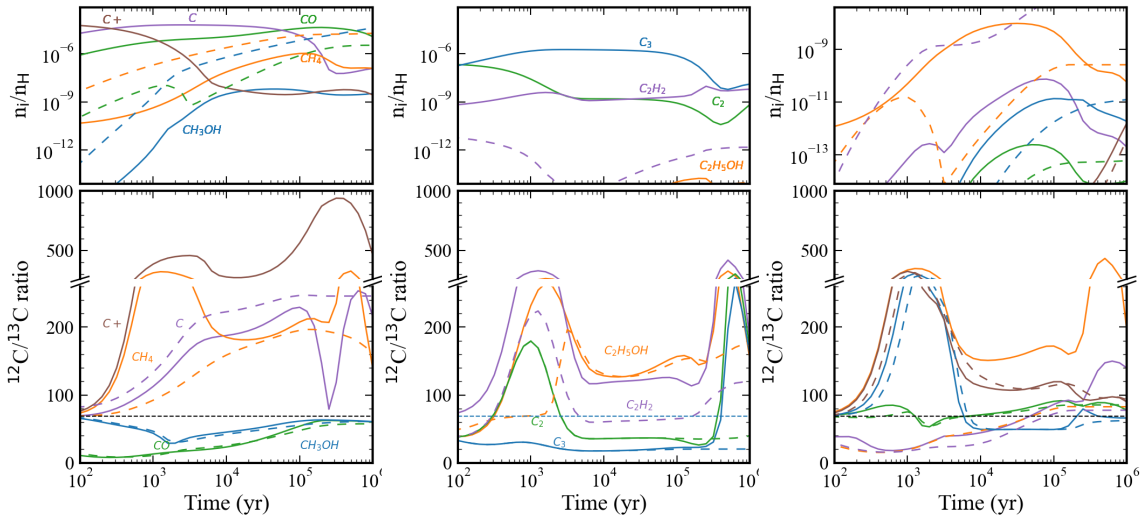

Figure A1: Same as Figure 2.2 but adopting the direct C-atom addition reactions

Figure A3 shows the temporal variation of abundance and the $^{12}C/^{13}C$ ratio of HCCO gas. HCCO is formed from C_2O ice which is formed via direct C-atom addition reaction 3.3. Therefore, after incorporating the direct C-atom addition reactions the abundance increases, and the $^{12}C/^{13}C$ ratio decreases. HCCO was observed toward the starless core (Agúndez et al. 2015), where they reported the column density ratio of HCCO and H_2, ranging from 10^{-13} to 10^{-11}. In our model,

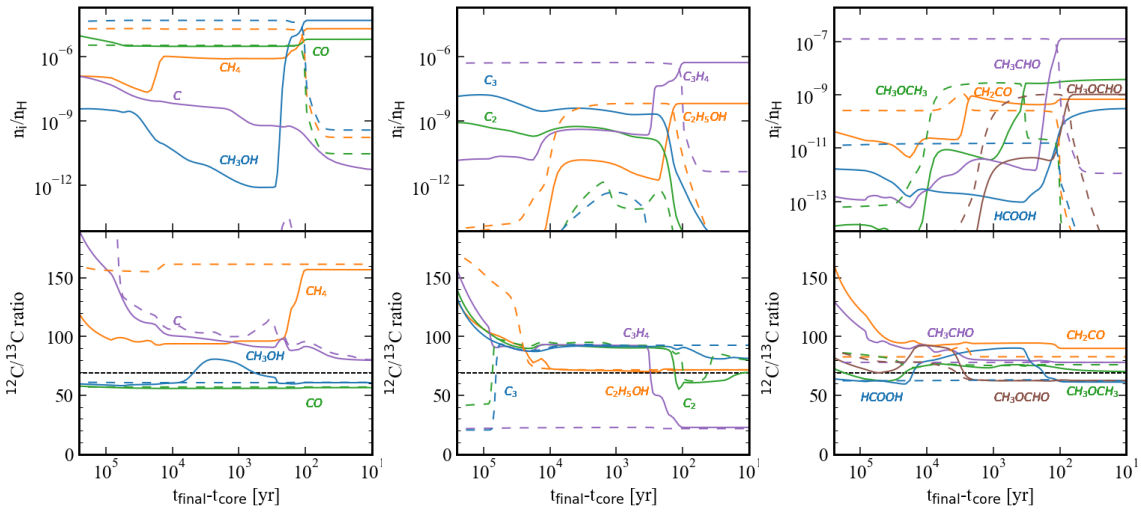

Figure A2: Same as Figure 2.3 but adopting the direct C-atom addition reactions.

HCCO gas to H_2 gas ratio at typical dense cloud age ($\sim 10^5$ yr) in the static phase increases from 4.4×10^{-14} to 3.5×10^{-10} with the direct C-atom addition reaction 3.3. This means that HCCO gas is efficiently formed via the direct C-atom addition reaction 3.3 even at low-temperature environments. The $^{12}C/^{13}C$ ratio of HCCO gas decreases from 160 to 80 at a typical dense cloud age, and from 93 to 85 after water ice sublimates. Therefore, measuring the $^{12}C/^{13}C$ ratio of HCCO by observation could confirm whether the direct C-atom addition reactions contribute to forming COMs.

A.1.2 Nitrogen-bearing molecules

Figures A4 and A5 show the temporal variation of abundances and $^{12}C/^{13}C$ ratios of nitrogen-bearing species in the static phase and the collapse phase, respectively. These results in the static phase in our model are similar to the results in Colzi et al. (2020) and Loison et al. (2020). The $^{12}C/^{13}C$ ratios are affected by carbon isotope exchange reactions. In particular, CN, HCN, and HNC become ^{13}C-rich in the early static phase, showing $^{12}C/^{13}C$ ratios lower than the elemental ratio. This behavior is consistent with observational results in cold molecular clouds (e.g., Daniel et al. 2013; Magalhães et al. 2018). Some molecules (e.g. HNCO, H_2CN, NH_2CHO and CH_3NH) show different time variations compared to our base model at around 10^4 yr in the static phase due to the direct C-atom addition reaction 3.2. These molecules are formed from H_2CO ice. In the base model HNCO, H_2CN, and NH_2CHO are partly formed from ^{13}C-enriched CO and H_2CO, but in the model with the direct

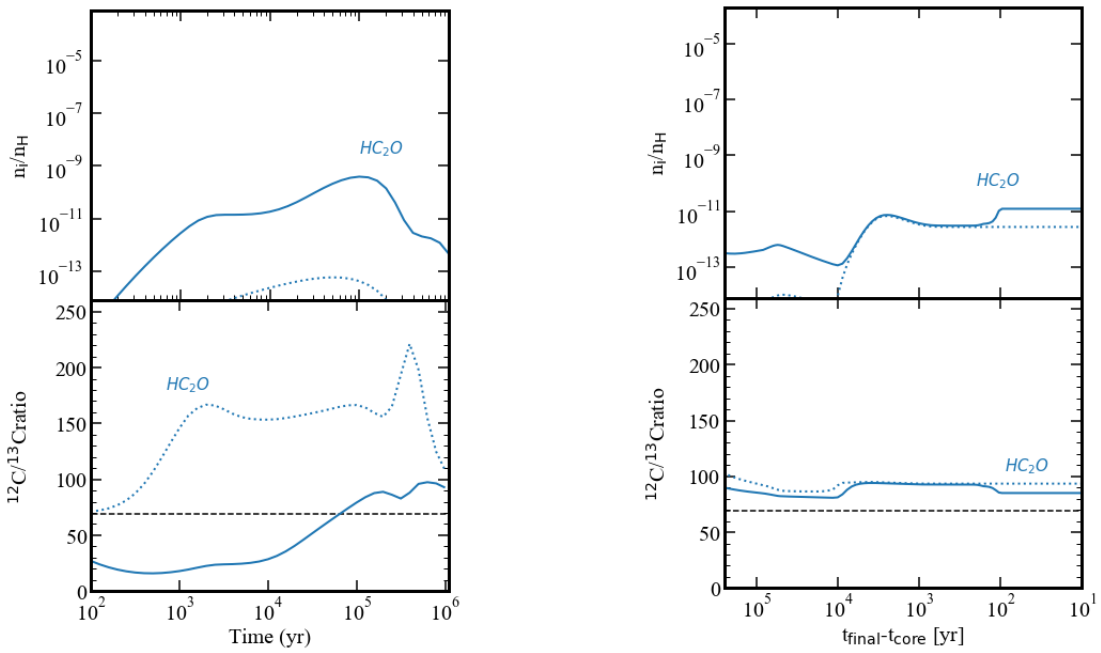

Figure A3: The temporal variation of abundance and the $^{12}C/^{13}C$ ratio of HC_2O gas for the base model (dotted lines) and the model with the direct C-atom addition reactions (solid lines). The left panel is for the static phase and the right panel is for the collapse phase.

C-atom addition reactions H_2CO is formed via Reaction 3.2 and is depleted in ^{13}C, similar to atomic C. Therefore, the $^{12}C/^{13}C$ ratios of these molecules increase when the direct C-atom addition reactions are incorporated. CH_3NH is formed from CH_3 or H_2CN, so the $^{12}C/^{13}C$ ratio changes by the direct C-atom addition reactions. Around 10^6 yr, however, these differences are no longer evident because H_2CO ice is formed from CO ice via a sequence of hydrogenation reactions on the grain surface. In the collapse phase, there is no difference between our base model and the model with the direct C-atom addition reactions. For HC_3N, the $^{12}C/^{13}C$ ratio depends on the position of ^{13}C within the molecules. Therefore, we will address these aspects in future work.

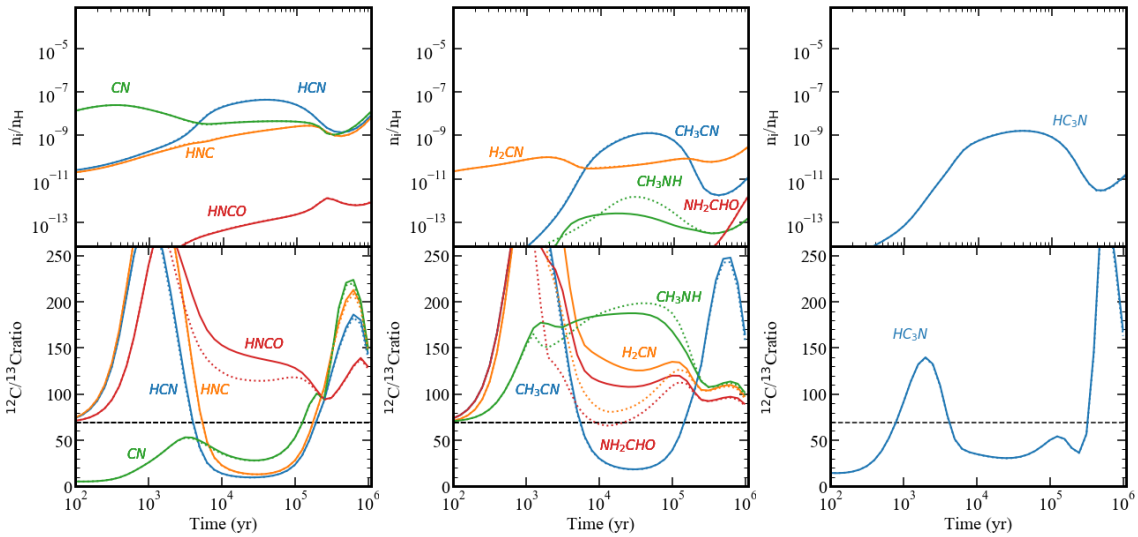

Figure A4: Temporal variation of the molecular abundances and $^{12}C/^{13}C$ ratios for gaseous species during the static phase in the model with the direct C-atom addition reactions (solid lines) and the base model (dashed lines). The horizontal black dashed line represents the average $^{12}C/^{13}C$ ratio of local ISM.

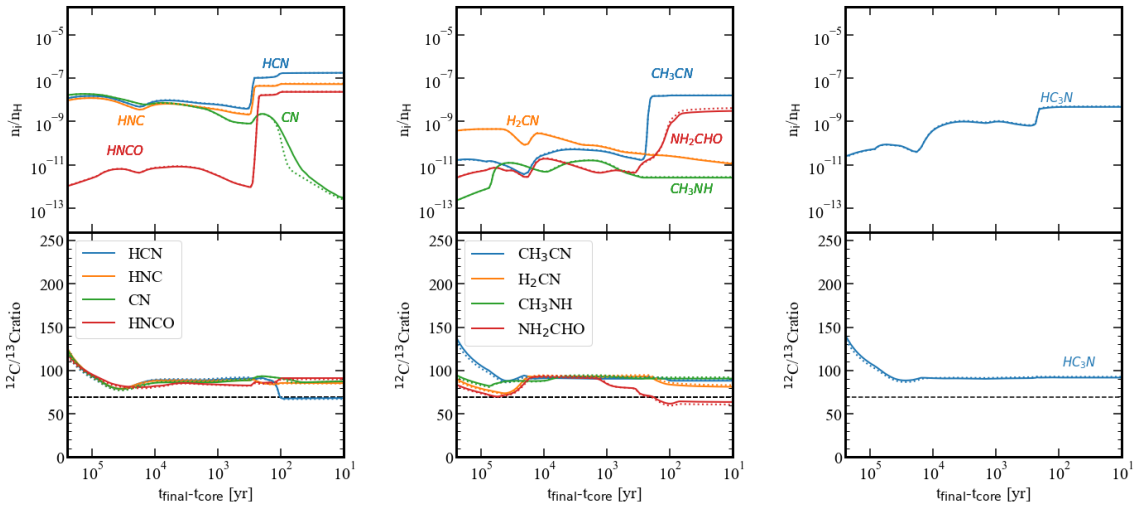

Figure A5: Same as Figure A4 but for during the collapse phase.

Chapter 3

Isotopomer-Specific Carbon Isotope Ratio of Complex Organic Molecules in Star-Forming Cores

This thesis chapter originally appeared in the literature as
Ichimura, R., Nomura, H., Furuya, K., Hama, T., and T. J. Millar. 2025,
ACS Earth and Space Chemistry, in press

3.1 Introduction

In this chapter, we develop an astrochemical model that explicitly tracks the position of ^{13}C atoms throughout reaction sequences, allowing for the evaluation of isotopomer-specific carbon fractionation in COMs under astrophysical conditions. By using cheminformatics tools, we systematically track the position of carbon atoms across chemical reactions. With our new chemical network, we evaluate how the resulting isotopomer ratios reflect the physical environment and chemical history of COMs in star-forming regions. The rest of this chapter is structured as follows: Section 3.2 describes the construction of our position-conserved reaction network and the physical and chemical model used in the simulations, while the detailed construction of the ^{13}C isotopomer-resolved chemical network is described in Appendix A. Section 3.3 presents the results of our calculations during the static and collapse phases. In Section 3.4, we discuss the implications of our findings, including comparisons to the full-scrambling model and observed isotopomer ratios. Finally, we summarize our findings in Section 3.5.

3.2 Model Description

3.2.1 Overview

A new chemical reaction network has been developed to describe carbon isotope fractionation among isotopomers. This network is based on Garrod (2013), with modifications that include ^{13}C isotope chemistry, non-thermal radiolysis chemistry in the bulk ice, and several other minor updates. Details of the main modifications are provided in the following sections. These modifications include the addition of ∼1600 new isotopically labeled species and ∼45500 reactions involving ^{13}C-bearing molecules and non-thermal radiolysis reactions. As a result, our complete reaction network consists of approximately ∼2900 species across the gas, ice surface, and ice mantle phases, and ∼59000 reactions covering both gas-phase and ice-phase chemistry. We solve the updated chemical reaction network using a gas-ice astrochemical code based on the rate equation approach (Rokko code; Furuya et al. (2015)). We adopt the three-phase gas-ice chemistry model developed by Hasegawa & Herbst (1993), consisting of three components: the gas phase, the ice surface, and the bulk ice mantle. Following Vasyunin & Herbst (2013), we treat the top four monolayers of the ice mantle as chemically active.

3.2.2 Carbon Isotope Chemistry

Carbon isotope exchange reactions in the gas phase are taken from Colzi et al. (2020); Loison et al. (2020); Sipilä et al. (2023). We extend the Garrod (2013) reaction network by explicitly considering the positional distribution of ^{13}C atoms in isotopologues containing fewer than four carbon atoms (e.g., $^{13}CH_3COCH_3$ and $CH_3{}^{13}COCH_3$ for CH_3COCH_3, acetone). Although the full network includes species with up to ten carbon atoms, this isotopomer-specific treatment is restricted to smaller molecules for computational feasibility and because observational constraints are mostly available for such species. In gas-phase chemistry, we assume that all reactions involving ^{13}C, except for proton transfer and charge transfer reactions, proceed through full scrambling, following the treatment of Colzi et al. (2020). This assumption applies to the statistical redistribution of carbon atoms within reaction intermediates and is adopted for both open-shell and closed-shell species. Molecules such as CCS, C_2H, and HC_3N, for which specific isotope exchange reactions are explicitly included in the network, are treated separately and are therefore not governed by the generic scrambling assumption. While full scrambling represents a simplifying approximation and may not strictly apply to all reaction

classes, it provides a consistent and tractable framework in the absence of detailed state-specific laboratory constraints. In full scrambling, the reactants form an intermediate complex that persists long enough for the constituent atoms to undergo complete rearrangement (Gerlich & Horning 1992). Full scrambling involving ^{13}C isotope species leads to two outcomes (see the left of Figure A.1). One corresponds to the position of the ^{13}C atom being retained from a specific reactant into the product, while the other corresponds to the interchange of the ^{13}C atom between reactants. The branching ratios are constructed based on statistical weights, which reflect the number of carbon atoms and their possible arrangements in the intermediate complex. Specifically, we calculate the branching ratios by multiplying simple probabilities associated with the possible positions of the ^{13}C atoms in the products. For example, in a reaction involving two carbon atoms, the probability of forming each isotopomer is proportional to the number of indistinguishable ways to assign ^{13}C to a given carbon position, assuming full scrambling. For proton transfer and charge transfer reactions, it is assumed that no atoms, including carbon atoms, within the reactants undergo interchange during the chemical process.

Here, we assume that the interchange of carbon atoms (^{12}C and ^{13}C) does not occur in ice-phase reactions (e.g, hydrogen abstractions, hydrogenation reactions, radical-radical reactions, photodissociation reactions), and accordingly construct a carbon atom position-conserved reaction network. Based on the theoretical study (Cooper & Kästner 2019), during hydrogen abstraction from closed-shell molecules such as CH_3OH, the carbon atom transiently shifts toward the departing hydrogen atom along the reaction coordinate, but ultimately returns to its original position within the molecular framework. Therefore, we neglect the interchange of carbon atoms through hydrogen abstraction reactions. We also neglect the interchange of carbon atoms during hydrogenation reactions. A pre-reactive minimum or a van der Waals complex formed in these reactions does not evolve into an intermediate complex or a transition state where the atomic interchange occurs. Instead, the product is considered to result from hydrogen tunneling from bound metastable states (Meisner & Kästner 2016). Radical–radical reactions in the ice generally have low activation barriers, and their transition states typically involve only the translation and/or rotation of the radicals, thereby preventing the interchange of carbon atoms (Enrique-Romero et al. 2022). Furthermore, the chemical networks of Garrod (2013) and Garrod et al. (2008), which form the foundation of our model, assume that no intramolecular rearrangement occurs during radical–radical reactions and that the structures of the products directly reflect those of the reacting radicals in the ice phase. Consistent with these theoretical and modeling considerations, our ^{13}C chemical network does not allow for carbon scrambling in radical–radical reactions, thereby preserving the original positions of ^{13}C within the molecules. For

example, when each reactant has a carbon atom, we assume that the product inherits positions of ^{12}C and ^{13}C in a functional group (e.g., CH_3 and CHO) from each reactant. For example, in a radical-radical reaction for the formation of acetaldehyde (CH_3CHO):

$$CH_3 + HCO \rightarrow CH_3CHO, \tag{3.1}$$

the 'HCO' in the reactant and the formyl group 'CHO' of a product are common structures. When a ^{13}C atom is present in the 'HCO' of the reactant, it is conserved in the 'CHO' of the product (Eq.(3.2)). Similarly, when a ^{13}C atom is present in the "CH_3" of the reactant, it remains in the methyl group "CH_3" of the product (Eq.(3.3)):

$$CH_3 + H^{13}CO \rightarrow CH_3^{13}CHO, \tag{3.2}$$

$$^{13}CH_3 + HCO \rightarrow {}^{13}CH_3CHO. \tag{3.3}$$

Dissociation processes within the ice, such as photodissociation or recombination, may cleave only a single chemical bond within a molecule, so the interchange of carbon atoms may not occur. The detailed procedure for constructing the ^{13}C isotopologue and isotopomer-resolved reaction network, including how carbon-atom positions are tracked and conserved, is described in Appendix A.

3.2.3 Cosmic-ray-induced Non-thermal Reaction

To describe cosmic-ray-induced non-thermal chemistry in the ice phase, we adopt the cosmic-ray-induced radiolysis framework of Shingledecker et al. (2018). Radiolysis processes are assumed to operate both on grain surfaces and within the bulk ice mantle. The primary dissociation and excitation channels included in this work are summarized in Table 3.1. These processes correspond to the Type I–III reactions described in Section 1.3.3. Type I (reaction 1.9) reactions produce suprathermal fragments, Type II (reaction 1.10) reactions represent dissociation after rapid thermalization, and Type III (reaction 1.11) reactions correspond to non-dissociative excitation. The branching fractions $f_{\rm br}$ and radiochemical yields (G-values) are adopted directly from Table 4 of Shingledecker et al. (2018) without modification.

Table 3.1:: Solid-phase radiolysis processes adopted in this work. Suprathermal species are indicated by *. (Adopted from Table 4 of Shingledecker et al. 2018.)

Number	Process	$f_{\rm br}$	G-value	Type
	H_2O			

Number	Process	$f_{\rm br}$	G-value	Type
1	$H_2O \rightsquigarrow O^* + H_2^*$	0.500	3.704	I
2	$H_2O \rightsquigarrow OH^* + H^*$	0.500	3.704	I
3	$H_2O \rightsquigarrow OH + H$	1.000	1.747	II
4	$H_2O \rightsquigarrow H_2O^*$	1.000	1.747	III
	O_2			
5	$O_2 \rightsquigarrow O^* + O^*$	1.000	3.704	I
6	$O_2 \rightsquigarrow O + O$	1.000	2.138	II
7	$O_2 \rightsquigarrow O_2^*$	1.000	2.138	III
	O_3			
8	$O_3 \rightsquigarrow O_2^* + O^*$	1.000	3.704	I
9	$O_3 \rightsquigarrow O_2 + O$	1.000	4.059	II
10	$O_3 \rightsquigarrow O_3^*$	1.000	4.059	III
	CO			
11	$CO \rightsquigarrow C^* + O^*$	1.000	3.704	I
12	$CO \rightsquigarrow C + O$	1.000	1.269	II
13	$CO \rightsquigarrow CO^*$	1.000	1.269	III
	CO_2			
14	$CO_2 \rightsquigarrow CO^* + O^*$	1.000	3.704	I
15	$CO_2 \rightsquigarrow CO + O$	1.000	1.249	II
16	$CO_2 \rightsquigarrow CO_2^*$	1.000	1.249	III
	NO			
17	$NO \rightsquigarrow N^* + O^*$	1.000	3.704	I
18	$NO \rightsquigarrow N + O$	1.000	1.922	II
19	$NO \rightsquigarrow NO^*$	1.000	1.922	III
	NO_2			
20	$NO_2 \rightsquigarrow NO^* + O^*$	1.000	3.704	I
21	$NO_2 \rightsquigarrow NO + O$	1.000	1.207	II
22	$NO_2 \rightsquigarrow NO_2^*$	1.000	1.207	III
	O_2H			
23	$O_2H \rightsquigarrow OH^* + O^*$	1.000	3.704	I
24	$O_2H \rightsquigarrow OH + O$	1.000	3.714	II
25	$O_2H \rightsquigarrow O_2H^*$	1.000	3.714	III
	H_2O_2			
26	$H_2O_2 \rightsquigarrow OH^* + OH^*$	0.500	3.704	I
27	$H_2O_2 \rightsquigarrow O^* + H_2O^*$	0.500	3.704	I
28	$H_2O_2 \rightsquigarrow OH + OH^*$	1.000	2.296	II
	NH_3			
29	$NH_3 \rightsquigarrow H^* + NH_2^*$	0.500	3.704	I

Number	Process	$f_{\rm br}$	G-value	Type
30	$NH_3 \rightsquigarrow H_2^* + NH^*$	0.500	3.704	I
31	$NH_3 \rightsquigarrow H + NH_2$	1.000	2.721	II
32	$NH_3 \rightsquigarrow NH_3^*$	1.000	2.721	III
	CH_4			
33	$CH_4 \rightsquigarrow H^* + CH_3^*$	0.500	3.704	I
34	$CH_4 \rightsquigarrow H_2^* + CH_2^*$	0.500	3.704	I
35	$CH_4 \rightsquigarrow H + CH_3$	1.000	1.505	II
36	$CH_4 \rightsquigarrow CH_4^*$	1.000	1.505	III
	H_2CO			
37	$H_2CO \rightsquigarrow H^* + HCO^*$	1.000	3.704	I
38	$H_2CO \rightsquigarrow H + HCO$	1.000	2.910	II
39	$H_2CO \rightsquigarrow H_2CO^*$	1.000	2.910	III
	CH_3OH			
40	$CH_3OH \rightsquigarrow H^* + CH_3O^*$	0.333	3.704	I
41	$CH_3OH \rightsquigarrow H^* + CH_2OH^*$	0.333	3.704	I
42	$CH_3OH \rightsquigarrow OH^* + CH_3^*$	0.333	3.704	I
43	$CH_3OH \rightsquigarrow H + CH_3O$	0.333	1.571	II
44	$CH_3OH \rightsquigarrow H + CH_2OH$	0.333	1.571	II
45	$CH_3OH \rightsquigarrow OH + CH_3$	0.333	1.571	II
46	$CH_3OH \rightsquigarrow CH_3OH^*$	1.000	1.571	III

Suprathermal fragments generated in Type I and Type III processes are treated as highly reactive species with negligible diffusion timescales. Their subsequent reactions with neighboring stable ice molecules are implemented using the grain-surface reaction network of Garrod (2013). When one of the reactants is suprathermal, activation energy barriers are removed, allowing otherwise kinetically forbidden reactions to proceed at low temperatures. In this way, suprathermal chemistry is incorporated by modifying the energetics of the corresponding ice-phase reactions already present in the network. For example, the surface reaction

$$CH_3 + HCO \rightarrow CH_3CHO$$

is treated in the present model such that suprathermal variants of either reactant are also included:

$$CH_3^* + HCO \rightarrow CH_3CHO,$$

$$CH_3 + HCO^* \rightarrow CH_3CHO.$$

These additional channels are incorporated consistently within the ice-surface and ice-mantle reaction network.

3.2.4 Other Modifications and Parameters

In addition to the major modifications, we also implement several other modifications and assumptions in our chemical network. While radical–radical reactions such as CH_3 + HCO → CH_3CHO are generally considered to be barrierless—as is the case in the gas phase, supported by experimental and theoretical studies (Callear & Cooper 1990; Knyazev 2017)—the presence of surrounding water ice may introduce intermolecular interactions that hinder direct recombination. Following the quantum chemical calculations of Enrique-Romero et al. (2019), we adopt effective energy barriers of 800 K and 1200 K for CH_3CHO formation and for the competing hydrogen abstraction pathway CH_3 + HCO → CH_4 + CO, respectively. These values reflect the energy cost of overcoming interactions with the surrounding ice matrix, rather than intrinsic activation barriers of the reactions themselves. We note that Enrique-Romero et al. (2022) slightly updated the activation energies to 5.5 kJ mol^{-1} and 7.2 kJ mol^{-1}, respectively; however, converting these values to Kelvin (approximately 660 K and 870 K) yields comparable barriers, and adopting them does not affect our model results. In our model, we also assume that these reactions proceed without carbon atom scrambling. This assumption is based on the fact that the intrinsic reactions are effectively barrierless and that, once the surrounding ice interactions are overcome, the transition state involves only the translation and/or rotation of the radicals. As is typical for radical–radical reactions, no rearrangement of the carbon backbone is expected, and the original position of each ^{13}C atom within the molecular structure is preserved. A fraction of the adsorbed carbon undergoes direct Eley–Rideal (ER) reactions with surface H_2O and CO ice, following the approach of Chapter 2, while the remainder becomes trapped in either physisorbed or chemisorbed states. Although physisorbed atomic carbon may retain some mobility, as discussed by Tsuge et al. (2023); Tsuge et al. (2024), we adopt a binding energy of 10,000 K—consistent with chemisorption values from Wakelam et al. (2017)—to represent its interaction with the ice, thereby simplifying its treatment in the reaction network.

We adopt the low-metal elemental abundances listed in Table 2.1 from Aikawa et al. (2001), along with the elemental $^{12}C/^{13}C$ ratio representative of the local ISM ($^{12}C/^{13}C$ = 69) (Milam et al. 2005a). The dust grain is spherical with a 0.1 µm radius with the material density of 2.5 g/cm^3(Draine 2003). The dust-to-gas mass ratio is set to 0.01 (Lombardi et al. 2014). The cosmic-ray ionization rate of H_2 is set to be 1.3×10^{-17} s^{-1} (Terzieva & Herbst 1998). Ice species are assumed to have a single binding energy. The diffusion energy is set to 40 % of the binding energy for most species, except for atomic hydrogen. We set the diffusion energy of H atoms to 330 K, which corresponds to the energy barrier for the deep potential sites (Hama

et al. 2012). To prevent nitrogen atoms from diffusing more easily than H atoms, we assume a diffusion energy of 500 K for atomic nitrogen. In the ice mantle, the binding energies of the species, except H and H_2, are the same as water ice (5700 K). This assumption reflects the fact that interstellar ice mantles are dominated by amorphous water ice, so that most adsorbed species interact primarily with an H_2O-rich substrate rather than with bare grain surfaces or pure molecular ices. The diffusion energy in the mantle is set to 80% of the binding energy, larger than the 40% adopted for the surface, in order to mimic the significantly slower bulk diffusion within amorphous water ice. This treatment follows the conventional three-phase approach in astrochemical models (e.g., Ruaud et al. 2016)

We calculate the evolution of molecular abundances with a chemical reaction network along a single fluid parcel as done in Aikawa et al. (2020) and Chapter 2.

3.3 Results

3.3.1 Static Phase

Figure 3.1 shows the temporal evolution of the abundances and $^{12}C/^{13}C$ ratios for dominant carbon-bearing species in the gas and ice during the static phase. As discussed in Chapter 2 and in previous studies (Furuya et al. 2011; Colzi et al. 2020; Loison et al. 2020), carbon isotope exchange reaction

$$^{13}C^+ + {}^{12}CO \rightleftharpoons {}^{12}C^+ + {}^{13}CO + 35K, \tag{3.4}$$

leads to ^{13}C enrichment in CO, while C and C^+ become ^{13}C-poor. This fractionation pattern is established within $\sim 10^3$ years and gradually relaxes toward the local ISM value ($^{12}C/^{13}C = 69$) after 10^5 years as carbon becomes sequestered in CO as described in Chapter 2. This gas-phase fractionation is transferred to the isotope composition of molecules formed on grains via adsorption and surface reactions.

In our model, COMs predominantly form in cold environments (10 K) during the static phase via two-body reactions with suprathermal species induced by radiolysis in the ice mantle. Upper panels of Figure 3.2 present the temporal evolution of the abundances of selected COMs and their isotopic ratios. Radiolysis of ice components, such as CH_4, CH_3OH, and H_2CO, produces suprathermal species (e.g., CH_3, CH_2OH, HCO), which undergo barrierless reactions with nearby species, rather than being saturated through hydrogenation. These reactions dominate both the surface and mantle chemistry. The $^{12}C/^{13}C$ ratios of the produced COMs are governed by those of their precursor suprathermal species or radicals. Also,

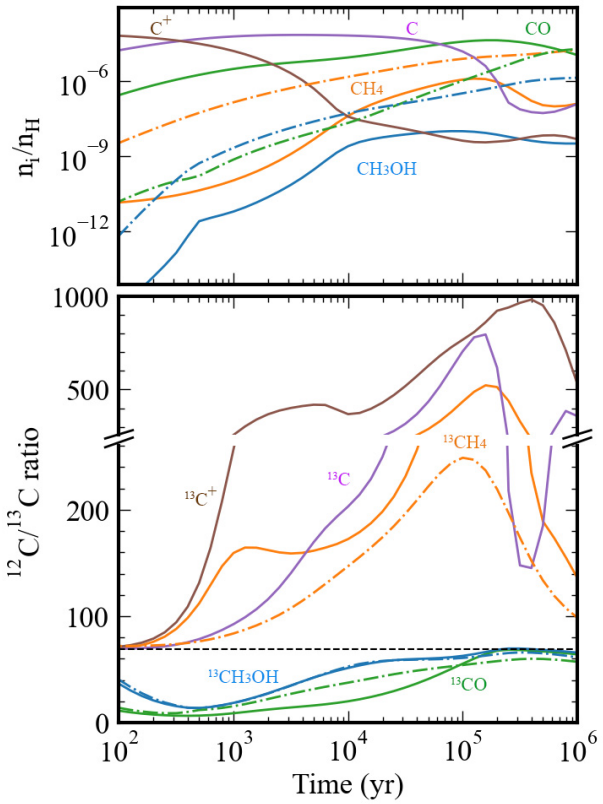

Figure 3.1: Temporal variation of the molecular abundances and $^{12}C/^{13}C$ ratios for gaseous species (solid lines), the bulk (surface + mantle) ice (dash-dot lines) during the static phase. The horizontal black dashed line represents the elemental $^{12}C/^{13}C$ ratio. A broken y-axis is used in the lower panel to show both the moderate ratios of some species (e.g., CO and CH_3OH) and the very high ratios of other species (e.g., C^+ and CH_4).

the $^{12}C/^{13}C$ ratios of these precursors reflect those of the parent ice species. For instance, CH_3 radicals are formed from ^{13}C-poor CH_4 and atomic C, while CH_2OH and CH_3O originate from ^{13}C-rich CH_3OH and CO. Different carbon atoms within the same molecule can exhibit distinct isotope compositions when two precursors have different $^{12}C/^{13}C$ ratios. The isotope ratios of selected COMs are listed in Table3.2.

Figure 3.3 presents the abundance ratios of two ^{13}C isotopomers (e.g., $^{13}CH_3CHO/CH_3^{13}CHO$), reflecting isotopomer-specific fractionation within functional groups. If the abundance ratio is unity, it means there is no difference in the abundances of the isotopomers. Although the ratio for some COMs starts to deviate from unity around 10^4 years, the ratio at later times ($\geq 10^5$ yr) is more important as COMs abundances rise. Notably, CH_3CHO exhibits a persistent

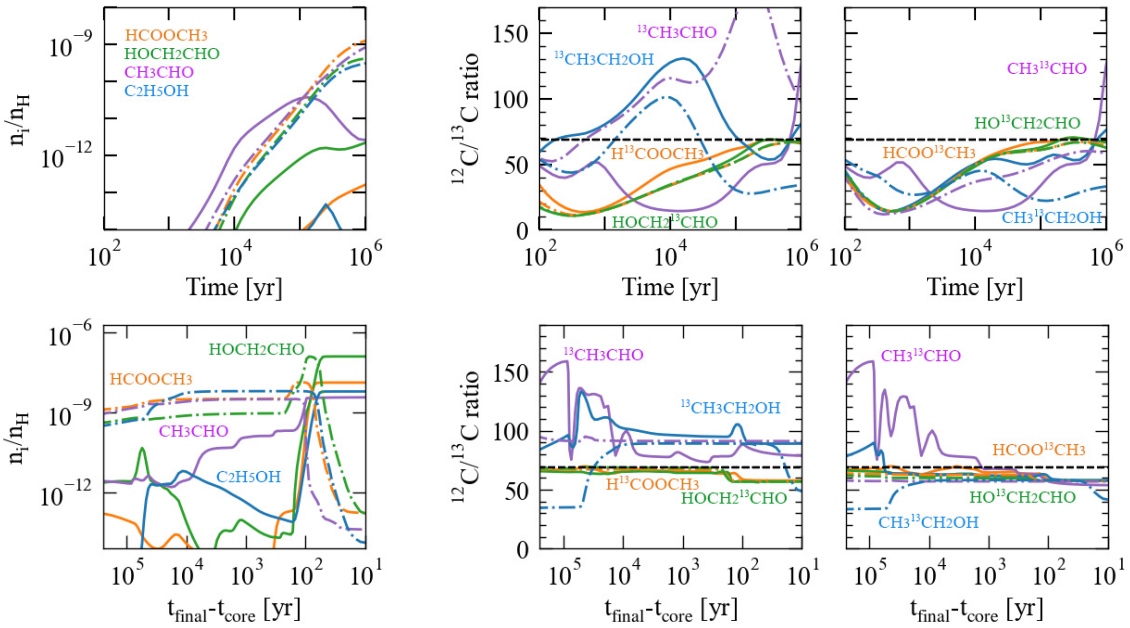

Figure 3.2: Temporal variation of the abundances (left panels) and $^{12}C/^{13}C$ ratios (middle and right panels) of selected COMs in the gas phase (solid lines) and in the bulk (surface + mantle) ice (dash-dotted lines) during the static phase (upper panels) and the collapse phase (lower panels). The middle panels show $^{12}C/^{13}C$ ratios for $H^{13}COOCH_3$, $HOCH_2{}^{13}CHO$, $^{13}CH_3CHO$, and $^{13}CH_3CH_2OH$, while the right panels show those for $HCOO^{13}CH_3$, $HO^{13}CH_2CHO$, $CH_3{}^{13}CHO$, and $CH_3{}^{13}CH_2OH$. The vertical axis is shared between the middle and right panels, and the horizontal black dashed line represents the elemental $^{12}C/^{13}C$ ratio.

Table 3.2:: Abundances and $^{12}C/^{13}C$ ratios of selected COMs during the static and collapse phases. For the static phase, values are taken at 10^6 yr for bulk (surface + mantle) ice. For the collapse phase, values correspond to gas after thermal desorption.

Species	**Abundance** (n_i/n_H)	$^{12}C/^{13}C$ **(isotopomer 1)**	$^{12}C/^{13}C$ **(isotopomer 2)**
Static phase at 10^6 **yr (bulk ice: surface + mantle)**			
$HCOOCH_3$ (ice)	1.2×10^{-9}	66 ($H^{13}COOCH_3$)	63 ($HCOO^{13}CH_3$)
$HOCH_2CHO$ (ice)	4.0×10^{-10}	66 ($HOCH_2{}^{13}CHO$)	61 ($HO^{13}CH_2CHO$)
CH_3CHO (ice)	8.1×10^{-10}	97 ($^{13}CH_3CHO$)	57 ($CH_3{}^{13}CHO$)
C_2H_5OH (ice)	3.0×10^{-10}	34 ($^{13}CH_3CH_2OH$)	32 ($CH_3{}^{13}CH_2OH$)
Collapse phase (gas after thermal desorption)			
$HCOOCH_3$	1.3×10^{-8}	57 ($H^{13}COOCH_3$)	57 ($HCOO^{13}CH_3$)
$HOCH_2CHO$	1.2×10^{-7}	57 ($HOCH_2{}^{13}CHO$)	56 ($HO^{13}CH_2CHO$)
CH_3CHO	3.7×10^{-9}	79 ($^{13}CH_3CHO$)	53 ($CH_3{}^{13}CHO$)
C_2H_5OH	6.1×10^{-9}	89 ($^{13}CH_3CH_2OH$)	57 ($CH_3{}^{13}CH_2OH$)

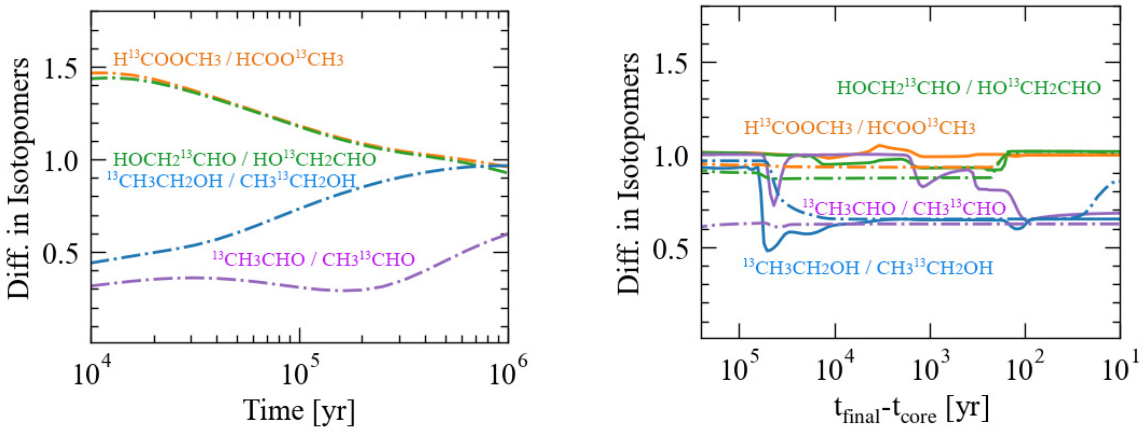

Figure 3.3: Temporal variation of the abundance ratio of isotopomers in the gas phase (solid lines) and in the bulk (surface + mantle) ice (dash-dot lines) during the static phase (left panel) and the collapse phase (right panel). The isotopomer ratios shown are $H^{13}COOCH_3/HCOO^{13}CH_3$, $HOCH_2{}^{13}CHO/HO^{13}CH_2CHO$, $^{13}CH_3CHO/CH_3{}^{13}CHO$, and $^{13}CH_3CH_2OH/CH_3{}^{13}CH_2OH$.

isotopomeric difference throughout the static phase, in contrast to other COMs where such differences are transient and diminish after 10^5 years. This enduring distinction in CH_3CHO isotopomer ratio arises from its formation pathway: the methyl group is primarily derived from ^{13}C-poor CH_4, whereas the formyl group (-CHO) comes from ^{13}C-rich CO.

In contrast, ethanol (C_2H_5OH) does not retain isotopomer-specific fractionation at 10^6 years. Instead, both carbon atoms in the ethyl group become increasingly ^{13}C-rich over time. Initially, CH_3 is derived from ^{13}C-poor CH_4, and CH_2OH is formed from ^{13}C-rich CH_3OH, yielding some isotopomer-specific fractionation. However, as the contribution from reactions involving C_2H_5 radicals and OH radicals becomes dominant, both carbon atoms in the ethyl group inherit similar levels of ^{13}C enrichment. In particular, C_2H_5 originates from C_2, which is formed from ^{13}C-rich C_3, so the isotopic signature of C_3 propagates into larger carbon-bearing species. Because isotope exchange reactions are included between atomic C and C_3 in the present network, whereas analogous exchange reactions for larger carbon chains are not treated, C_3 effectively serves as the main multi-carbon mediator of carbon isotope signatures. As a result, once C_3 becomes enriched in ^{13}C, its isotopic imprint is efficiently transferred to downstream species such as C_2H_5OH. This leads to an overall ^{13}C-rich ethyl group and the disappearance of isotopomeric differences.

Regarding methyl formate ($HCOOCH_3$) and glycolaldehyde ($HOCH_2CHO$), these COMs also show a transient isotopomeric difference, with a noticeable

divergence appearing around 10^4 years but diminishing by 10^5 years. This is attributed to the combination of ^{13}C-rich CH_3O and ^{13}C-poor HCO radicals, which are derived from CH_3OH and H_2CO, respectively. The ^{13}C depletion in H_2CO originates from the insertion of ^{13}C-poor atomic carbon into H_2O ice, leading to the formation of H_2CO. As the relative contribution of CH_3OH increases with time and the overall isotope ratios approach the ISM value, the isotopomer difference becomes less pronounced.

These results emphasize that isotopomer-resolved $^{12}C/^{13}C$ ratios provide crucial insights not only into the molecular formation at each moment, but also into the longer-term chemical evolution and precursor supply that governs the isotopic structure of COMs during their formation.

3.3.2 Collpase Phase

Lower panels of Figure 3.2 show the resulting evolution in COMs abundances and their $^{12}C/^{13}C$ ratios under the collapse phase. When the dust temperature exceeds 20 K, thermal diffusion enables radical–radical reactions to occur efficiently on grain surfaces, potentially becoming a significant or even dominant pathway for COMs formation, depending on the mobility of reactants. This surface-induced chemistry gradually competes with, and in some cases supplements, COMs formation in the ice mantle. This contrasts with the static phase, where COMs mainly form via suprathermal reactions in the ice mantle. When thermal diffusion dominates COMs formation, the carbon isotopic composition increasingly reflects the isotopic origins of individual surface radicals. Among the radicals produced via photodissociation of major ice components, CH_3 radicals, which are ^{13}C-poor due to their origin in CH_4 gas, play a particularly important role because their low binding energy (1600 K) enables efficient diffusion on grain surfaces even at $\sim$20 K. These mobile CH_3 radicals readily react with ^{13}C-rich partners such as CH_2OH, CH_3O, and HCO, leading to the formation of COMs like C_2H_5OH. The isotope ratios of selected COMs are listed in Table3.2.

Figure 3.3 presents the abundance ratios of two ^{13}C isotopomers. C_2H_5OH serves as a representative example of isotopomer-specific evolution. At the end of the static phase, C_2H_5OH exhibits no significant isotopomer difference. However, after the protostar formation and CH_3 begins to diffuse and participate in surface chemistry, an isotopomer difference emerges. The methyl group in newly formed C_2H_5OH turns into ^{13}C-poor due to its CH_4 gas origin, while the CH_2OH group is ^{13}C-rich, reflecting the ^{13}C-rich CH_3OH. This results in a divergence in $^{12}C/^{13}C$ ratios between the two carbon positions, which is seen in the thermally desorbed

C_2H_5OH. The duration and efficiency of this diffusion-induced surface formation depend on the binding energy of the produced COMs. C_2H_5OH, with a relatively high binding energy (4680 K), continues to form and accumulate until temperatures approach ∼90 K. At that point, its abundance formed via surface diffusion exceeds that formed through non-diffusive processes in the ice mantle, and the collapse-phase chemistry largely determines its isotopic ratios.

In contrast, CH_3CHO maintains a persistent isotopomeric difference until the end of our simulations. The methyl group originates from ^{13}C-poor CH_4 or atomic carbon, while the formyl group is formed from slightly ^{13}C-rich CH_3OH. Surface formation of CH_3CHO remains limited during the collapse phase due to competing hydrogen abstraction reactions from CH_3CHO by other radicals (e.g., OH radical or H). Therefore, the isotopomeric ratio established during the static phase is almost preserved.

Other COMs, such as $HCOOCH_3$ and $HOCH_2CHO$, exhibit transient isotopomer differences. These species are primarily formed in the ice mantle from combinations of ^{13}C-rich CH_3OH-derived radicals (e.g., CH_3O, CH_2OH, and HCO). However, in the collapse phase, their surface formation is suppressed due to CO desorption and the activation energy barrier of key reactions (e.g., $CH_3O + CO \rightarrow CH_3OCO$ + 2500 K) and the subsequent hydrogenation. Consequently, the isotopomer differences established in the static phase tend to persist in the mantle and are reflected in the thermally desorbed COMs. Alternative radical–radical pathways involving HCO are possible, as HCO exhibits moderate mobility (E_{bind} 2280 K). However, its contribution is limited by competing hydrogen abstraction reactions involving atomic oxygen or other HCO radicals. As a result, surface production of formyl-bearing COMs remains low, and no new isotopomer difference is introduced.

Meanwhile, suprathermal-radical chemistry continues in the ice mantle, largely insulated from thermal diffusion processes inside the ice mantles due to the binding energies (5700 K) of species trapped in water ice. Here, radicals retain the $^{12}C/^{13}C$ signatures established during the static phase. For example, both functional groups in $HCOOCH_3$ and $HOCH_2CHO$ are formed from slightly ^{13}C-rich CH_3OH and CO, resulting in little or no isotopomer difference.

When the temperature reaches the sublimation temperature of water ice (∼115 K (Garrod & Herbst 2006)), these COMs are released into the gas phase together with water. Thus, the evolution of isotopomer difference during the collapse phase depends on both the mobility and isotopic composition of precursor radicals, and whether surface or mantle chemistry dominates the formation of each COM. If surface formation remains inefficient, the desorbed COMs will retain

their mantle-like isotopic ratios, which are established in the static phase. This preservation emphasizes the importance of early chemical histories in shaping the isotopic characteristics of COMs in protostellar environments where ices have sublimated.

3.4 Discussion

3.4.1 Dependence on the Initial Condition of Carbon

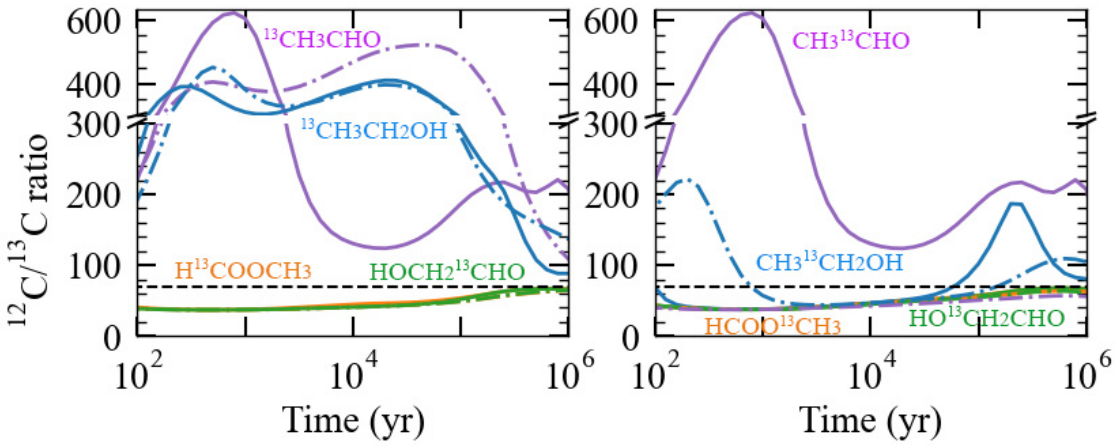

Figure 3.4: Temporal variation of the $^{12}C/^{13}C$ ratios of selected COMs in the gas phase (solid lines) and in the bulk (surface + mantle) ice (dash-dotted lines) during the static phase, in a model where half of the initial carbon is present as CO and the other half as C^+.

We assume that all carbon atoms are initially present as ionized carbon (C^+). To assess the impact of this assumption, we perform additional simulations throughout both the static and collapse phases, in which half of the initial carbon is present as CO, and the other half as C^+. In this case, the isotope exchange reaction $^{13}C^+ + CO \rightleftharpoons C^+ + {}^{13}CO + 35$ K proceeds from the beginning of the simulation.

Figure 3.4 presents the resulting evolution in the $^{12}C/^{13}C$ ratios of certain COMs during the static phase. The influence of the initial carbon condition on the $^{12}C/^{13}C$ ratios and isotopomer differences in COMs depends on their formation timescales. For COMs (e.g., $HCOOCH_3$) that primarily form after $\sim 10^5$ years—around the CO depletion timescale—the impact of the initial carbon condition is negligible. After this point, the efficiency of isotope exchange reactions decreases, and only a minor fractionation in gas-phase species is transferred to COMs via subsequent ice

chemistry. As a result, the initial isotope fractionation of carbon-bearing species has little effect on their final $^{12}C/^{13}C$ ratios or isotopomer distributions.

In contrast, COMs (e.g., C_2H_5OH) that partially form before $\sim 10^5$ years are significantly affected by the initial carbon condition. Because CO ice is still scarce prior to significant depletion, CO-based ice chemistry plays a limited role in early COM formation. As a result, early-forming COMs are mainly derived from gas-phase precursors that retain the imprint of early isotope fractionation processes. Consequently, their $^{12}C/^{13}C$ ratios and isotopomer distributions reflect the initial C^+/CO ratio. For example, C_2H_5OH forms in the ice from C_2H_5, which in turn inherits the carbon isotope composition of gas-phase C_3. When half of the carbon is initially in CO, the reduced abundance of atomic carbon suppresses the isotope exchange reactions between C and C_3, which would otherwise enrich C_3 in ^{13}C. As a result, C_3 is mainly formed from the remaining atomic carbon with a relatively high $^{12}C/^{13}C$ ratio, leading to an overall increase in the $^{12}C/^{13}C$ ratio of C_3 and its derivatives. As a result, the $^{12}C/^{13}C$ ratios in C_2H_5OH isotopomers in the ice phase increase, reaching values of ∼142 for $C_2H_5OH/^{13}CH_3CH_2OH$ and ∼107 for $C_2H_5OH/CH_3{}^{13}CH_2OH$ at 10^6 years. These elevated ratios are slightly preserved after thermal desorption during the collapse phase, particularly if thermal diffusion reactions are inefficient. For instance, the $^{12}C/^{13}C$ ratios remain as high as ∼114 for $C_2H_5OH/^{13}CH_3CH_2OH$ and ∼63 for $C_2H_5OH/CH_3{}^{13}CH_2OH$ in the gas phase after water ice sublimation. These findings highlight the importance of considering the initial carbon reservoir when interpreting carbon isotope ratios in COMs, particularly for species that form early in cold star-forming environments. However, a static (pseudo–time-dependent) treatment cannot capture the coupled evolution of the C/CO partitioning with the changing physical conditions during collapse. In reality, the balance between atomic carbon and CO is regulated by the simultaneous evolution of density, shielding, and freeze-out, which requires a dynamically evolving model.

3.4.2 Comparison to the Full-Scrambling Model

In most of the previous astrochemical models, such as Chaper 2, the full-scrambling was assumed, and all carbon atoms within a molecule are treated as chemically equivalent. This approach simplifies the construction of a chemical network with ^{13}C species but prohibits the study of the isotopomer-specific carbon isotope ratio of COMs.

In contrast, our position-conserved model tracks the position of each carbon atom in molecules through chemical reactions. This allows us to study the

isotopomer-specific $^{12}C/^{13}C$ ratios of COMs in star-forming cores using astrochemical kinetic models for the first time. In this framework, isotopomers of a given molecule can exhibit different abundances if their respective carbon atoms are derived from chemically distinct reservoirs, as mentioned in Section 3.3

While we confirmed that the average of the $^{12}C/^{13}C$ ratios (e.g., $2\times[CH_3CHO]/([^{13}CH_3CHO]+[CH_3{}^{13}CHO])$) is identical between the position-conserved model and the full-scrambling model, the latter model fails to capture the internal isotopomer distribution within molecules. Our results demonstrate that position-specific isotope modeling is essential for interpreting observations that resolve ^{13}C substitutions at different molecular sites, and for identifying formation pathways of COMs based on their isotopic structure.

3.4.3 Isotopomer Differences in COMs Governed by the $^{12}C/^{13}C$ Ratios of Precursor Molecules

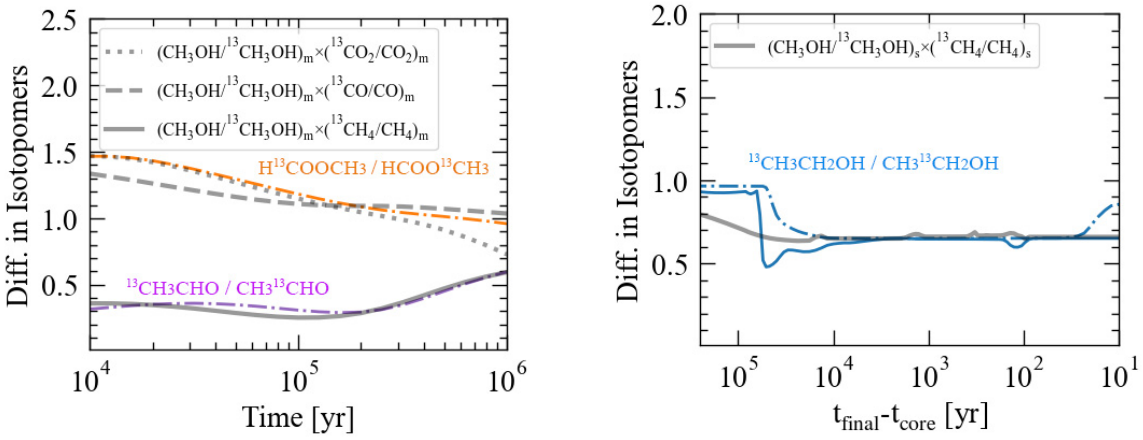

Figure 3.5: Temporal variation of the isotopomer differences during the static phase (left panel) and the collapse phase (right panel). In the left panel, the orange and purple lines represent $HCOOCH_3$ and CH_3CHO, respectively, which correspond to the same quantities as the left panel in Figure 3.3. The dotted, dashed, and solid gray lines represent $(CH_3OH/^{13}CH_3OH)_m\times(^{13}CO_2/CO_2)_m$, $(CH_3OH/^{13}CH_3OH)_m\times(^{13}CO/CO)_m$, and $(CH_3OH/^{13}CH_3OH)_m\times(^{13}CH_4/CH_4)_m$ in the ice mantle, respectively ("m" denotes the ice mantle). In the right panel, the solid and dash-dotted blue lines represent the isotopomer differences of C_2H_5OH in the gas phase and in the bulk (surface + mantle) ice, respectively, corresponding to the right panel in Figure 3.3. The gray line represents $(CH_3OH/^{13}CH_3OH)_s\times(^{13}CH_4/CH_4)_s$ in the ice surface ("s" denotes the ice surface).

In cold environments where thermal diffusion is inefficient, COMs primarily form within the ice mantle through non-thermal processes involving suprathermal species. In this regime, the $^{12}C/^{13}C$ ratios of COMs and, in particular, their isotopomer-specific differences reflect the isotopic composition of their precursor radicals at the time of formation.

Figure 3.5 shows the abundance ratio of ^{13}C isotopomers for CH_3CHO and $HCOOCH_3$ in the bulk ice during the static phase. These isotopomer ratios are compared against products of precursor isotope ratios such as $(CH_3OH/^{13}CH_3OH)_m \times (^{13}CO/CO)_m$ and $(CH_3OH/^{13}CH_3OH)_m \times (^{13}CO_2/CO_2)_m$, where the subscript $_m$ indicates the abundance ratio in the ice mantle. These products represent the expected isotopomer ratios based on the $^{12}C/^{13}C$ ratios of precursor species involved in two-body formation reactions. Before the depletion of gas-phase CO, ^{13}C-poor atomic carbon contributes to CH_3OH formation via the ER reaction of gas-phase atomic carbon with H_2O ice and subsequent hydrogenation. Then CO_2 is more enriched in ^{13}C than CH_3OH, although both molecules primarily are formed from CO. As a result, both $(CH_3OH/^{13}CH_3OH)_m \times (^{13}CO_2/CO_2)_m$ and $(CH_3OH/^{13}CH_3OH)_m \times (^{13}CO/CO)_m$ are different from unity. In this case, the isotopomer difference of COMs could be significant even though both reactants of COMs are enriched in ^{13}C. However, when the hydrogenation of CO becomes the main formation pathway of CH_3OH due to the freeze-out of gas-phase CO, CO and CH_3OH have almost the same $^{12}C/^{13}C$ ratio and $(CH_3OH/^{13}CH_3OH)_m \times (^{13}CO/CO)_m$ get close to unity.

$HCOOCH_3$ is formed from only ^{13}C-rich reactants. Before the freeze-out of gas-phase CO, $HCOOCH_3$ is formed from the suprathermal CO, which is formed from CO_2 via radiolysis. As a result the isotopomer difference of $HCOOCH_3$ is overlapped on the $(CH_3OH/^{13}CH_3OH)_m \times (^{13}CO_2/CO_2)_m$. After that, the formation of CH_3OH is dominated by the hydrogenation of CO, leading to $HCOOCH_3$ formation through CH_3OH and CO, and the isotopomer difference of $HCOOCH_3$ gets close to $(CH_3OH/^{13}CH_3OH)_m \times (^{13}CO/CO)_m$.

CH_3CHO is formed from CH_3 and HCO radicals. While HCO is ^{13}C-rich, CH_3 originates from both CH_4 and CH_3OH. In the early static phase, suprathermal CH_3 is mainly produced from CH_4, which is synthesized from ^{13}C-poor atomic carbon. As a result, CH_3 retains a high $^{12}C/^{13}C$ ratio. As the static phase progresses and CH_3OH abundance increases via hydrogenation of CO, radiolysis of CH_3OH begins to supply ^{13}C-rich CH_3. The methyl group in CH_3CHO thus reflects a combination of these two sources. Consequently, the isotopomer ratio of CH_3CHO gradually approaches unity over time but remains lower than unity.

Thermal diffusion of radicals on grain surfaces also plays a role in setting the isotopomer ratios of COMs as well as radiolysis-induced two-body reactions in the ice mantle. Because radical–radical reactions proceed rapidly once the temperature reaches high enough for the diffusion of one of the reactants, the relative mobility of each radical may affect which formation pathways dominate. Figure 3.5 illustrates the abundance ratio of ^{13}C isotopomers of C_2H_5OH together with the $^{12}C/^{13}C$ ratios of its precursors (CH_4 and CH_3OH) in the ice surface during the collapse phase. The isotopomeric difference directly traces the isotope compositions of CH_3 and CH_2OH radicals, which are primarily formed from ^{13}C-poor CH_4 and ^{13}C-rich CH_3OH, respectively. As such, the abundance ratio of $^{13}CH_3CH_2OH/CH_3{}^{13}CH_2OH$ closely follows the $(^{13}CH_3OH/CH_3OH)_s \times (CH_4/^{13}CH_4)_s$, where the subscript $_s$ indicates the abundance ratio on the ice surface.

3.4.4 Effects of Thermal Radical Diffusion

The radical-radical reaction on the warm ice surface has little to no activation energy, making the reaction rate primarily controlled by the diffusion rate of the radical reactant (Enrique-Romero et al. 2022). However, radicals are highly reactive, making it challenging to determine their diffusion activation energies accurately (Miyazaki et al. 2022). Additionally, the binding energy could also depend on the properties of the surface or the distribution of adsorption sites. To examine how uncertainties in radical mobility affect isotopomer ratios, we varied the diffusion energy ($E_{\rm diff}$) from 0.4 to 0.6 times the binding energy ($E_{\rm bind}$) for key radicals: CH_3, HCO, NH_2, and OH. These species are crucial intermediates in COMs formation and are produced from abundant ice components. Figure 3.6 shows the impact of the radical mobility on the abundance and the isotopomer-specific $^{12}C/^{13}C$ ratio of C_2H_5OH. The increased diffusion activation energies suppress the formation of C_2H_5OH on the surface, reducing the contribution of the diffusive radical-radical reactions on the surface to the overall formation of C_2H_5OH. Consequently, the isotopomer ratio $^{13}CH_3CH_2OH/CH_3{}^{13}CH_2OH$ increases to 0.95 in the evaporated gas at the end of the simulation. Both isotopomers are enriched in ^{13}C, with $^{12}C/^{13}C$ ratios of 36 for $^{13}CH_3CH_2OH$ and 35 for $CH_3{}^{13}CH_2OH$, respectively, where these values are comparable to those seen in the static phase.

These results underscore that isotopomer-resolved carbon isotope ratios reflect the formation pathway of COMs. When radical diffusion is efficient, surface formation pathways dominate, and the isotopic compositions of individual functional groups reflect the isotopic signatures of the radicals involved, especially CH_3, which often retains the ^{13}C-poor character of its CH_4 precursor. In contrast, when the

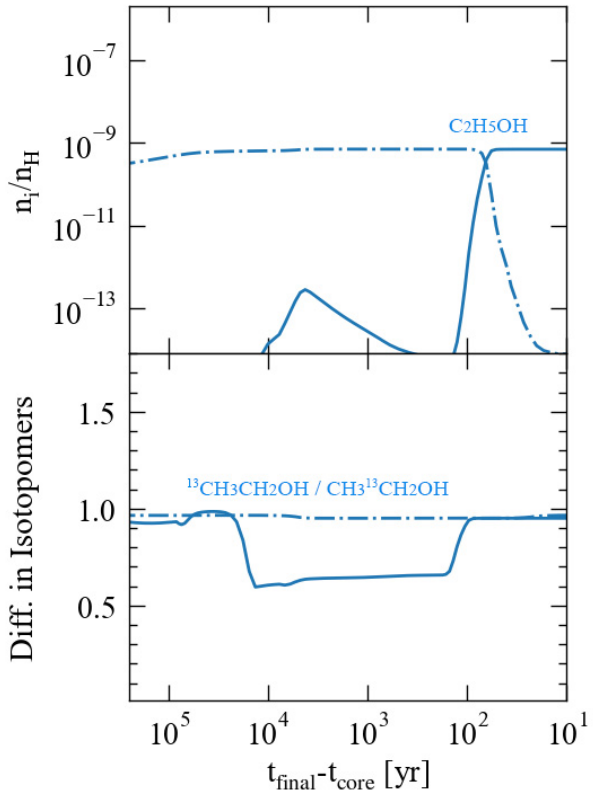

Figure 3.6: Temporal variation of the abundance (upper panel) and isotopomer differences (lower panel) of C_2H_5OH gas (solid blue line) and bulk (surface + mantle) ice (dash-dotted blue line). A lower panel is similar to the right panel in Figure 3.5, but using $E_{\rm diff} = 0.6 \times E_{\rm bind}$ for selected radicals: CH_3, HCO, NH_2, and OH.

activation energy of radical diffusion is high and diffusion is limited, the formation of COMs on the surface becomes inefficient. This enhances the relative contribution from the ice mantle, where suprathermal-radical reactions dominate, and the carbon isotope ratios of both positions often converge due to a common origin in dominant ice species (see Sect 3.3.1). As a result, the isotopomeric differences in the desorbed products diminish, and the $^{12}C/^{13}C$ ratios approach mantle-like values, which are typically more ^{13}C-enriched but less positionally differentiated.

Given the uncertainty in diffusion activation energies of radicals, isotopomer-specific $^{12}C/^{13}C$ ratios of COMs may serve as a useful diagnostic for assessing the relative contributions of surface versus bulk chemistry in astrochemical environments. And given the increasing availability of high-resolution isotopic observations, future laboratory measurements and quantum chemical calculations of radical diffusion energies will be essential for interpreting these isotopic signatures in the context of COMs formation pathways.

3.4.5 Comparisons with Observations

We compare our modeling results with observational data from the ALMA-PILS survey of IRAS 16293-2422B (Jørgensen et al. 2016, 2018). In these observations, the $^{12}C/^{13}C$ ratios for the two ^{13}C isotopomers of C_2H_5OH and CH_3CHO appear nearly identical. However, the reported uncertainties in the $^{12}C/^{13}C$ ratio are as high as 30 %, making it difficult to draw any definitive conclusions about isotopomeric differences. Such potential differences may be entirely obscured by the current measurement limitations.

In contrast, our model predicts a clear isotopomeric difference in the $^{12}C/^{13}C$ ratios of thermally desorbed C_2H_5OH. This difference originates from the thermal diffusion reactions occurring during the collapse phase, which imprint distinct isotope signatures on the methyl and ethyl functional groups. However, if C_2H_5OH forms primarily in the ice mantle or under cold conditions, the isotopomeric difference is suppressed, as discussed in Section 3.4.4. In that case, the $^{12}C/^{13}C$ ratio of C_2H_5OH can become as low as ∼35, consistent with the observed gas-phase value of 41±12. However, the static model alone cannot reproduce the observed gas-phase abundance, even when radiolysis chemistry is included, suggesting that additional non-diffusive formation pathways, such as those proposed by Jin & Garrod (2020), may be required to enhance ethanol production under cold conditions.

Thermally desorbed CH_3CHO in our model also shows a persistent isotopomeric difference in both the static and collapse phases, again differing from the observations. However, this discrepancy may be resolved if a significant fraction of CH_3CHO originates from gas-phase carbon chain species with two indistinguishable carbon atoms, such as C_2H_3 and C_2H_5 (see Section 3.3.1). These species react with atomic oxygen in the gas phase, forming CH_2CO and CH_3CHO, respectively. Moreover, CH_2CO ice could form CH_3CHO ice via successive hydrogenation (Fedoseev et al. 2022; Ferrero et al. 2023; Ibrahim et al. 2024).

Additionally, we compare our results of $^{13}CH_3CN/CH_3{}^{13}CN$ with that of the observations of Class 0/I protostellar systems obtained as part of the PRODIGE (PROtostars & DIsks: Global Evolution) large program (Busch et al. 2025). The $^{12}C/^{13}C$ ratios for the two ^{13}C isotopomers of CH_3CN are enriched in ^{13}C compared to the ISM value regardless of the source. In contrast, our model predicts an isotopomer-specific fractionation in thermally desorbed CH_3CN: $CH_3CN/^{13}CH_3CN$ ∼38 and $CH_3CN/CH_3{}^{13}CN$ ∼102 (see lower panels in Figure 3.7), which reflect the $^{12}C/^{13}C$ ratios of CH_3CN ice formed during the static phase. Upper panels in Figure 3.7 show the temporal evolution of the abundances and $^{12}C/^{13}C$ ratios of CH_3CN in the gas and ice phases during the static phase. Prior to 10^5 years, the

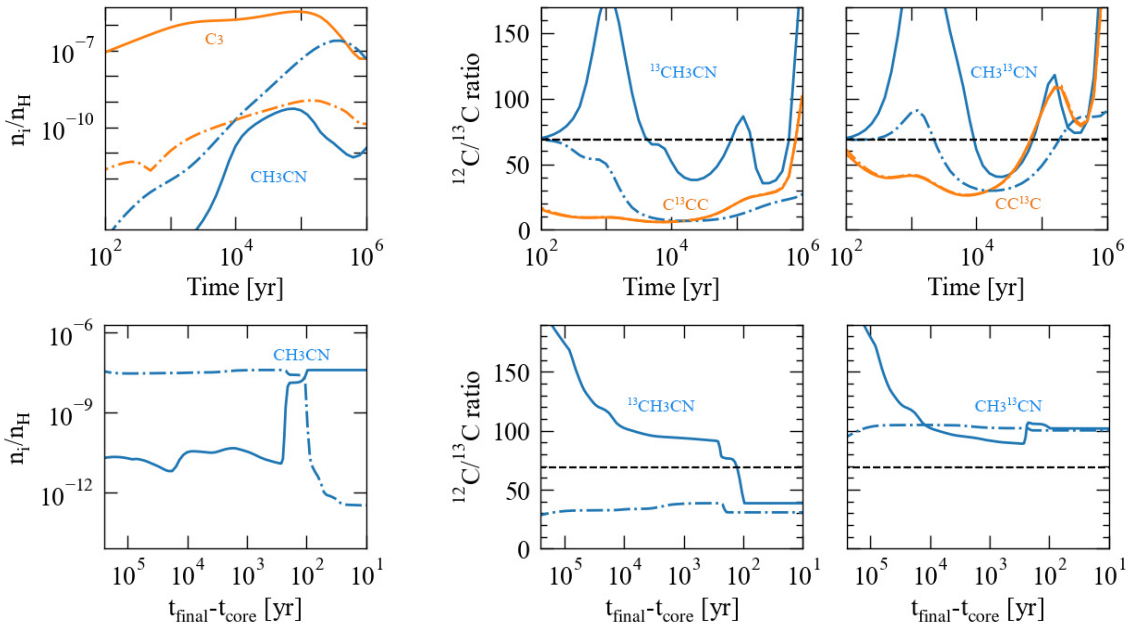

Figure 3.7: Temporal variation of the abundances (left panels) and $^{12}C/^{13}C$ ratios (middle and right panels) of CH_3CN in the gas phase (solid lines) and bulk (surface + mantle) ice (dash-dotted lines) during the static phase (upper panels) and the collapse phase (lower panels). In the upper panels, the results for C_3 are also shown for comparison. The $^{12}C/^{13}C$ ratios of $C^{13}CC$ and $CC^{13}C$ in the gas and ice phases are nearly identical, respectively.

^{13}C isotopomers of CH_3CN ice are initially enriched in ^{13}C, but their $^{12}C/^{13}C$ ratios gradually increase over time. This trend reflects the formation pathway of CH_3CN ice, which originates from the dissociation of C_2H_5CN ice during the static phase. The precursor molecule C_2H_5CN is formed via the reaction of atomic nitrogen with C_3, followed by successive hydrogenation on the ice. Consequently, the carbon isotope ratios in CH_3CN inherit those of C_3. The $^{12}C/^{13}C$ ratio of C_3 gas is primarily shaped by three isotope exchange reactions: $^{13}C + C_3 \rightleftharpoons C + C_2{}^{13}C + 27$ K, $^{13}C + C_3 \rightleftharpoons C + C^{13}CC + 43$ K, and $C + C_2{}^{13}C \rightleftharpoons C + C^{13}CC + 16$ K. Because C_3 is symmetric with equivalent terminal carbon atoms, $^{13}CC_2$ and $C_2{}^{13}C$ are physically indistinguishable and are treated as a single isotopomer. As the efficiencies of the isotope exchange reactions decrease over time, C_3 increasingly forms from atomic carbon that is relatively ^{13}C-poor. This results in a gradual increase in the $^{12}C/^{13}C$ ratio of C_3. Furthermore, as more atomic carbon becomes locked in CO, the overall abundance of C_3 diminishes. This reduction in abundance amplifies the extent of isotope fractionation, leading to even higher $^{12}C/^{13}C$ ratios and enhancing the differences between C_3 isotopomers. This isotopic signature in the gas phase is

subsequently transferred to the ice phase. Since atomic nitrogen reacts with the terminal carbon atoms of C_3 in the ice phase, the carbon atom adjacent to nitrogen in CH_3CN becomes more depleted in ^{13}C than the methyl carbon.

The discrepancy between our model and the observations may arise from physical processes during the static phase. A substantial abundance of CH_3CN ice ($\sim 4.4\times10^{-8}$) is already formed by 10^5 years, and these molecules are enriched in ^{13}C ($CH_3CN/^{13}CH_3CN$ ~10, $CH_3CN/CH_3{}^{13}CN$ ~46). If the static phase effectively ends around 10^5 years, this ^{13}C enrichment in CH_3CN ice may be preserved through to the protostellar stage, depending on subsequent thermal and chemical processing. Another possible explanation is the uncertainty in the formation pathways of CH_3CN. While gas-phase reactions involving protonated CH_3CN or surface reactions between CH_3 and CN radicals may influence the $^{12}C/^{13}C$ isotopomer ratios, as discussed by Busch et al. (2025) and Enrique-Romero & Lamberts (2025), their actual contributions remain uncertain.

To better interpret isotopomer-resolved $^{12}C/^{13}C$ ratios and constrain the formation pathways of COMs, further improvements in observational precision, theoretical modeling, and the accuracy of spectroscopic parameters used to derive column densities are essential. As discussed at the beginning of this section, the observed $^{12}C/^{13}C$ ratio of CH_3CHO is ~67, with an uncertainty of about 30% (i.e., 47–87). Our results ($CH_3CHO/^{13}CH_3CHO$ ~80 and $CH_3CHO/CH_3{}^{13}CHO$ ~55) are consistent within these observational errors. To evaluate the observational accuracy required to distinguish isotopomer differences, we estimated the detectable limit using both the relative percent difference (RPD) and error propagation analysis. The RPD is defined as

$$\mathrm{RPD} = \frac{|R_1 - R_2|}{(R_1 + R_2)/2} \times 100\% \tag{3.5}$$

where R_1 and R_2 denote the respective $^{12}C/^{13}C$ ratios of the two isotopomers. Assuming equal relative observational uncertainties for the two isotopomers, the RPD provides a first-order measure of how precise the observations must be to distinguish the isotopomers. In our model, the largest isotopomer difference occurs for CH_3CHO or C_2H_5OH, with $R_1/R_2 \approx 0.65$ ($R_1 \leq R_2$), corresponding to RPD $\approx$ 42%. This indicates that their distinction requires observational uncertainties smaller than roughly half of this value ($\lesssim$20%).

Recent JWST observations of protostellar envelopes (Brunken et al. 2024) have reported solid-state $^{12}C/^{13}C$ ratios for CO and CO_2 ice across a sample of embedded sources. For CO_2 ice, the mean $^{12}CO_2/^{13}CO_2$ ratios derived from the 2.70 μm, 4.27 μm, and 15.2 μm bands observations are 85 ± 23, 76 ± 12, and 97 ± 17, respectively. For CO ice, the sample-averaged $^{12}CO/^{13}CO$ ratio is typically close to $\sim$ 100,

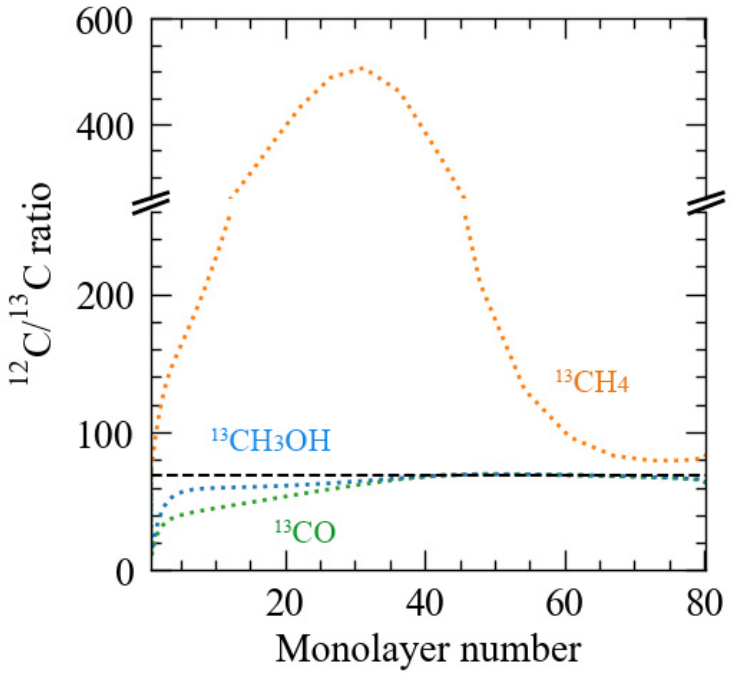

Figure 3.8: Evolution of $^{12}C/^{13}C$ ratios of selected species on the ice surface as a function of the cumulative number of icy layers. The "monolayer number" on the horizontal axis represents the temporal sequence of ice accumulation.

although individual sources show significant scatter depending on the band used. In contrast, our model predicts that CO ice generally inherits a $^{12}C/^{13}C$ ratio close to the elemental value during the prestellar and collapse phases, with only moderate deviations. While the CO_2 ice ratios are broadly consistent with this prediction within uncertainties, the elevated mean $^{12}CO/^{13}CO$ ratios inferred for CO ice are not reproduced. This suggests that additional processes affecting carbon partitioning in protostellar envelopes may not yet be fully captured in the present framework.

3.4.6 Chemically Heterogeneous Ice

Figure 3.8 shows the evolution of the $^{12}C/^{13}C$ ratios of selected carbon-bearing species (e.g., CH_3OH, CO, CH_4) on the ice surface as a function of the number of monolayers accumulated over time. In the three-phase model adopted here, the surface layer is continuously updated as molecules accrete from the gas phase, while previously formed surface material is incorporated into the ice mantle. Note that the mantle phase in this model is not explicitly layered; thus, "monolayer number" should be interpreted as a time-ordered index of ice growth. These results

demonstrate the formation of chemically heterogeneous ice, characterized by vertical stratification in carbon isotope composition.

The $^{12}C/^{13}C$ ratios of surface species generally follow those in the gas phase, as ice growth proceeds through accretion from the gas. Because the gas-phase isotope ratio evolves rapidly, particularly during the early stages due to isotope exchange reactions, the newly accreted surface layers reflect the time-dependent gas-phase conditions. Once CO becomes the dominant carbon-bearing species, the efficiency of exchange reactions declines, resulting in diminished fractionation in the later-deposited surface layers.

In contrast, the ice mantle—composed of earlier surface layers buried over time—is less chemically active and gradually decouples from ongoing gas-phase processes (see dash-dotted lines in Figure 3.1). As a result, it preserves stronger signatures of the early isotope fractionation, producing a vertically stratified $^{12}C/^{13}C$ pattern analogous to that seen in the deuteration study (Taquet et al. 2014) and in the nitrogen isotope fractionation study (Furuya & Aikawa 2018).

This vertical heterogeneity is also seen for species formed by surface hydrogenation, such as CH_3OH. While CH_3OH on the surface inherits the evolving isotope ratio of CO, the mantle CH_3OH retains a more ^{13}C-enriched signature corresponding to early-time CO. Consequently, the carbon isotope ratios of CH_3OH in the mantle differ from those on the surface, even though they share a common formation pathway.

Radiolysis may also contribute to isotopic mixing in the ice mantle. For instance, radiolysis of CO via

$$\mathrm{CO} \rightarrow \mathrm{C}^* + \mathrm{O}^*, \quad \mathrm{C}^* \rightarrow \mathrm{C}, \tag{3.6}$$

can blend ^{13}C-rich and ^{13}C-poor components by converting CO into atomic carbon. However, this process is similar to photodissociation via UV photons induced by cosmic rays or external sources. Our results indicate that for dominant species such as CH_4 and CH_3OH, the effect of radiolysis on $^{12}C/^{13}C$ ratios is minor, as these species primarily form via barrierless or low-barrier reactions independent of suprathermal chemistry.

This stratification in precursor isotope ratios suggests that COMs formed within the ice mantle may inherit analogous isotopic gradients, depending on their formation depths and the temporal evolution of precursors. While our model distinguishes between gas, surface, and mantle phases, it lacks a fully layered treatment of the mantle, and thus cannot capture intra-mantle isotopic variations in COMs formation. To quantitatively evaluate how such vertical isotope gradients

influence the isotopomer-specific $^{12}C/^{13}C$ ratios of COMs, future modeling efforts must incorporate a fully multilayered treatment of ice chemistry.

3.4.7 Implications for Meteoritic Organic Matter

Recent advances in compound- and site-specific isotope analyses of meteoritic amino acids provide an unprecedented opportunity to explore possible genetic links between interstellar organic chemistry and the organic inventory of the early Solar System. At the same time, however, significant uncertainties remain in the interstellar carbon isotope inventory. In the cold interstellar medium, ^{13}C is expected to be preferentially incorporated into CO, potentially depleting the remaining "carbon isotope pool" in ^{13}C. Although observations have revealed ^{13}C depletions in several C-bearing molecules, tentative ^{13}C enrichments in others, such as formaldehyde, appear to contradict theoretical expectations. As emphasized by Aponte et al. (2017), these inconsistencies indicate that isotopic partitioning among interstellar molecules has not yet been demonstrated unequivocally, and that the large observational uncertainties in interstellar $^{12}C/^{13}C$ ratios imply that relying on a single, molecule-independent (bulk) interstellar isotope ratio cannot constrain the origin of meteoritic organics without extensively considering the chemistry and other isotope effects for each molecule present.

In light of these uncertainties, the comparison presented here is deliberate and cautious. The aim is not to construct a fully quantitative model of disk chemistry or parent-body processing, which would require additional ingredients such as detailed protoplanetary disk evolution, radial transport, and heterogeneous alteration histories. Instead, our goal is to place the astrochemical results obtained in this thesis into a broader perspective by comparing them qualitatively and semi-quantitatively with position-specific and isotopomer-resolved carbon isotope measurements of meteoritic organic compounds. The emphasis is on relative, intramolecular isotopic relationships, which are less sensitive to environmental gradients and observational uncertainties than absolute bulk isotope ratios.

Recent site-specific $\delta^{13}C$ measurements of meteoritic amino acids provide a particularly valuable benchmark for evaluating possible links between interstellar chemistry and Solar System organic matter. Here, $\delta^{13}C$ values are reported in the conventional per mil (‰) notation relative to the VPDB standard, for which $^{12}C/^{13}C \simeq 89.4$. For example, alanine in the Murchison meteorite exhibits pronounced intramolecular isotopic heterogeneity (-29 ± 10 ‰ for the carboxyl carbon, $+142 \pm 20$ ‰ for the amine-bound carbon, and -36 ± 20 ‰ for the methyl carbon; Chimiak et al. 2021). These values correspond to $^{12}C/^{13}C$ ratios of approximately

∼92 (carboxyl), ∼78 (amine-bound), and ∼93 (methyl), respectively. Previous meteoritic studies have interpreted this pattern in terms of specific synthetic pathways: in α-amino acids such as alanine, Strecker-type synthesis has been proposed, in which the amine-bearing carbon originates from the carbonyl carbon of aldehydes. If the aldehydes are derived from CO in the interstellar medium, they are expected to carry a ^{13}C-enriched signature, which is then transferred to the amine-bound carbon in the resulting amino acid. In contrast, the methyl carbon in alanine has been linked to a comparatively ^{13}C-depleted carbon pool associated with C^+- or CH_x-dominated chemistry (Elsila et al. 2012; Aponte et al. 2017). Meanwhile, β-alanine has been suggested to form predominantly via Michael addition to acrylonitrile, implying that its isotopic structure may reflect the isotopic properties of nitrile precursors rather than those of CO-derived aldehydes (Chimiak & Eiler 2024).

Our astrochemical modeling provides an independent theoretical perspective on these relationships. In our isotopomer-resolved calculations, aldehyde-bearing functional groups formed from CO ice, such as CH_3CHO, $HCOOCH_3$, and $HOCH_2CHO$, become systematically enriched in ^{13}C by approximately 14–28% relative to the elemental $^{12}C/^{13}C$ ratio. This enrichment originates from the CO reservoir in the cold prestellar phase, with the effect subsequently inherited by molecules formed from CO-derived radicals on grain surfaces or in the mantle. By contrast, our model predicts that acrylonitrile shows only weak ^{13}C fractionation at its terminal carbon, with values remaining close to the elemental ratio throughout the chemical evolution. This contrast reflects the distinct isotopic histories of the CO-derived and C/C^+-related carbon reservoirs in the interstellar medium.

When these results are viewed together, a plausible correspondence emerges between meteoritic isotope patterns and interstellar chemical processes. The strong ^{13}C enrichment predicted for aldehyde-derived carbon sites in our model is qualitatively consistent with the highly ^{13}C-enriched amine-bound carbon observed in α-alanine, if Strecker synthesis involving CO-derived aldehydes indeed dominated its formation. Conversely, the comparatively weak fractionation predicted for acrylonitrile is consistent with the expectation that β-alanine, if synthesized via Michael addition to acrylonitrile, should inherit only modest ^{13}C enrichment at its amine site. In this sense, differences in the degree of ^{13}C enrichment between α- and β-alanine may encode information not only about their formation pathways (Strecker versus Michael addition) but also about the isotopic characteristics of their distinct precursor reservoirs (CO-derived aldehydes versus acrylonitrile).

It is worth noting that the absolute amplitude of intramolecular ^{13}C enrichment observed in meteoritic amino acids is typically smaller—often by up to an order of

magnitude—than the maximum isotopomer-specific fractionation predicted under cold prestellar conditions in our model. This difference is likely general rather than molecule-specific. Large fractionation signatures generated in the interstellar medium may be partially attenuated during subsequent protostellar collapse, disk evolution, radial mixing, and parent-body processing, including thermal and aqueous alteration (e.g., Aponte et al. 2017). Such processes would reduce the magnitude of the original isotopic heterogeneities while potentially preserving their relative intramolecular patterns. Therefore, the comparison presented here does not rely on quantitative agreement in absolute enrichment levels, but instead emphasizes relative position-specific contrasts as the more robust indicator of chemical heritage.

We emphasize, however, that this connection remains interpretative rather than definitive. Galactic-scale gradients in $^{12}C/^{13}C$ ratios, arising from Galactic chemical evolution, the limited precision of many interstellar $^{12}C/^{13}C$ measurements, and the effects of parent-body alteration complicate any direct one-to-one comparison. Nevertheless, the combination of our modeling results and meteoritic observations demonstrates that relative, position-specific isotopic contrasts—between functional groups, molecular sites, and precursor reservoirs—provide a powerful and robust means of evaluating whether meteoritic organics retain an isotopic "memory" of interstellar chemistry.

3.5 Conclusions

We have developed a position-specific isotopic astrochemical model that traces the $^{12}C/^{13}C$ ratios of individual carbon atoms within COMs in interstellar environments. By distinguishing ^{13}C substitution sites, we reveal how isotopomer-specific carbon isotope ratios evolve from prestellar cores to protostellar cores. This work extends our previous model (see Chapter 2), which included multi-carbon COMs but treated all carbon atoms as equivalent, to an isotopomer-specific isotopic model that distinguishes individual ^{13}C substitution sites within each molecule. The main conclusions are as follows:

1. Isotopomer-Specific Carbon Isotope Ratio: COMs can exhibit up to 40% differences in $^{12}C/^{13}C$ ratios between their isotopomers, depending on the isotopic composition of their functional-group precursors. For example, CH_3CHO shows a persistent isotopomer difference between its $^{13}CH_3CHO$ and $CH_3{}^{13}CHO$ forms ($^{13}CH_3CHO$ / $CH_3{}^{13}CHO$ $\sim$0.6), originating from the distinct isotope ratios of CH_4 and CO in the early cold phase. These differences are absent in conventional models assuming complete atomic scrambling.

2. Cold-Phase Isotopic Memory: In the static phase, COMs form primarily in the ice mantle via non-thermal suprathermal reactions in our model. The isotopomeric compositions of COMs reflect the $^{12}C/^{13}C$ ratios of precursors like CH_3OH, CO, and CH_4, which themselves inherit isotope fractionation patterns from earlier gas-phase isotope exchange reactions. This imprint can persist throughout the evolution and remains in thermally desorbed COMs if surface formation is inefficient.

3. Collapse-Phase Surface Chemistry: Diffusion-induced surface chemistry produces new isotopomer differences not present at the end of the static phase. For instance, as dust grains warm, ^{13}C-poor CH_3 radicals diffuse and react with ^{13}C-rich radicals such as CH_2OH, forming $^{13}C_2H_5OH$. Consequently, the $^{13}CH_3CH_2OH$ / $CH_3{}^{13}CH_2OH$ ratio in ice decreases from unity to ∼0.6. This demonstrates that isotopomer differences can be amplified during warm-up through selective surface diffusion.

4. Sensitivity to Diffusion Activation Energy Barriers: A 20% increase in diffusion activation energies reduces the contribution of surface formation and isotopomer differences. For example, $^{13}CH_3CH_2OH$ / $CH_3{}^{13}CH_2OH$ in ice does not change during the collapse phase. Under these conditions, thermally desorbed COMs more strongly reflect the mantle composition, highlighting the need for accurate estimates of radical mobility.

5. Comparison with Observations: Our model reproduces the observed $^{12}C/^{13}C$ ratios of CH_3CHO within the measurement uncertainty (∼67±20, i.e., 47–87), with modeled values of ∼80 and ∼55 for the two isotopomers. For C_2H_5OH, diffusion-driven surface chemistry during the collapse phase produces isotopomeric differences, whereas formation mainly in the ice mantle or under cold conditions suppresses them, yielding a ratio (∼40) consistent with the observed value (41±12, i.e., 28–53). In contrast, CH_3CN shows isotopomer-specific ratios (38 and 102) that differ from the ^{13}C-enriched isotopomers observed in the PRODIGE survey, likely due to the preservation of ^{13}C-rich CH_3CN ice formed during the static phase or the contribution of gas-phase reactions. Future high-sensitivity isotopomer measurements—achieving uncertainties smaller than ≈20% in the derived $^{12}C/^{13}C$ ratios—will be required to distinguish between surface- and mantle-driven formation routes of COMs.

6. Implications and Future Work: This position-specific isotopic modeling demonstrates that isotopomer-resolved $^{12}C/^{13}C$ ratios can preserve information on the chemical origin of COMs from the cold to the warm stages of star

formation. Quantitative comparison with our previous model (see Chapter 2), which does not distinguish positions of carbon isotopes within a molecule, confirms that including isotopomer-specific chemistry refines the distribution of ^{13}C among functional groups without altering the total carbon budget. Further improvements in observational precision and constraints on microphysics on ice chemistry, such as diffusion barriers and ice morphology, will be essential to confirm isotopomer-specific signatures and link isotopic patterns across simple and complex molecules for understanding their formation pathways.

Our study demonstrates that the position-specific carbon isotope ratio of COMs retains a history of their formation processes and environmental effects. By resolving isotopomer differences, we gain access to chemical information that would otherwise be averaged out in conventional isotopic models. This framework offers a promising pathway toward decoding the formation pathways of complex organic molecules in star-forming regions.

Appendix to Chapter 3

A.1 Nitrogen-bearing molecules

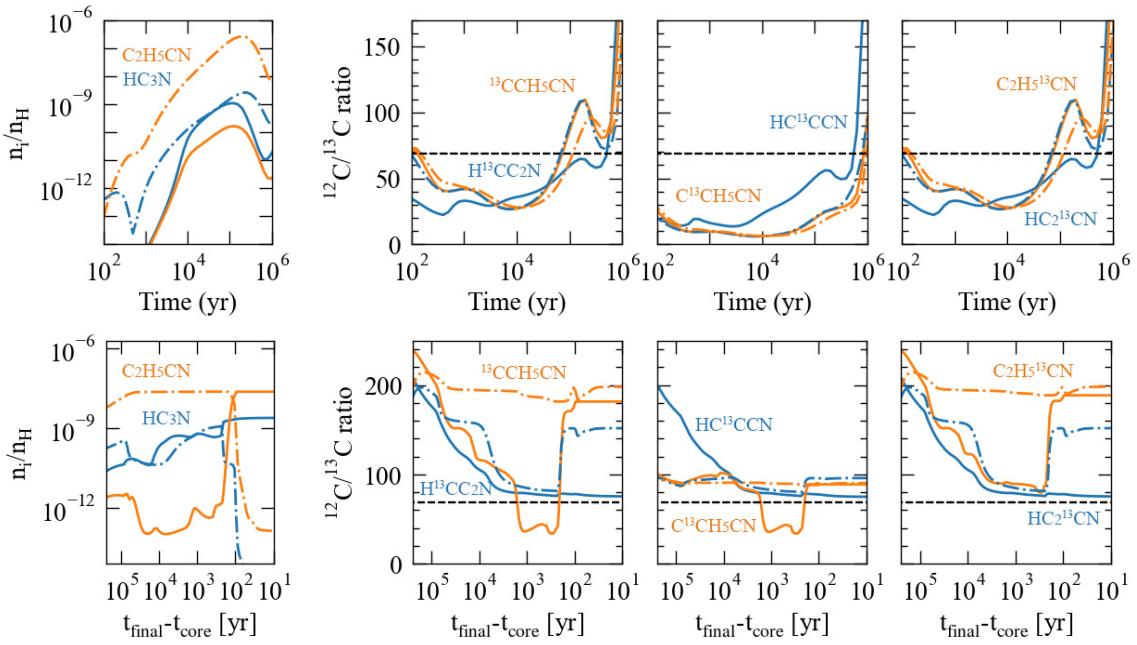

Figure A.1: Temporal variation of the abundances (left panels) and $^{12}C/^{13}C$ ratios (middle and right panels) of HC_3N and C_2H_5CN in the gas phase (solid lines) and bulk (surface + mantle) ice (dash-dotted lines) during the static phase (upper panels) and the collapse phase (lower panels).

Our model predicts isotopomer-specific fractionation in both HC_3N and C_2H_5CN, reflecting their common formation pathway through reactions involving C_3 during the static phase (Figure A.1). Upper panels in Figure A.1 show the temporal evolution of the abundances and $^{12}C/^{13}C$ ratios of HC_3N and C_2H_5CN in the gas and ice phases during the static phase. Both HC_3N ice and C_2H_5CN

ice are primarily formed through reactions of atomic nitrogen with C_3, followed by successive hydrogenation reactions on grain surfaces. Consequently, their carbon isotope compositions closely follow that of C_3. Because isotope exchange reactions between atomic carbon and C_3 enrich C_3 in ^{13}C during the static phase, the isotopic signature of C_3 is directly transferred to these molecules. As a result, the carbon atom located in the central position of the carbon chain becomes more enriched in ^{13}C than the terminal carbon atoms, producing characteristic isotopomer-specific fractionation patterns similar to those of C_3.

During the collapse phase (lower panels in Figure A.1), the isotopic differences among the carbon positions in HC_3N become significantly reduced. In this stage, HC_3N is predominantly formed from precursors whose carbon atoms originate from major ^{13}C-poor species, such as CH_3. As a result, the $^{12}C/^{13}C$ ratios of all carbon positions in HC_3N converge toward values of order $\sim$90, and the isotopomer-specific fractionation largely disappears.

Chapter 4

Summary and Future perspectives

4.1 Summary

This thesis investigates how COMs evolve in star- and planet-forming regions, with a particular focus on carbon isotope signatures as tracers of chemical histories and molecular formation pathways. Motivated by the rapid expansion of high-sensitivity observations of COMs in prestellar cores, protostellar environments, and protoplanetary disks, this work aims to clarify how COMs acquire their isotopic compositions, which chemical pathways dominate under different physical conditions, and whether isotopomer-resolved information can distinguish formation mechanisms that are otherwise degenerate in abundance-only analyses.

To address these goals, astrochemical models were developed that couple time-dependent physical evolution with a three-phase (gas, grain surface, and ice mantle) chemical network, extended to explicitly track the positional distribution of ^{13}C within organic molecules. This isotopomer-resolved framework allows carbon isotope ratios to be evaluated not only at the molecular level but also at the functional-group level, establishing a direct link between molecular formation processes and observable isotopic patterns. By following both abundances and isotope ratios throughout the prestellar, collapsing, and protostellar stages, the results demonstrate that early isotopic signatures are not completely erased during collapse and warm-up, but may be attenuated or redistributed depending on the efficiency of thermal diffusion.

A detailed analysis of the modeled chemical evolution shows that isotope fractionation is strongly pathway-dependent and reflects the isotopic characteristics of precursor reservoirs. Carbon originating from CO, atomic C, or C^+ experiences

different fractionation histories in cold gas and on icy grains, leading to molecule-dependent and environment-dependent isotopic outcomes. Incorporating grain-surface C-atom addition chemistry, supported by recent laboratory findings, reduces excessive fractionation predicted by purely gas-phase processes and yields more realistic $^{12}C/^{13}C$ ratios consistent with observational constraints.

Building on this, an isotopomer-resolved reaction network was constructed to follow the position of ^{13}C within individual molecules, including both thermal diffusion–driven radical chemistry on warm surfaces and non-thermal suprathermal chemistry in cold bulk ice. The results reveal that different carbon sites within a single molecule can maintain distinct $^{12}C/^{13}C$ ratios, reflecting whether formation proceeds through CO-derived fragments, C/C^+-dominated chemistry, surface versus mantle pathways, or thermal versus non-thermal processes. In particular, functional groups associated with CO-derived radicals tend to inherit ^{13}C-enriched signatures originating in the cold prestellar phase, whereas other carbon positions can remain comparatively ^{13}C-poor. These findings demonstrate that position-specific isotope patterns offer a new diagnostic dimension, providing a physically grounded means of discriminating among competing COMs formation scenarios.

Finally, the implications of these results were extended beyond interstellar chemistry to organic matter preserved in Solar System materials. Position-specific and compound-specific isotope measurements of meteoritic amino acids exhibit pronounced intramolecular ^{13}C heterogeneity, which likely encodes information on precursor reservoirs and formation pathways. By comparing such isotopic structures with those predicted by isotopomer-resolved astrochemical models, this thesis explores whether meteoritic organics are consistent with inheritance from interstellar chemistry, while explicitly acknowledging uncertainties arising from observational limitations, disk evolution, and parent-body processing. This connection establishes a conceptual and quantitative bridge between star-forming chemistry and meteoritic records.

Overall, this thesis demonstrates that isotopomer-specific astrochemistry provides a powerful framework for tracing the origin and evolution of organic matter from molecular clouds to planetary building blocks. By integrating dynamical evolution, grain-surface and bulk-ice chemistry, non-thermal processing, and isotopic structure, the work offers testable predictions for forthcoming high-sensitivity ALMA and JWST observations and contributes toward establishing robust isotopic links between the interstellar medium and Solar System materials.

4.2 Future Perspectives

The results presented in this thesis point to several promising directions to advance isotopic astrochemistry toward a comprehensive, observation-tested description of organic evolution from molecular clouds to the Solar System. First, continued progress will rely on tighter integration between isotopomer-resolved modeling and emerging observational capabilities. High spectral- and spatial-resolution surveys with ALMA, together with infrared constraints on ices and organics from JWST, will increasingly enable simultaneous constraints on molecular abundances, excitation conditions, and isotopic ratios across evolutionary stages. Systematic comparisons between modeled isotopomer patterns and multi-source observational samples (from prestellar cores to disks) will be essential to isolate environmental trends and to identify robust isotopic diagnostics that are insensitive to uncertainties in physical structure. A timely example is provided by recent JWST measurements of solid-state $^{12}CO/^{13}CO$ ratios in protostellar envelopes, which in some cases approach or exceed values of order 100. Such elevated ratios are difficult to reproduce through low-temperature ion–molecule exchange reactions alone, which tend to enrich ^{13}CO rather than deplete it. A promising avenue is isotope-selective photodissociation of CO in moderately shielded envelope layers, combined with the layered freeze-out history of CO ice. Incorporating self-shielding, ultraviolet radiative transfer, and explicit ice layering into isotopomer-resolved models will therefore be essential for quantitatively testing the new JWST constraints.

Second, key chemical uncertainties must be reduced to make isotopic predictions quantitatively predictive rather than qualitative. Priority targets include (i) branching ratios and rate coefficients for ice-phase reactions, (ii) atom-addition/abstraction kinetics on ices, and (iii) non-diffusive mechanisms in the mantle that can lock in early-time isotopic signatures. In addition, a major frontier is the incorporation of isotope-dependent surface physics—binding energies, diffusion barriers, and reaction-diffusion competition—derived from laboratory measurements and quantum-chemical calculations. Although Chapter 2 shows that isotope exchange reactions dominate over isotope-dependent adsorption or diffusion effects under the conditions explored here, such physical isotope effects may become more important in multilayer ice models where subtle differences in binding and diffusion can accumulate over long timescales. Exploring this possibility will require models that explicitly resolve ice layering and bulk diffusion.

Third, advancing from “source tracing” to “inheritance tracing” requires connecting chemical evolution to material transport. Disk accretion, vertical turbulent mixing, grain growth, and radial drift of dust grains can redistribute

ices and organics and thereby mix isotopically distinct reservoirs. Incorporating isotopomer chemistry into disk models with transport, together with explicit ice layering and phase transitions, will allow us to test whether isotopic signatures observed in comets and meteorites can be reproduced from physically realistic inheritance-and-processing scenarios. Such models can also clarify which signatures are resilient enough to survive into planetesimals and which are overwritten during episodic heating or irradiation. In this context, a key future challenge is to establish quantitative links between isotopic signatures observed in star- and planet-forming environments and those measured in organic matter preserved in meteorites and comets. Laboratory analyses of meteoritic insoluble and soluble organic matter, as well as isotopic measurements of cometary volatiles, provide complementary records of early Solar System chemistry that can be directly compared with astrochemical model predictions. Isotopomer- and functional-group–specific isotope ratios are particularly promising in this regard, as they can retain information on precursor reservoirs and formation pathways even when bulk isotopic ratios are partially altered by parent-body or nebular processing. Developing a forward-modeling framework that connects interstellar and disk chemistry to the isotopic properties of Solar System materials will be essential for disentangling inheritance from secondary modification.

Finally, the isotopomer-resolved framework developed here can be extended beyond ^{13}C to multi-isotope and multi-element tracers. Joint modeling of ^{13}C with ^{15}N, and D/H—especially when isotopomer-specific information is available—will offer stronger constraints on formation pathways, because different isotopes respond differently to ion-molecule chemistry, photochemistry, and grain-surface processes. A long-term goal is to establish a unified isotopic "fingerprint library" for key organic families across environments, enabling the isotopic compositions of Solar System materials to be interpreted as outcomes of specific astrochemical histories. Through these developments, isotopic signatures will become not only passive tracers but quantitative diagnostics of organic evolution from star- and planet-forming regions to the Solar System.

Appendix A

Construction of the ^{13}C Isotopomer-Resolved Chemical Network

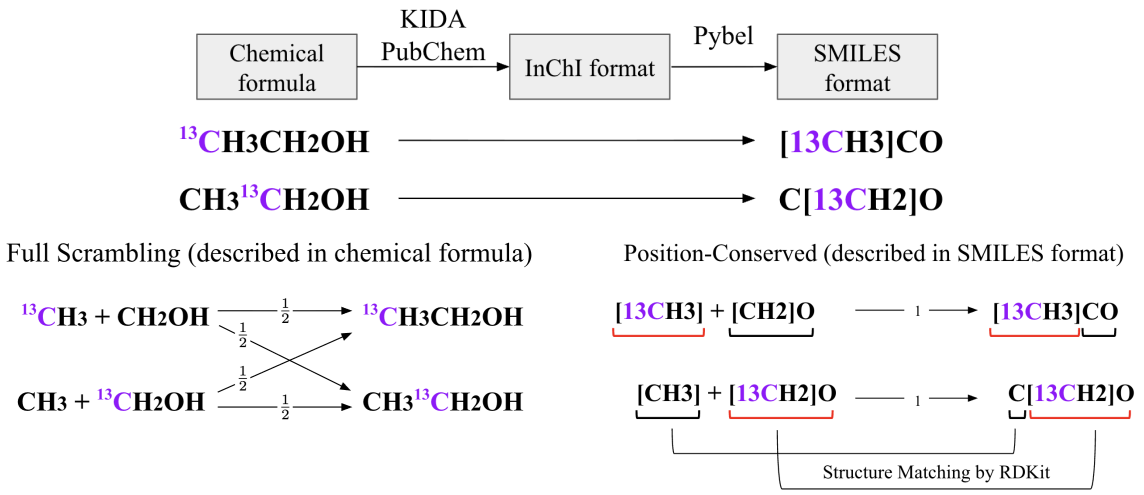

Figure A.1: Conversion of chemical formula to SMILES format representation (upper). Comparison between the full scrambling (lower left) and position-conserved (lower right) models taking the reaction for the formation of ethanol (C_2H_5OH), CH_3 + CH_2OH → C_2H_5OH as an example.

In this Appendix, we describe the computational methodology used to construct the ^{13}C isotopologue and isotopomer-resolved chemical network employed in this study. The goal of this procedure is to automatically generate position-specific ^{13}C-bearing species and to implement carbon-atom position–conserved reactions in

a chemically and structurally consistent manner. To accomplish this, we combine astrochemical reaction networks with cheminformatics tools, enabling explicit tracking of carbon atom positions through molecular transformations. The following section summarizes the workflow and key algorithms used in building the network.

We developed a PYTHON script that automatically incorporates ^{13}C isotopologues and ^{13}C position-conserved reactions into a chemical reaction network composed of molecular formulae. Conventional molecular formulae are insufficient for mechanically constructing such a chemical reaction network with carbon atom position-conserved reactions, because they do not specify which carbon atom, belonging to which functional group, is substituted with ^{13}C. Instead, we utilize the International Chemical Identifier (InChI; Heller et al. 2015) and the Simplified Molecular Input Line Entry System (SMILES; Weininger 1988) as molecular string grammars (see Figure A.1). InChI and SMILES represent the structure of molecules in formats interpretable by both humans and computers, provide a unique representation for each molecular structure, and can uniquely distinguish between structural isomers that cannot be differentiated by conventional molecular formulae (O'Boyle 2012; Fried et al. 2023; Scolati et al. 2023). Firstly, we acquire the InChI format of species in Garrod (2013) network from the KIDA (`https://kida.astrochem-tools.org/`) and PUBCHEM (`https://pubchem.ncbi.nlm.nih.gov/`) databases. InChI strings are converted to SMILES format via PYBEL (O'Boyle et al. 2008), which provides PYTHON access to the OPENBABEL library (`https://openbabel.org/index.html`). SMILES is a machine-readable notation for molecules, widely used in cheminformatics, a field that applies computational tools to chemical data analysis. We use the open-source toolkit 'RDKit' (`https://www.rdkit.org/`) to do cheminformatics analysis. The Substructure matching module in RDKit is used to identify common functional groups in reactant and product molecules and track the position of ^{13}C from reactants to products (see the right of Figure A.1). The CanonicalRankAtoms module is used to identify indistinguishable carbon atoms within a symmetric molecule. This module assigns a number 'rank' to each atom within the species. Atoms with the same rank are assigned to identical atoms in the species. If there are two or more ^{12}C atoms with the same rank in the species, the species in which one of them is replaced by ^{13}C are considered to be the same species. For example, the dimethyl ether (CH_3OCH_3) has two indistinguishable carbon atoms, meaning that its isotopologues $^{13}CH_3OCH_3$ and $CH_3O^{13}CH_3$ are equivalent. Therefore, in the radical-radical reaction, $CH_3 + CH_3O \rightarrow CH_3OCH_3$, even if a ^{13}C atom is present in either reactant, the products of '$^{13}CH_3 + CH_3O$' and '$CH_3 + {}^{13}CH_3O$' are identical.

References

Adande, G. R., & Ziurys, L. M. 2012, ApJ, 744, 194

Agúndez, M., Cernicharo, J., & Guélin, M. 2015, A&A, 577, L5

Aikawa, Y., Furuya, K., Yamamoto, S., & Sakai, N. 2020, ApJ, 897, 110

Aikawa, Y., Herbst, E., Roberts, H., & Caselli, P. 2005, ApJ, 620, 330

Aikawa, Y., Ohashi, N., Inutsuka, S.-i., Herbst, E., & Takakuwa, S. 2001, ApJ, 552, 639

Aikawa, Y., Wakelam, V., Garrod, R. T., & Herbst, E. 2008, ApJ, 674, 984

Andrews, S. M. 2020, ARA&A, 58, 483

Andrews, S. M., Wilner, D. J., Hughes, A. M., Qi, C., & Dullemond, C. P. 2009, ApJ, 700, 1502

Aponte, J. C., Elsila, J. E., Glavin, D. P., et al. 2017, ACS Earth and Space Chemistry, 1, 3

Armitage, P. J. 2011, ARA&A, 49, 195

Bacmann, A., Taquet, V., Faure, A., Kahane, C., & Ceccarelli, C. 2012, A&A, 541, L12

Bergin, E., Alexander, C., Drozdovskaya, M., Gounelle, M., & Pfalzner, S. 2024, in Comets III, ed. K. J. Meech, M. R. Combi, D. Bockelée-Morvan, S. N. Raymodn, & M. E. Zolensky, 3–32

Bergin, E. A., & Tafalla, M. 2007, ARA&A, 45, 339

Bohr, N. 1913, The London, Edinburgh, and Dublin Philosophical Magazine and Journal of Science, 26, 1

Bottinelli, S., Ceccarelli, C., Lefloch, B., et al. 2004, ApJ, 615, 354

Brunken, N. G. C., van Dishoeck, E. F., Slavicinska, K., et al. 2024, A&A, 692, A163

Burke, D. J., & Brown, W. A. 2010, Physical Chemistry Chemical Physics, 12, 5947

Burke, D. J., & Brown, W. A. 2010, Physical Chemistry Chemical Physics (Incorporating Faraday Transactions), 12, 5947

Busch, L. A., Pineda, J. E., Sipilä, O., et al. 2025, A&A, 699, A359

Cabedo, V., Maury, A., Girart, J. M., et al. 2023, A&A, 669, A90

Callear, A. B., & Cooper, I. A. 1990, Journal of the Chemical Society, Faraday Transactions, 86, 1763

Caselli, P., & Ceccarelli, C. 2012, A&A Rev., 20, 56

Chimiak, L., & Eiler, J. 2024, Chemical Geology, 644, 121828

Chimiak, L., Elsila, J. E., Dallas, B., et al. 2021, Geochim. Cosmochim. Acta, 292, 188

Colzi, L., Sipilä, O., Roueff, E., Caselli, P., & Fontani, F. 2020, A&A, 640, A51

Cooper, A. M., & Kästner, J. 2019, Journal of Physical Chemistry A, 123, 9061

Crimier, N., Ceccarelli, C., Maret, S., et al. 2010, A&A, 519, A65

Cummings, A. C., Stone, E. C., Heikkila, B. C., et al. 2016, ApJ, 831, 18

Cuppen, H. M., Walsh, C., Lamberts, T., et al. 2017, Space Sci. Rev., 212, 1

Daniel, F., Gérin, M., Roueff, E., et al. 2013, A&A, 560, A3

Draine, B. T. 2003, ARA&A, 41, 241

Elsila, J. E., Charnley, S. B., Burton, A. S., Glavin, D. P., & Dworkin, J. P. 2012, , 47, 1517

Endres, C. P., Schlemmer, S., Schilke, P., Stutzki, J., & Müller, H. S. P. 2016, Journal of Molecular Spectroscopy, 327, 95

Enrique-Romero, J., & Lamberts, T. 2025, arXiv e-prints, arXiv:2506.08792

Enrique-Romero, J., Rimola, A., Ceccarelli, C., et al. 2019, ACS Earth and Space Chemistry, 3, 2158

—. 2022, The Astrophysical Journal Supplement Series, 259, 39

Enrique-Romero, J., Rimola, A., Ceccarelli, C., et al. 2022, ApJs, 259, 39

Fedoseev, G., Qasim, D., Chuang, K.-J., et al. 2022, ApJ, 924, 110

Ferrero, S., Ceccarelli, C., Ugliengo, P., Sodupe, M., & Rimola, A. 2023, ApJ, 951, 150

Fraser, H. J., Collings, M. P., McCoustra, M. R. S., & Williams, D. A. 2001, MNRAS, 327, 1165

Fried, Z. T., Lee, K. L. K., Byrne, A. N., & McGuire, B. A. 2023, Digital Discovery, 2, 952

Furuya, K., & Aikawa, Y. 2018, ApJ, 857, 105

Furuya, K., Aikawa, Y., Hincelin, U., et al. 2015, A&A, 584, A124

Furuya, K., Aikawa, Y., Sakai, N., & Yamamoto, S. 2011, ApJ, 731, 38

Furuya, K., van Dishoeck, E. F., & Aikawa, Y. 2016, A&A, 586, A127

Garrod, R. T. 2013, ApJ, 765, 60

Garrod, R. T. 2013, ApJ, 765, 60

Garrod, R. T., & Herbst, E. 2006, A&A, 457, 927

Garrod, R. T., Widicus Weaver, S. L., & Herbst, E. 2008, ApJ, 682, 283

Gerlich, D., & Horning, S. 1992, Chemical Reviews, 92, 1509

Guilloteau, S., Dutrey, A., Piétu, V., & Boehler, Y. 2011, A&A, 529, A105

Hama, T., Kuwahata, K., Watanabe, N., et al. 2012, ApJ, 757, 185

Hama, T., & Watanabe, N. 2013, Chemical Reviews, 113, 8783

Hasegawa, T. I., & Herbst, E. 1993, MNRAS, 263, 589

Hasegawa, T. I., Herbst, E., & Leung, C. M. 1992, ApJS, 82, 167

Heller, S. R., McNaught, A., Pletnev, I., Stein, S., & Tchekhovskoi, D. 2015, Journal of cheminformatics, 7, 23

Herbst, E., & Klemperer, W. 1973, ApJ, 185, 505

Herbst, E., & van Dishoeck, E. F. 2009, ARAA, 47, 427

Hirota, T., Ohishi, M., & Yamamoto, S. 2009, ApJ, 699, 585

Hollenbach, D., & McKee, C. F. 1979, ApJS, 41, 555

Hollenbach, D., & Salpeter, E. E. 1970, J. Chem. Phys., 53, 79

Hollenbach, D. J., & Tielens, A. G. G. M. 1999, Reviews of Modern Physics, 71, 173

Ibrahim, M., Guillemin, J.-C., Chaquin, P., Markovits, A., & Krim, L. 2024, Physical Chemistry Chemical Physics, 26, 4200

Indriolo, N., & McCall, B. J. 2012, ApJ, 745, 91

Jenkins, E. B. 2009, ApJ, 700, 1299

Jiménez-Serra, I., Vasyunin, A. I., Caselli, P., et al. 2016, ApJ, 830, L6

Jin, M., & Garrod, R. T. 2020, The Astrophysical Journal Supplement Series, 249, 26

Jin, M., & Garrod, R. T. 2020, ApJS, 249, 26

Johnson, R. E. 1990, Energetic Charged-Particle Interactions with Atmospheres and Surfaces, doi:10.1007/978-3-642-48375-2

Jørgensen, J. K., Belloche, A., & Garrod, R. T. 2020, ARA&A, 58, 727

Jørgensen, J. K., van der Wiel, M. H. D., Coutens, A., et al. 2016, A&A, 595, A117

Jørgensen, J. K., Müller, H. S. P., Calcutt, H., et al. 2018, A&A, 620, A170

Knyazev, V. D. 2017, Chemical Physics Letters, 685, 165

Langer, W. D., Graedel, T. E., Frerking, M. A., & Armentrout, P. B. 1984a, ApJ, 277, 581

—. 1984b, ApJ, 277, 581

Langevin, P. 1905, A fundamental formula of kinetic theory

Langmuir, I. 1918, Journal of the American Chemical society, 40, 1361

Larson, R. B. 1969, Monthly Notices of the Royal Astronomical Society, 145, 271

Linsky, J. L. 2003, Space Sci. Rev., 106, 49

Loison, J.-C., Wakelam, V., Gratier, P., & Hickson, K. M. 2020, MNRAS, 498, 4663

Lombardi, M., Bouy, H., Alves, J., & Lada, C. J. 2014, A&A, 566, A45

Magalhães, V. S., Hily-Blant, P., Faure, A., Hernandez-Vera, M., & Lique, F. 2018, A&A, 615, A52

Masunaga, H., & Inutsuka, S.-i. 2000, ApJ, 531, 350

McElroy, D., Walsh, C., Markwick, A. J., et al. 2013, A&A, 550, A36

McElroy, D., Walsh, C., Markwick, A. J., et al. 2013, Astronomy and Astrophysics, 550, A36

McGuire, B. A. 2022, ApJS, 259, 30

McKee, C. F., & Ostriker, E. C. 2007, ARA&A, 45, 565

Meisner, J., & Kästner, J. 2016, Angewandte Chemie International Edition, 55, 5400

Milam, S. N., Savage, C., Brewster, M. A., Ziurys, L. M., & Wyckoff, S. 2005a, ApJ, 634, 1126

—. 2005b, ApJ, 634, 1126

Minissale, M., Dulieu, F., Cazaux, S., & Hocuk, S. 2016, A&A, 585, A24

Miyazaki, A., Tsuge, M., Hidaka, H., Nakai, Y., & Watanabe, N. 2022, ApJl, 940, L2

Molpeceres, G., K00E4stner, J., Fedoseev, G., et al. 2021, The Journal of Physical Chemistry Letters, 12, 10854, pMID: 34727500

Müller, H. S. P., Schlöder, F., Stutzki, J., & Winnewisser, G. 2005, Journal of Molecular Structure, 742, 215

Nomura, H., & Millar, T. J. 2004, A&A, 414, 409

Nomura, H., Furuya, K., Cordiner, M. A., et al. 2023, in Astronomical Society of the Pacific Conference Series, Vol. 534, Astronomical Society of the Pacific Conference Series, ed. S. Inutsuka, Y. Aikawa, T. Muto, K. Tomida, & M. Tamura, 1075

O'Boyle, N. 2012, Journal of cheminformatics, 4, 22

O'Boyle, N. M., Morley, C., & Hutchison, G. R. 2008, Chemistry Central Journal, 2, 1

Oya, Y., López-Sepulcre, A., Sakai, N., et al. 2019, ApJ, 881, 112

Padovani, M., Galli, D., & Glassgold, A. E. 2009, A&A, 501, 619

Padovani, M., Hennebelle, P., Marcowith, A., & Ferrière, K. 2015, A&A, 582, L13

Padovani, M., Ivlev, A. V., Galli, D., & Caselli, P. 2018, A&A, 614, A111

Padovani, M., Marcowith, A., Hennebelle, P., & Ferrière, K. 2016, A&A, 590, A8

Penston, M. V. 1969, Monthly Notices of the Royal Astronomical Society, 144, 425

Pineda, J. E., Maury, A. J., Fuller, G. A., et al. 2012, A&A, 544, L7

Potapov, A., Krasnokutski, S. A., Jäger, C., & Henning, T. 2021, ApJ, 920, 111

Prasad, S. S., & Huntress, W. T. 1980, The Astrophysical Journal Supplement Series, 43, 1

Prasad, S. S., & Tarafdar, S. P. 1983, ApJ, 267, 603

Rideal, E. 1939in , Cambridge University Press, 130–132

Roueff, E., Loison, J. C., & Hickson, K. M. 2015, A&A, 576, A99

Ruaud, M., Loison, J., Hickson, K., et al. 2015, Monthly Notices of the Royal Astronomical Society, 447, 4004

Ruaud, M., Loison, J. C., Hickson, K. M., et al. 2015, MNRAS, 447, 4004

Ruaud, M., Wakelam, V., & Hersant, F. 2016, MNRAS, 459, 3756

Ruffle, D. P., & Herbst, E. 2000, MNRAS, 319, 837

Sadavoy, S. I., Myers, P. C., Stephens, I. W., et al. 2018, ApJ, 869, 115

Sakai, N., Saruwatari, O., Sakai, T., Takano, S., & Yamamoto, S. 2010, A&A, 512, A31

Sakai, N., Takano, S., Sakai, T., et al. 2013, Journal of Physical Chemistry A, 117, 9831

Sakai, N., & Yamamoto, S. 2013, Chemical Reviews, 113, 8981

Scolati, H. N., Remijan, A. J., Herbst, E., McGuire, B. A., & Lee, K. L. K. 2023, ApJ, 959, 108

Shingledecker, C. N., Tennis, J., Le Gal, R., & Herbst, E. 2018, ApJ, 861, 20

Shu, F. H. 1977, The Astrophysical Journal, 214, 488

Sipilä, O., Colzi, L., Roueff, E., et al. 2023, A&A, 678, A120

Smith, L. R., Gudipati, M. S., Smith, R. L., & Lewis, R. D. 2021, A&A, 656, A82

Smith, R. L., Pontoppidan, K. M., Young, E. D., & Morris, M. R. 2015, ApJ, 813, 120

Spinks, J. W., & Woods, R. J. 1990, An introduction to radiation chemistry (New York, NY (USA); John Wiley and Sons Inc.)

Spitzer, Jr., L., & Tomasko, M. G. 1968, ApJ, 152, 971

Su, T., & Chesnavich, W. J. 1982, The Journal of Chemical Physics, 76, 5183

Takano, S., Masuda, A., Hirahara, Y., et al. 1998, A&A, 329, 1156

Taquet, V., Charnley, S. B., & Sipilä, O. 2014, ApJ, 791, 1

Terzieva, R., & Herbst, E. 1998, ApJ, 501, 207

Tielens, A. G. G. M. 2013, Reviews of Modern Physics, 85, 1021

Tielens, A. G. G. M. 2021, Molecular Astrophysics (Cambridge University Press)

Tielens, A. G. G. M., & Hagen, W. 1982, A&A, 114, 245

Tsuge, M., Molpeceres, G., Aikawa, Y., & Watanabe, N. 2023, Nature Astronomy, 7, 1351

Tsuge, M., Molpeceres, G., Aikawa, Y., & Watanabe, N. 2024, ApJ, 973, 80

van Dishoeck, E. F., & Black, J. H. 1988a, ApJ, 334, 771

—. 1988b, ApJ, 334, 771

van Dishoeck, E. F., & Blake, G. A. 1998, ARA&A, 36, 317

Vasyunin, A. I., & Herbst, E. 2013, ApJ, 762, 86

Visser, R., van Dishoeck, E. F., & Black, J. H. 2009, A&A, 503, 323

Wakelam, V., Loison, J.-C., Mereau, R., & Ruaud, M. 2017, Molecular Astrophysics, 6, 22

Wakelam, V., Vastel, C., Aikawa, Y., et al. 2014, MNRAS, 445, 2854

Wakelam, V., Herbst, E., Loison, J.-C., et al. 2012, The Astrophysical Journal Supplement Series, 199, 21

Ward-Thompson, D., Motte, F., & Andre, P. 1999, MNRAS, 305, 143

Watson, W. D., Anicich, V. G., & Huntress, W. T., J. 1976, ApJ, 205, L165

Weininger, D. 1988, Journal of chemical information and computer sciences, 28, 31

Wilson, T. L., & Rood, R. 1994, ARA&A, 32, 191

Woodall, J., Agúndez, M., Markwick-Kemper, A. J., & Millar, T. J. 2007, Astronomy and Astrophysics, 466, 1197

Yamato, Y., Notsu, S., Aikawa, Y., et al. 2024, AJ, 167, 66